Title

Dendrite Suppression Strategies in Li-Metal Solid-State Batteries: Mechanisms and Innovations

Author

Diallo, Mouhamad Said Al Hamid

Publication Date

2024

Peer reviewed|Thesis/dissertation

Dendrite Suppression Strategies in Li-Metal Solid-State Batteries: Mechanisms and Innovations

By

Mouhamad Saïd Al Hamid Diallo

A dissertation submitted in partial satisfaction of the

requirements for the degree of

Doctor of Philosophy

in

Engineering Materials - Science and Engineering

in the

Graduate Division

of the

University of California, Berkeley

Committee in charge:

Professor Gerbrand Ceder, Chair

Professor Mary Cooper Scott

Professor Bryan McCloskey

Fall 2024

Dendrite Suppression Strategies in Li-Metal Solid-State Batteries: Mechanisms and Innovations

Abstract

Dendrite Suppression Strategies in Li- Metal Solid-State Batteries: Mechanisms and Innovations

by

Mouhamad Saïd Al Hamid Diallo

Doctor of Philosophy in Engineering – Materials Science and Engineering

University of California, Berkeley

Professor Gerbrand Ceder, Chair

The development of lithium metal solid-state batteries offers significant potential for next-generation energy storage systems, particularly in terms of energy density and operational safety. However, their commercialization is hindered by challenges such as lithium dendrite formation, which can lead to short circuits and battery failure. This dissertation aims to provide a comprehensive understanding of dendrite growth mechanisms in solid electrolytes and explores various strategies to suppress dendrite propagation. Our research investigates the role of solid-electrolyte pellet density in the performance and failure of solid-state batteries. We find that a 99.5% dense solid electrolyte transitions from a pore-percolating to a non-percolating structure, significantly improving the longevity of the battery by preventing short-circuiting under high current densities. Additionally, we explore the role of the Ag/C buffer layers in anode-free solid-state batteries, using first-principles atomistic and continuum modeling techniques. Our findings reveal that the Ag/C BL promotes uniform lithium deposition and reduces interfacial resistance, which enhances cycling stability and mitigates dendrite formation.

Furthermore, we demonstrate that silver nanoparticles play a key role in suppressing dendrite growth and preventing stress-induced solid electrolyte fractures in lithium metal solid-state batteries. Through ex-situ characterization techniques such as Focused-ion beam – scanning electron microscopy and energy dispersive X-ray spectroscopy , we show that Ag nanoparticles migrate alongside Li dendrites, promoting homogeneous growth and reducing localized stress concentrations. This uniform distribution of lithium could potentially enable higher charging rates, further enhancing the performance and safety of lithium metal solid-state batteries. By combining experimental and computational approaches, this work contributes to the broader understanding of dendrite suppression in lithium metal solid-state batteries, providing insights into the optimization of solid electrolyte properties, buffer layer design, and nanoparticle incorporation. The results presented in this dissertation offer promising pathways toward the commercialization of safer, high-performance solid-state batteries.

To God,

هُوَ ٱللَّهُ ٱلَّذِى لَآ إِلَٰهَ إِلَّا هُوَ ۖ عَٰلِمُ ٱلْغَيْبِ وَٱلشَّهَٰدَةِ ۖ هُوَ ٱلرَّحْمَٰنُ ٱلرَّحِيمُ ٢٢ هُوَ ٱللَّهُ ٱلَّذِى لَآ إِلَٰهَ إِلَّا هُوَ ٱلْمَلِكُ ٱلْقُدُّوسُ ٱلسَّلَٰمُ ٱلْمُؤْمِنُ ٱلْمُهَيْمِنُ ٱلْعَزِيزُ ٱلْجَبَّارُ ٱلْمُتَكَبِّرُ ۚ سُبْحَٰنَ ٱللَّهِ عَمَّا يُشْرِكُونَ ٢٣ هُوَ ٱللَّهُ ٱلْخَٰلِقُ ٱلْبَارِئُ ٱلْمُصَوِّرُ ۖ لَهُ ٱلْأَسْمَآءُ ٱلْحُسْنَىٰ ۚ يُسَبِّحُ لَهُۥ مَا فِى ٱلسَّمَٰوَٰتِ وَٱلْأَرْضِ ۖ وَهُوَ ٱلْعَزِيزُ ٱلْحَكِيمُ ٢٤

He is Allāh, other than whom there is no deity, Knower of the unseen and the witnessed. He is the Entirely Merciful, the Especially Merciful.(22) He is Allāh, other than whom there is no deity, the Sovereign, the Pure, the Perfection, the Grantor of Security, the Overseer, the Exalted in Might, the Compeller, the Superior. Exalted is Allāh above whatever they associate with Him.(23) He is Allāh, the Creator, the Producer, the Fashioner; to Him belong the best names. Whatever is in the heavens and earth is exalting Him. And He is the Exalted in Might, the Wise.(24)

Qur'an 59:22 – 24

وَيَزِيدُ ٱللَّهُ ٱلَّذِينَ ٱهْتَدَوْا۟ هُدًى ۗ وَٱلْبَٰقِيَٰتُ ٱلصَّٰلِحَٰتُ خَيْرٌ عِندَ رَبِّكَ ثَوَابًا وَخَيْرٌ مَّرَدًّا

And Allāh increases those who were guided, in guidance, and the enduring good deeds are better to your Lord[1] for reward and better for recourse.

Qur'an 19:76

My Family, and Friends,

For their unconditional support and love

Table of Contents

List of Figures and Tables

Chapter 1: Introduction

Chapter 2: Effects of Solid-Electrolyte Pellet Density on Failure of Solid-State Batteries

Figures:

Tables:

Supplementary – Information: Chapter 2: Effects of Solid-Electrolyte Pellet Density on Failure of Solid-State Batteries

Chapter 3: The Microscopic Mechanism of Lithiation and Delithiation in the Ag/C Buffer Layer for Anode-free Solid-state Batteries

Figures:

Tables:

Supplementary Information – Chapter 3: The Microscopic Mechanism of Lithiation and Delithiation in the Ag/C Buffer Layer for Anode-free Solid-state Batteries

Figures:

Tables:

Chapter 4: Mitigating battery cell failure: Role of Ag-nanoparticle fillers in solid electrolyte dendrite suppression

Figures:

Tables:

Supplementary Information – Chapter 4: Mitigating battery cell failure: Role of Ag-nanoparticle fillers in solid electrolyte dendrite suppression

Acknowledgements

We begin our affairs in the name of God (بِسْمِ اللَّهِ الرَّحْمَٰنِ الرَّحِيمِ), and we close our matters by expressing our gratitude. I thank God (ٱلْحَمْدُ لِلَّهِ), for giving me the ability to overcome most of the challenges and giving me the strength to keep striving despite the many obstacles. While we acknowledge those who stayed with us throughout this journey, we also pray for the souls of those who have departed from this plane of existence. May the souls of the deceased rest in peace.

First and foremost, I would like to acknowledge my whole family for their unconditional support and love: my mother, Dr. Aïcha Fall, who has always been a role model in all aspects of life, and my father, Dr. Ousmane Diallo, along with my siblings—Tahir, Zaynab, Cheikh, and Salimatou—and their families and children. My heartfelt thanks to my delightful wife, Rama, whose support and care have been a constant source of strength. She has truly been the highlight of my Ph.D. journey at UC Berkeley.

I extend my sincere thanks to my advisor, Prof. Gerbrand Ceder, for giving me the opportunity to be part of the Ceder group. Over the past five years, I have been fortunate to learn invaluable lessons from him that have significantly shaped my research journey. I also wish to thank my qualifying exam and dissertation committee members, Prof. Mark Asta, Prof. Mary Cooper Scott, Prof. Bryan McClosky, and Prof. Andrew Minor, for their invaluable support and critical insights, which have been instrumental in shaping my thesis. Additionally, I express my gratitude to all the sponsors of the Ceder group, whose continued support has allowed us to pursue exciting research.

I am grateful to all my collaborators—Prof. Gerbrand Ceder, Prof. Mary Cooper Scott, Prof. Qingsong Howard Tu, Prof. Christopher Bartel, Prof. Yan Zeng, Prof. Solomon Oyakhire, Dr. Tan Shi, Dr. Yaqian Zhang, Dr. Xinxing Peng, Dr. Yan Wang, Dr. Lincoln Miara, Dr. Fengyu Xie, Dr. Haegyeom Kim, Dr. Nathan Szymanski, Dr. Venkata Avvaru, Dr. Xiaochen Yang, Dr. Tofunmi Ogunfunmi, and Dr. Imtiaz Shozib—whose support was instrumental in completing my thesis.

It was truly my honor to share my work environment with many talented individuals in the Ceder group. I would like to express my gratitude starting with my fellow "first-years," who are all very dear friends: Yunyeong Choi, Nathan Szymanski, and Kevin Cruse, with whom I started and finished this journey. We have been through a lot together, and I am happy that we all stuck to the plan and are able to graduate. Special thanks to Tan Shi and Howard Tu for mentoring me in my early Ph.D. days when I was adjusting to the solid-state field. Your patience and support were vital during that challenging time.

Among the many problems we faced in the lab, the most appreciated thing was always finding reliable friends who could support us and were ready to help in any way they could. I would like

to thank all the wonderful people who added so much quality to my Ph.D. experience: Yan Zeng for our wonderful discussions and tea times, which I always remember fondly; Kyujung Jun for all the pleasant discussions and wonderful cat stories; Zijian Cai, Yingzhi Sun, and Han-Ming Hau for the good food and the pain we shared while performing maintenance on lab equipment; Yu Chen for being so wonderful and always ready to help with anything; Xiaochen Yang for being an amazing friend and great colleague—we shared so many discussions about science and life; Yuxing Fei and Bernardus Rendy for showing me what real-life robots look like; and finally, Shillong Wang for all the help and the great personality. Sharing the workspace and social events with Ronald Kam, Grace Wei, Tucker Holstun, Benjamin Lam, and Eunryeol Lee was a delight. I would also like to thank everyone in the Ceder group, including Julia, Luis, Huiwen, Zhengyan, Jingyang, Jiangping, Zinab, Dogancan, Zheren, Tina, Yaosen, Amalie, Olga, Yaqian, Peichen, Fengyu, Yihan, Tanjin, Bin, Haoyan, Xu, Jia-wei, Bowen, Xinye, Lauren, Tara, Zhuohan, Shash, and Sunny, for the moments we shared.

I cannot forget to thank the behind-the-scenes heroes: Sonia Dominguez, Alice Muller, Emma Rose, Muzghan Ali, Shannon Dowling, Ariana, and Catalina for their incredible support. We were fortunate to be in their care. Additionally, my thanks to Kristopher Pearson and John Lindsay in the machine shop, Paul Johnson, Elda, and the lab team.

I also thank my undergraduate physics professor, Dr. Nancy Ann Woods, whose support and impact have been monumental. Her kindness and dedication to helping students have always represented, to me, the best of what America stands for. I extend my thanks to all the staff, professors, and friends I made at DMACC, especially Kate Bergin and Marco, and at Iowa State University, who have helped me along the way. Special thanks to my undergraduate mentors: Dr. Ganesh Balasubramanian, Dr. Pratik Ray, Dr. Aayush Sharma, Dr. Srilok Srinivasan, Dr. Raul Sing and Dr. Boyce Cheng. I am also grateful to the LSAMP and McNair programs, which helped me pursue a research career early on.

Lastly, but certainly not least, I am deeply grateful for the friendship of my amazing cohort, particularly Yunyeong, Abdullah Saud Abbas, Viktoriia Baibakova, and Daewon Lee, with whom I shared many cherished moments. I extend my deepest respect to those suffering across the world, whose resilience is a constant reminder of our shared humanity, especially to our friends and allies in Palestine, for whom we pray for liberation and the right to self-determination, alongside all their neighbors, in prosperity and security. I also extend my thanks to my friends in the Bay Area, including Karim Ndiaye, Ngone Ndiaye, and their entire family for warmly welcoming me, as well as Abdoulaye Cisse, Khadija Diop, Niokhor Dione, Emma Smith, Chams Mballo, Doudou Mbaye, Astou Ndoye, Imam Issa, Mor Seye and all our friends in the Senegalese community for their unforgettable companionship. I also extend my gratitude to the Rouse family for allowing me to share this journey with them. Finally, I would like to thank everyone I have interacted with over the past few years whose names I could not include in this acknowledgment, but whose presence and support have left a lasting impact on my life.

Chapter 1: Introduction

1.1 Motivation

The global landscape of energy access and consumption is at a critical juncture. Despite significant advancements, a substantial portion of the world's population still lacks access to electricity. Africa, home to approximately 1.5 billion people—about 20% of the global population—has the largest share of individuals without electricity, as illustrated in *Figure 1.1*. Currently, the majority of the world's electricity is generated from fossil fuels, including coal, oil, and natural gas. While these energy sources have driven industrialization and scientific progress, they are also the primary contributors to greenhouse gas emissions, which are fueling the ongoing climate crisis. As the global population continues to grow, with a current birth rate of 17.668 births per 1,000 people,[1,2] and as efforts to expand electrification intensify, the demand for energy is expected to increase significantly. If billions of people were to gain access to electricity using conventional energy sources, the environmental consequences could be catastrophic, further accelerating climate change and its associated impacts.

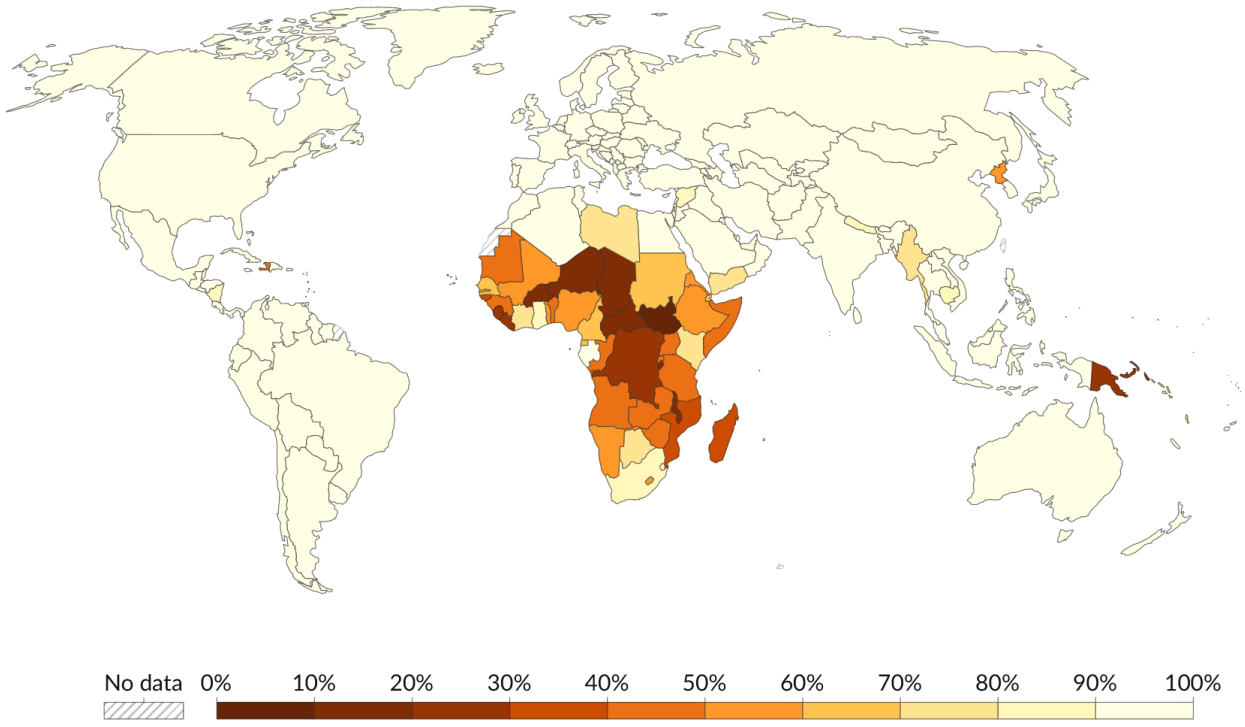

Figure1. 1. Share of the population with access to electricity in 2021.

The climate crisis, driven largely by the combustion of fossil fuels, poses an existential threat to ecosystems, economies, and societies worldwide. The transition to cleaner, more sustainable energy sources is no longer a matter of debate but an imperative. Renewable energy sources such

as solar, wind, and hydroelectric power have made remarkable progress in recent years.[3,4] However, they also present their own set of challenges, particularly in energy storage.

In this context, batteries play a crucial role in enabling the widespread adoption of renewable energy. The intermittency of energy sources like solar and wind necessitates efficient and reliable energy storage solutions to ensure a steady power supply. Lithium-ion batteries (LIBs) have become pervasive in modern electronics, powering everything from consumer electronics to electric vehicles (EVs). Their widespread use is driven by their relatively high energy density, long cycle life, and decreasing costs. Over the last few decades, LIB energy density has significantly improved—from around 90 Wh kg^{-1} to over 250 Wh kg^{-1}—making them key components in the push to decarbonize global energy systems.[5]

The rise of the electric vehicle market has played a crucial role in driving demand for LIBs. In 2023, the global EV fleet exceeded 40 million vehicles, up by 3.5 million from the previous year, which is a 35% increase.[6] However, despite the growth in EV adoption, significant challenges remain. Further improvements in battery technology are essential to achieve the performance and safety standards necessary for widespread adoption of EVs. Higher energy density batteries would allow EVs to travel longer on a single charge, while higher power density batteries could reduce charging times. Safety remains a critical concern, as the flammability of the liquid electrolytes used in current LIBs is a significant risk factor, particularly in high-energy applications like EVs [7]. LIB technology, though revolutionary, is approaching its theoretical limits. While incremental improvements are still possible, especially with high-nickel cathodes and silicon-based anodes, the energy density targets set by organizations such as the U.S. Department of Energy (DOE) and the U.S. Advanced Battery Consortium (USABC) — 470 Wh/kg and 1000 Wh/L—are beyond the reach of conventional LIB designs [8–16]. As a result, the focus has shifted towards next-generation battery technologies, with solid-state batteries (SSBs) emerging as one of the most promising alternatives.

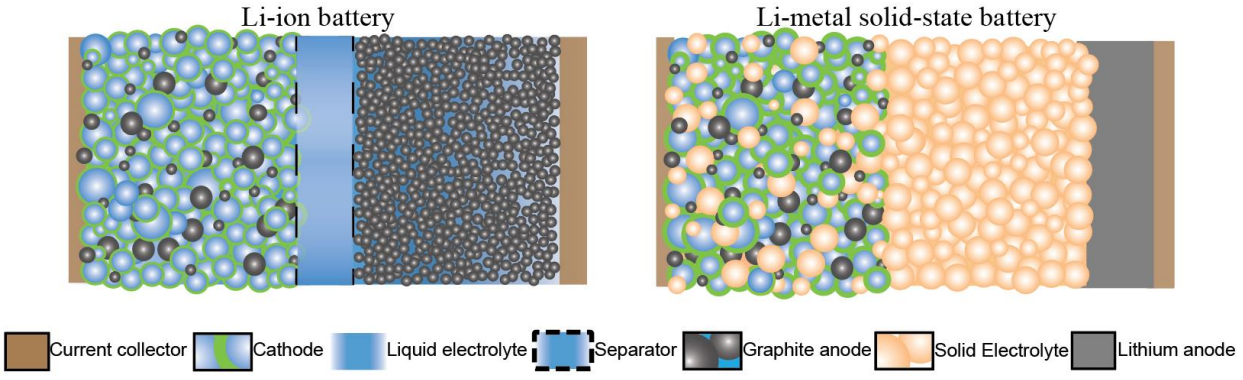

Figure1. 2. Schematic illustration of a typical Li-ion battery (left) and a Li-metal SSB (right).

In SSBs, the liquid electrolyte found in conventional LIBs, as illustrated in *Figure 1.2*, is replaced with a solid ionic conductor, namely a solid electrolyte (SE), which offers several advantages. The use of non-flammable SEs improves the safety of the battery[17], reducing the risk of fires or

explosions. Furthermore, SSBs enable the use of a lithium metal anode, which has a much higher theoretical capacity (3860 mAh/g) compared to the graphite anodes typically used in LIBs. [18–21] The pairing of a lithium metal anode with a SE could significantly increase the energy density of the battery, making SSBs a strong candidate for next-generation EV batteries and other high-performance applications[22]. Despite the promise of SSBs, several technical challenges remain. One of the key issues is the formation of lithium dendrites, which are metallic structures that can grow through the SE during charge and discharge cycles, causing short circuits and battery failure. Dendrite formation is a critical challenge in the development of SSBs, as it compromises both the safety and longevity of the battery. To fully realize the potential of SSBs, it is essential to develop effective strategies that allow the use of SEs with high ionic conductivity and excellent chemical stability against lithium metal.

Sulfide-based SEs have emerged as a promising candidate for use in SSBs. These materials offer high ionic conductivity and low interfacial resistance, making them suitable for scalable production through techniques like cold pressing[23]. Sulfide-based electrolytes, such as $Li_7P_3S_{11}$, have demonstrated excellent performance in glass-ceramic form, providing a balance between conductivity and processability. Crystalline sulfides like thio-LISICON and Li argyrodites have shown even higher ionic conductivities, surpassing those of conventional liquid electrolytes in some cases[24–27]. The high ionic conductivity and processability of sulfide-based electrolytes make them attractive for SSB applications, but their role in suppressing dendrite growth is still being explored. The high mechanical modulus of some SEs may help prevent dendrites from propagating, but more research is needed to fully understand the mechanisms at play. Additionally, the interfacial stability between the lithium metal anode and the sulfide electrolyte remains a key area of investigation. Developing a stable, low-resistance interface is critical to improving the cycling stability and performance of SSBs.

In summary, while lithium-ion batteries have played a pivotal role in the evolution of energy storage technologies, their limitations in terms of energy density, safety, and performance have prompted the search for next-generation solutions. SSBs, particularly those utilizing sulfide-based electrolytes, represent a promising path forward. This thesis will focus on the challenges associated with dendrite formation in sulfide-based SSBs and explore potential strategies for mitigating this issue, with the aim of advancing the development of safer and more efficient energy storage technologies for a renewable energy future.

1.2 Li dendrites in SSBs

Li-metal dendrites are needle-like structures that form in Li-metal SSBs during charging and discharging, specifically at the Li anode interface with the SE. These dendrites can grow through the SE towards the cathode, potentially short-circuiting the battery and leading to failures and safety concerns. While conventional Li-ion batteries face risks of fires and explosions due to dendrite-induced internal short circuits, SSBs reduce this risk thanks to the non-flammable nature of SEs. However, the existence of dendrites still compromises battery performance and longevity.

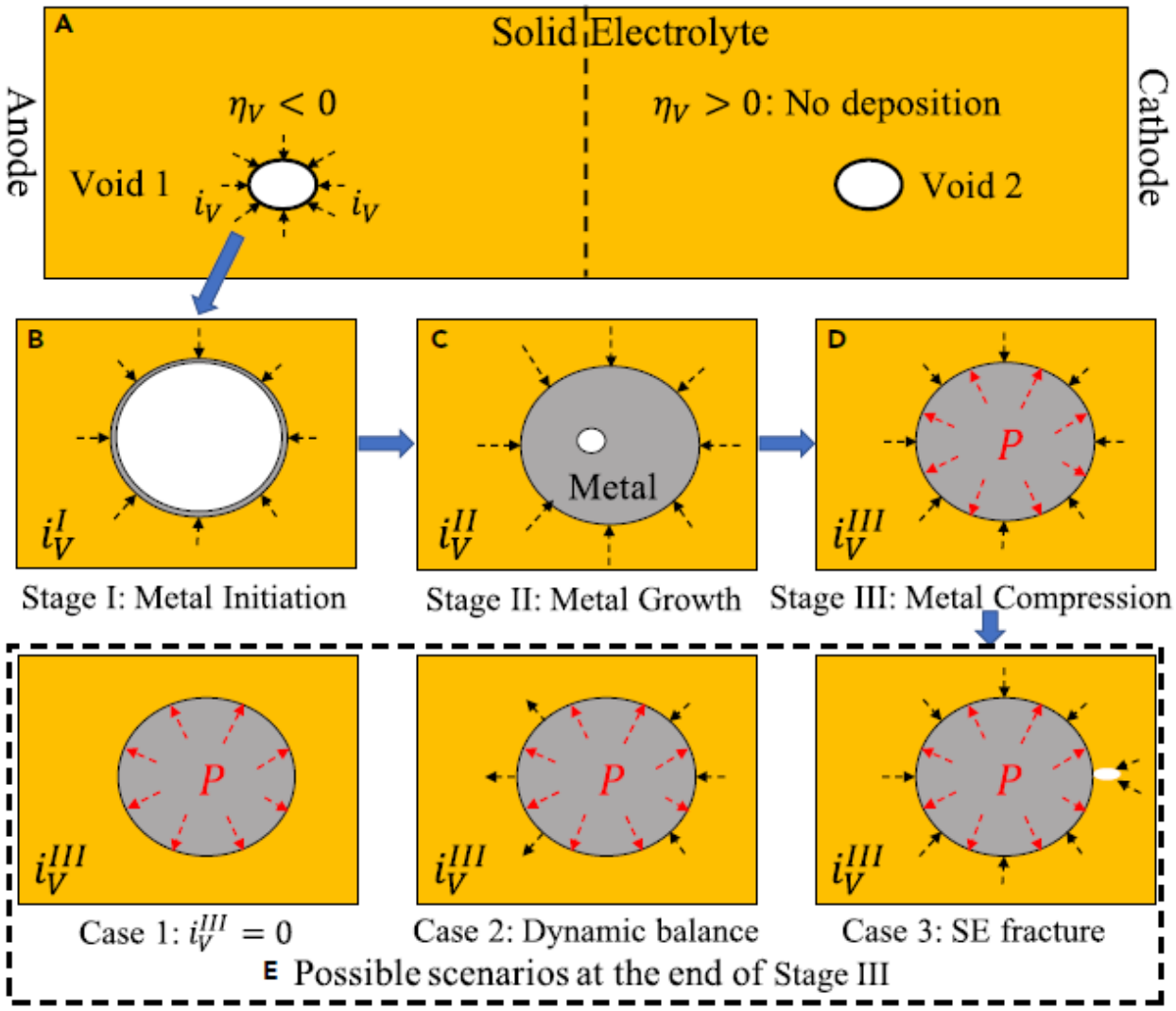

Figure1. 3. Illustration of different stages of metal deposition in a void in the SE. (reproduced from [28])

In their seminal work on the impact of elastic deformation on lithium deposition kinetics at the Li/polymer interface, Monroe and Newman propose that when the separator's shear modulus is approximately twice that of Li, the amplification of surface roughness—leading to dendrite formation—can be mechanically suppressed. This finding suggests that enhancing the mechanical properties of the SE, particularly its shear modulus, is crucial for preventing dendrite growth.[29,30]

Conversely, Barroso-Luque et al. developed a theoretical model to explain how electrodeposition-induced plastic flow and stress concentrations at defects within SEs contribute to metal propagation and eventual mechanical failure in SSBs. Their findings indicate that controlling the SE's microstructural properties, particularly by minimizing defects and enhancing material strength, is essential for mitigating metal propagation and preventing short circuits. This study provides critical insights into the role of stress and mechanical properties in designing more robust solid-state batteries.[31] Tu et al. further highlights that metal propagation can occur through defects

like grain boundaries and pores or be driven by electronic conductivity within the SE itself, leading to internal nucleation and growth of metal filaments. The study identifies three critical stages of metal deposition within solid electrolytes: metal plating initiation, metal growth, and metal compression. These stages describe the progression from initial metal deposition in internal voids to the compression of these deposits, potentially leading to fractures in the SE, irrespective of its mechanical properties.[28]

Additionally, Ji et al. investigate the mechanisms behind lithium dendrite formation in solid-state electrolytes (SSEs), showing that chemical reactions at the interface between lithium and SEs significantly influence dendrite formation. When SEs are not chemically stable with lithium, reactions can produce byproducts with high electronic conductivity, such as Li3P in certain sulfide-based SEs. These conductive byproducts lower the energy barrier for lithium nucleation and facilitate dendrite growth within the SE. High electronic conductivity within the SE or its decomposition products allows electrons to migrate more freely, enabling lithium to nucleate and grow inside the electrolyte rather than just at the surface. This combination of chemical instability and increased electronic conductivity transforms the dendrite growth mechanism from purely mechanical to electrochemical, accelerating dendrite penetration and potentially leading to short circuits and battery failure.[32]

The literature suggests that multiple mechanisms are at play in dendrite formation. While Monroe and Newman's conclusions emphasize the importance of mechanical properties, other studies demonstrate that SE microstructure, electronic conductivity, and chemical stability against lithium all significantly influence the propensity for dendrite growth. These findings prompted our investigations, presented in *Chapter 2*, which aim to illuminate the mechanisms of SSB failure through comprehensive experimental and computational studies.

1.3 State-of-the-art solutions

As the field of SSBs advances, several innovative solutions have been proposed to mitigate dendrite formation, which remains the most significant challenge to commercialization. One of the most groundbreaking developments is the introduction of active buffer layers. A buffer layer is an additional material placed between the Li anode and the SE to prevent dendrite-promoting phenomena that arise from the interfacial interactions between Li and the SE. By leveraging the unique properties of silver nanoparticles and carbon black, Lee et al. demonstrate that the Ag-C layer facilitates uniform lithium deposition, thereby mitigating the risk of dendrite-induced short circuits. The resulting improvements in energy density—exceeding 900 Wh/L—and cycling stability of up to 1,000 cycles, with high cathode loading of 6.8 mAh cm^{-2} and a stable Coulombic efficiency over 99.8%, highlight the Ag-C buffer layer's potential to significantly enhance the performance and safety profile of SSBs.[33] In a subsequent report, Suzuki et al. further explore the effectiveness of buffer layers, emphasizing the critical role of carbon microstructure. They found that carbon black (CB), an amorphous material, outperforms graphite in suppressing short circuits. While the CB layer effectively prevents short circuits, graphite fails

to do so. The authors also observed that lithium penetrates the CB layer and deposits between the current collector and the CB layer, a behavior not seen with graphite. Additionally, the study assessed the performance of five metals mixed with CB, with silver (Ag) demonstrating superior performance compared to zinc, tin, aluminum, and nickel.[34] In both published works, the explanation behind the Li plating between the current collector and the SE, along with the seemingly better performance when Ag was added to the buffer layer instead of the other metals was not provided.

Kim et al. provided a pioneering explanation for the lithium plating behavior in solid-state batteries, attributing it to the differences in interfacial energy between the buffer layer and the SE versus the buffer layer and the current collector. They found that the buffer layer-SE interface has a higher adhesion energy, making it less favorable for lithium deposition compared to the buffer layer-current collector interface. This energy difference drives lithium to deposit preferentially at the interface with lower energy, leading to more controlled and uniform plating. The study also highlights the crucial role of carbon in the buffer layer, as it governs the rate capabilities, which are limited by the diffusion of lithium through the carbon layer. The metal particles embedded in the carbon layer primarily serve to homogenize the current density, a key factor in suppressing dendrite formation. [35] Numerous studies have explored different aspects of buffer layers, providing valuable insights into their mechanisms of action. Spencer-Jolly et al. investigated the in-situ phase evolution of Li within a graphite-Ag buffer layer, revealing that lithium first intercalates into graphite, then reacts with silver to form various Li-Ag alloy phases, and eventually deposits as lithium metal at higher states of charge. While the Ag nanoparticles in the interlayer do not increase the critical current density required to prevent dendrite formation, they play a crucial role in promoting more homogeneous deposition of Li and Li-Ag alloy at the current collector interface. This uniform deposition is essential in reducing uneven Li plating, a key factor in preventing short circuits and enhancing battery stability[36]

The literature provides extensive insights into the intriguing effects of various buffer layer architectures on the performance of solid-state batteries (SSBs). While numerous studies have thoroughly examined the performance of different metals in buffer layers[37–40] and explored various carbon-metal deposition techniques[41–43], a detailed microscopic explanation of the lithiation and delithiation mechanisms remains lacking. Therefore, in Chapter 3, we present a comprehensive explanation of the working principles of the Ag/C buffer layer, utilizing first-principles atomistic and continuum modeling techniques.

1.4 Dissertation overview

The work presented in this dissertation was undertaken with the broad goals of 1)Providing a clear understanding of the mechanisms of dendrite growth in solid electrolytes (SEs) within solid-state batteries (SSBs). 2) Developing and exploring potential solutions to halt dendrite formation in SSBs. To achieve these objectives, we employed a combination of experimental and computational techniques, contributing valuable insights and advancements to the solid-state

battery field. Through a systematic investigation, this dissertation aims to address one of the most critical challenges in the development of SSBs, ultimately paving the way for safer, more reliable, and higher-performing energy storage solutions.

Chapter 2: we investigate the impact of solid-electrolyte (SE) pellet density on the failure mechanisms of solid-state batteries. Our findings reveal that when the SE achieves a density of 95%, a significant shift in the pore microstructure occurs. Below this threshold, the pores form a percolating network, while above it, the structure becomes non-percolating. This transition correlates with the cell failure behavior: below 99.5% density, the cells are prone to short-circuiting under applied current density, whereas above this density, the cells demonstrate significantly improved longevity.

Chapter 3: we explore the working principles behind the use of an Ag/C buffer layer in anode-free lithium metal solid-state batteries. Utilizing first-principles atomistic and continuum modeling techniques, we investigate how the Ag/C BL contributes to enhanced performance. Our results reveal that the Ag–Li alloy acts as a homogeneous solid solution during lithiation, with Ag maintaining a positive potential even at high lithiation states. We identify multiple factors driving predominant lithium deposition at the current collector/ buffer layer interface and the migration of Ag toward the current collector.

Chapter 4: we explore the potential of Ag nanoparticles to suppress lithium dendrite propagation in solid electrolytes, a critical challenge in the commercialization of solid-state batteries with lithium metal anodes. Our study demonstrates that Ag nanoparticles effectively mitigate two primary failure mechanisms: dendrite growth within porous networks at low current densities and stress-induced SE fracture at higher current densities (12.8 mA/cm^2). We also reveal that Ag nanoparticles migrate with advancing Li dendrites, promoting uniform dendrite growth and reducing localized stress. This uniform distribution of Li facilitated by Ag nanoparticles could potentially enable higher charging rates in SSBs.

Chapter 2: Effect of Solid-Electrolyte Pellet Density on Failure of Solid-State Batteries

2.1 Foreword

The work presented in this chapter is based, often verbatim, on the following publication:
Diallo, M.S.; Shi, T.; Zhang, Y.; Peng, X.; Shozib, I.; Wang, Y.; Miara, L.J.; Scott, M.C.; Tu, Q.H.; Ceder, G., "Effect of solid-electrolyte pellet density on failure of solid-state batteries." *Nature Communication* **15**, 858 (2024).

2.2 Abstract

Despite the potentially higher energy density and improved safety of solid-state batteries (SSBs) relative to Li-ion batteries, failure due to Li-filament penetration of the solid electrolyte and subsequent short circuit remains a critical issue. Herein, we show that Li-filament growth is suppressed in solid-electrolyte pellets with a relative density beyond ~95%. Below this threshold value, however, the battery shorts more easily as the density increases due to faster Li-filament growth within the percolating pores in the pellet. The microstructural properties (e.g., pore size, connectivity, porosity, and tortuosity) of $75\%Li_2S - 25\%P_2S_5$ with various relative densities are quantified using focused ion beam–scanning electron microscopy tomography and permeability tests. Furthermore, modeling results provide details on the Li-filament growth inside pores ranging from 0.2 to 2 μm in size. Our findings improve the understanding of the failure modes of SSBs and provide guidelines for the design of dendrite-free SSBs.

2.3Introduction

Among alternatives to conventional Li-ion batteries, solid-state batteries (SSBs) show potential for higher energy density and improved safety because they may enable the use of Li-metal anodes and replacement of flammable liquid electrolytes with solid electrolytes (SEs).[17,44] Computational [27,45] and experimental efforts have led to the discovery of SE materials including $Li_7La_3Zr_2O_{12}$ (LLZO) [46], $Li_2S - P_2S_5$ (LPS) [47], and Li_6PS_5X [26] with high ionic conductivities comparable to those of liquid electrolytes ($\sim 10^{-3}$ S/cm). However, further improvement of the processability and scalability of these materials is critical for their commercialization. [7] The processing conditions of SEs, such as the fabrication pressure and processing temperature, significantly affect the measured ionic conductivity [48], likely leading to the large discrepancies in reported values. [49] The ionic conductivity of LLZO increases from 10^{-6} to 10^{-4} S/cm upon increasing the sintering temperature from 1000 ℃ to 1150 ℃, with a corresponding decrease in the porosity from 6.59% to 4.52%. [50] Likewise, the conductivity of LPS increases from 3×10^{-4} to 1.1×10^{-3} S/cm when increasing the fabrication pressure during hot pressing (200 ℃) from 47 MPa [51] to 270 MPa [23], with a corresponding increase in the relative density from 85% to 98%.

Intuitively, optimizing the relative density should not only increase the ionic conductivity of the SE but also suppress Li-dendrite growth. However, extensive studies have demonstrated Li-filament penetration of LPS[52] and LLZO[53] regardless of their density or crystallinity.[54,55] Many studies have indicated that the penetration may be related to low ionic conductivity at grain boundaries[56], inhomogeneous plating at the Li metal/SE interfaces[57], electronic conductivity in the SE[28,58], low relative density of the SE[59], and pre-existing microstructural defects (such as cracks and pores) on the surface of and in bulk SEs[60]; however, consensus on the mechanism in various SEs has not yet been reached. As most of these factors are influenced by the fabrication conditions, it is important to quantify the effect of processing parameters such as the densification pressure on the micro- and macrostructural properties (e.g., porosity, tortuosity, pore networks) of the SE and on the failure of SSBs due to Li-filament growth.

In this work, we provide insight on the failure mechanism of SSBs due to Li-filament growth by investigating the effect of the fabrication pressure on the micro- and macrostructure of LPS. We first show that fully dense LPS SE (relative density >99%) is produced at fabrication pressures above 600 MPa. The ionic conductivity increases linearly during densification of the LPS pellet, as reported in similar studies.[23,51] However, the failure behavior of SSB cells as a function of densification is found to be more complicated: a symmetric cell (Li|LPS|Li) fails much faster as the density of the LPS pellet increases, before reaching a critical relative density (~95% for a fabrication pressure of 500 MPa) beyond which cell failure does not occur. To explain this highly non-linear failure behavior the micro- and macrostructure (pore size and connectivity, porosity, tortuosity) of LPS pellets are quantified using surface scanning electron microscopy (SEM), focused ion beam (FIB)–SEM tomography, and pellet-permeability tests, revealing that the pore networks formed during processing play a key role in the failure of SSBs. Our modeling results

confirm the much higher Li-filament growth rate (and therefore faster cell failure) in denser pellets because of the much smaller pore sizes.

2.4Results

Figure 2.1-a confirms that the relative density of the LPS pellet was well controlled by the fabrication pressure, with an almost fully dense LPS pellet (99.9%) obtained at a fabrication pressure of 700 MPa, consistent with previous results.[23] *Figure 2.1-b* presents Nyquist plots from sequential electrochemical impedance spectroscopy (EIS) measurements of the LPS pellet with a density of 95.3% (LPS-95.3%). The real part of the impedance increases for the initial 2 h, before leveling off for the remaining 10 h, behavior consistent with a chemical reaction between LPS and Li metal[61] and early passivation of the solid-electrolyte interphase (SEI).[53,62] *Figure 2.1-c* clearly shows the strong effect of the pellet density on the bulk (SE+SEI) resistance and its temporal evolution as well as passivation of all the cells during the initial 2 h. As depicted in *Figure 2.1-d*, the ionic conductivity linearly increases with increasing LPS density, and the initial overpotential decreases.[51] The increase in conductivity is likely related to the increase in contact area between the LPS particles at higher density.

The effect of the LPS pellet density on Li-filament growth was investigated through electrochemical (EC) measurements. A total of 35 cells (5 cells per LPS density) were charged with a current density of 0.2 mA/cm^2 until failure of the cell or depletion of the counter electrode. Failure occurred when the voltage dropped to zero and depletion occurred when the voltage rapidly increased to the cutoff value (1 V). *Figure 2.2-a* presents the voltage curves of four representative cells with different LPS pellet densities. Cell shorting took longer for LPS-81.8% (18 h) than for LPS-89.2% (16 h) and LPS-95.3% (8 h), whereas depletion was observed in the LPS-99.9% cell after charging for more than 40 h.

Figure 2.2-b summarizes the effect of the LPS pellet density on the cell survivability. Each data point is the average of 5 measurements, with the detailed EC results for each cell presented in *Figure SI-2.4*. As the LPS relative density increases from 81.8% to 95.3%, the cell-shorting time decreases; however, cell shorting does not occur above a pellet density of 95.3%. Instead, depletion was observed in all the LPS 98%–100% cells, as highlighted in *Figure SI-2.5*, with a clean surface of the counter electrode (stripping side) at the end of the EC experiments.

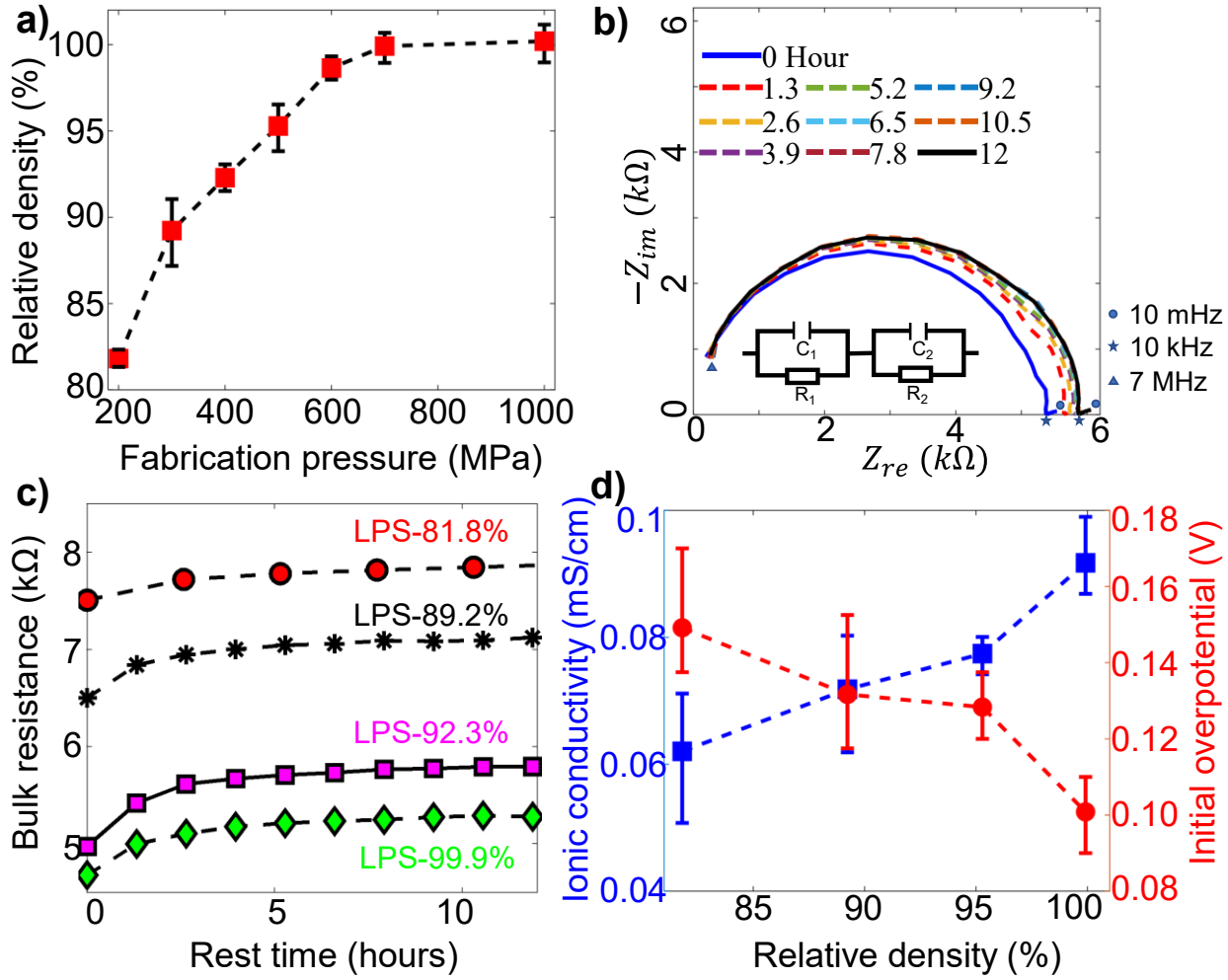

Figure 2. 1. Effect of pellet density on cell resistance; error bars are defined as standard deviation. **a)** Relative density of LPS pellet for various fabrication pressures (theoretical LPS density of 1.88 g/cm^3). **b)** Nyquist plots from sequential EIS measurements (with time interval of 1.3 h) of Li|LPS|Li symmetric cell (with LPS pellet relative density of ~89.5%). All the intermediate curves (dashed lines) are enveloped by the initial ($t = 0$ h, blue solid line) and final ($t = 12$ h, blue solid line) curves. **c)** Temporal evolution of bulk (SE+SEI) resistance of symmetric cells with four different LPS relative densities. **d)** Ionic conductivity (blue curve) of LPS pellets and the initial overpotential (red curve) of the cell at current density of 0.2 mA/cm^2.

Figure 2.2-c presents a schematic of our hypothesis explaining the non-monotonic relation between the cell-shorting time and the LPS pellet density. At lower density, the LPS pellet is more porous with larger and interconnected pores, whereas the pores become smaller and more isolated at higher density.[50]. As a result, a pore network connecting two electrodes may exist in low-density LPS pellets, indicated as the "pore-percolating zone" (orange area in *Figure 2.2-c*), whereas in high-density pellets, the pores become non-percolating (green area in *Figure 2.2-c*). These microstructural features are responsible for the shorting behavior of the symmetric cells observed in *Figure 2.2-b*: (1) Li filaments propagate easily in the percolating pores until shorting

occurs when the LPS density is low (pore-percolating regime); however, propagation is suppressed by the non-percolating pores when the LPS density is in the non-percolating zone. (2) Within the pore-percolating regime, Li filaments propagate faster with decreasing pore size, causing faster cell shorting because of the reduction in the fillable volume.

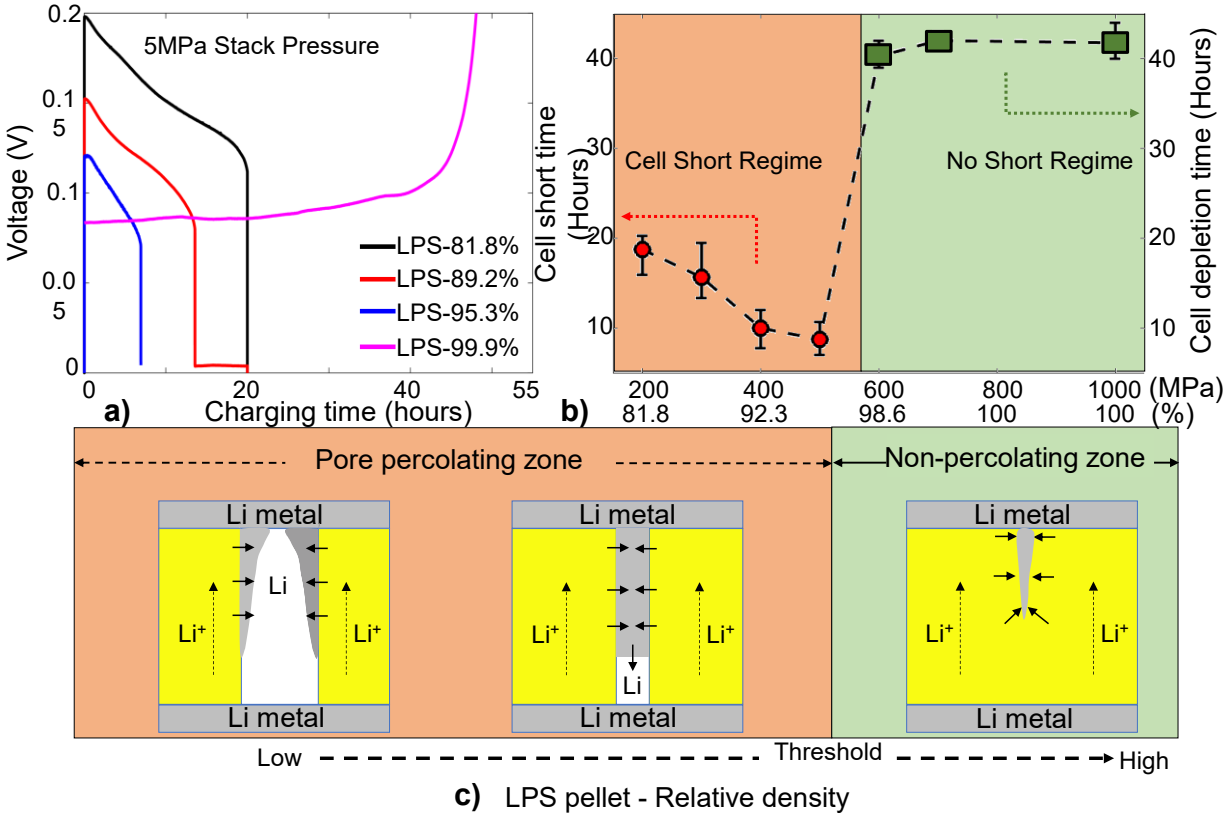

Figure 2. 2. Effect of pellet density on Li-filament growth; error bars are defined as standard deviation. **a)** Charging voltage of cells with different LPS pellet densities. **b)** Cell-shorting time ("cell-shorting regime") as a function of fabrication pressure and LPS relative density and threshold where the cell voltage increases rapidly ("no-short regime"). **c)** Schematic of Li deposition within pores of LPS pellets with different pellet densities. Symmetric cells in the "percolating regime" have pore networks connecting two electrodes in the initial microstructure, whereas those in the "non-percolating regime" have no connecting pore network initially.

To validate the aforementioned hypothesis, quantitative analyses of the pore microstructure and connectivity were performed using FIB–SEM tomography and permeability tests. The pore structures in the $(50\ \mu m)^3$ volume from different pellets (LPS-89.2%, LPS-95.3%, LPS-99.9%) are shown in *Figure 2.3-a, c*, respectively, with the different colors representing different interconnected pore networks. The pores are large and well connected in the LPS-89.2% cube, as exemplified by the largest pore network shown in red occupying most of the total pore volume. In contrast, the pores in the LPS-95.3% cube are small and connected, whereas the pores in the LPS-99.9% cube are small and isolated. The pore size, porosity, and connectivity (defined as the ratio

between the largest pore volume and the total pore volume) of the three cubes were calculated statistically and are summarized in Table-2.1, with details provided in *Figure SI-2.6* and *SI-2.7*.

Figure 2.3-d depicts the relation between the outlet Ar gas flowrate Q and the pressure gradient ($\Delta P = P_0 - P_{atm}$) across LPS pellets with varying densities, showing that a higher Ar gas flux was measured for LPS-81.8% and LPS-89.2%, whereas little to no Ar gas flux was measured for LPS-95.3% and LPS-99.9%. These results confirm the presence of percolated pores in the low-density pellets and non-percolated pores in the high-density pellets. A more quantitative permeability analysis based on the modified Darcy's law[63,64] in the SI (The permeability tests and analysis) shows that their respective permeability values are $k_{82\%} = 1.50 \times 10^{-3}\mu m^2$, $k_{89\%} = 3.86 \times 10^{-4}\mu m^2$, $k_{95\%} = 1.82 \times 10^{-5}\mu m^2$, and $k_{99\%} \approx 0$.

Table-2. 1. FIB/SEM characterization analysis

Bulk LPS pellet density (%)	89.2	95.3	99.9
Porosity (%)	8.43	2.28	0.01
Connectivity (%)	76.8	4.88	3.34
Pore size (μm)	0.5–1.5	0.2–0.8	<0.1

Electro-chemo-mechanical modeling was employed was employed to quantify the Li propagation rate within pores in SE pellets .[28,65] Li-ions conduction in the SE is described by Ohm's relation, the Li electrodeposition on SE/anode interface is described by the Butler-Volmer relation, and the Li deformation in the SE pore is described by visco-elastoplastic mechanics[66,67]. More details are provided in the Method section. *Figure 2.4-a* presents a simplified model to describe the growth of Li (gray area) within a pore (white area) present in the LPS pellet (yellow area) near the Li-metal anode. Li ions are stripped from the counter electrode at the bottom, conducted through the SE, and deposited at the interface between the LPS and the top Li-metal electrode (line AB and CD) and the surface of the pore (line BE and CF). Li initially deposits at the three-phase corner at location B and C, where both Li^+ ions (from LPS) and electrons (from the Li metal anode) are available for the reducing reaction ($Li^+ + e^- \rightarrow Li$). The four dashed lines represent the Li boundary at four charging times ($0.5, 1.0, 1.5, 1.9$ h) under a current density of $0.2\ mA/cm^2$. The metallic Li grows both radially and longitudinally toward the counter electrode. For example, it takes 1.9 h to close a 2-μm-diameter pore while growing to a depth of 2.5 μm in the LPS pellet. *Figure 2.4-b* shows the deposition current along the interface (line A–B) and the pore surface (line B–E) at the four charging times, with the detailed distribution of ionic current and overpotential within the SE shown in *Figure SI-2.11*. The current reaches a maximum at the advancing tip of the Li filament (location E) due to the lower resistance to reach this point. This maximum current density increases as the Li filament grows towards the counter electrode, from $0.5\ mA/cm^2$ at $t = 0.5$ h to $1.0\ mA/cm^2$ at $t = 1.9$ h. It should be noted that this local current density is five times the nominal current.

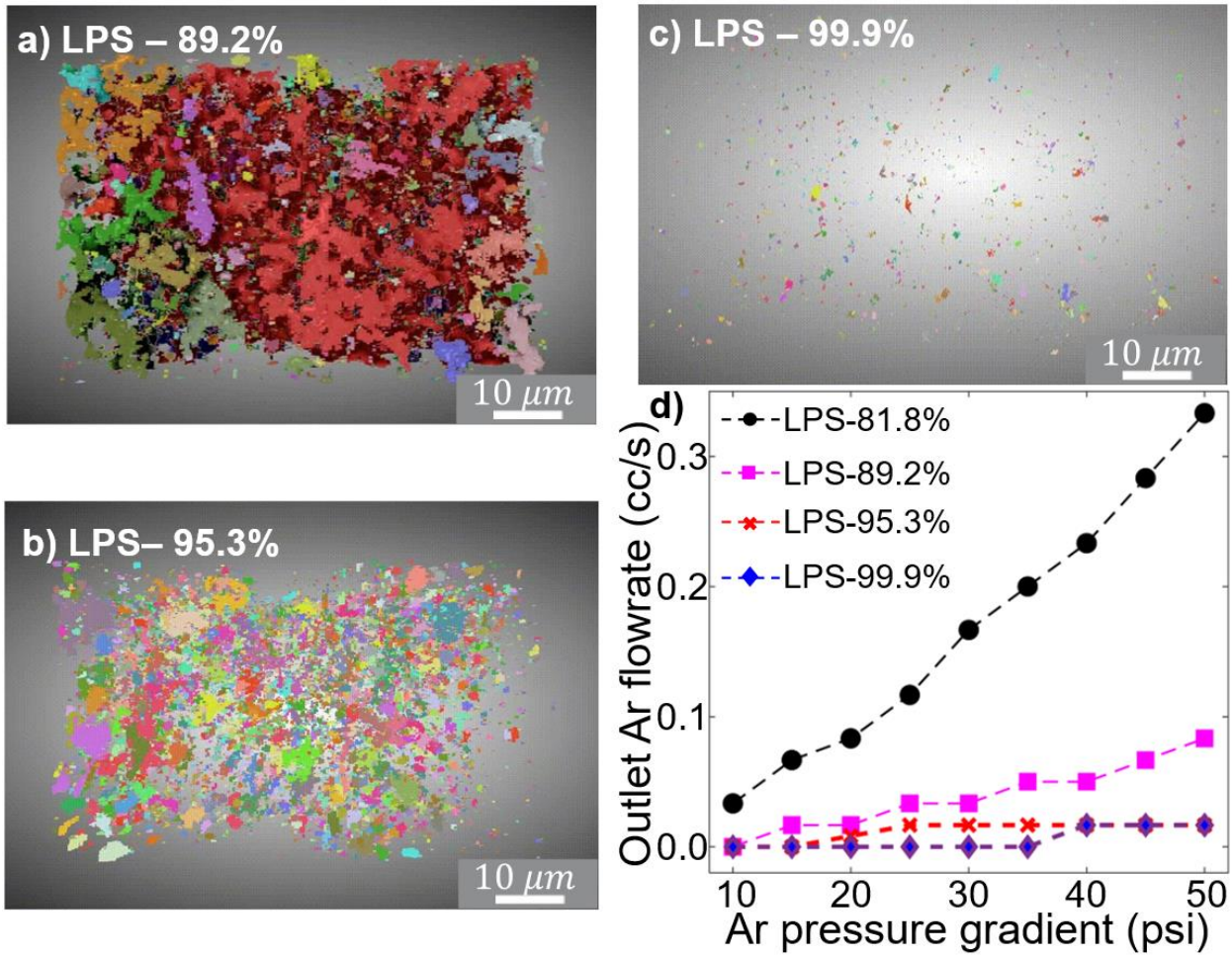

Figure 2. 3. Characterizations of micro- and macrostructure of LPS. 3D structure of pores within the LPS pellets at densities of a) 89.2%, b) 95.3%, and c) 99.9%. d) Flowrate of Ar gas flowing out of LPS pellet as a function of Ar pressure gradient across the pellet.

When the Li width ($W = w_1 + w_2$) reaches the pore size (D_{pore}) the radially deposited Li will start to extrude longitudinally. For example, when $t > 1.9$ h in *Figure 2.4-a*, the newly deposited Li extrudes longitudinally, which accelerates the Li-filament propagation. *Figure 2.4-c* shows the starting time of Li extrusion for three different pore diameters: 0.5 μm (green line), 1 μm (blue line), and 2 μm (red line), which takes 0.63, 1.0, and 1.9 h, respectively. *Figure 2.4-d* presents the propagation length of the Li filaments perpendicular to the electrodes within these pores. These results confirm the important fact that Li filaments indeed grow much faster towards the opposite electrode for smaller pore sizes. But the growth appears bilinear, rather than linear in time due to the changing mechanism as the pore is filled. Notably, the Li extrusion starts at $t = 1.9$ h in the 2μm pore but accelerates at $t = 2.9$ h (*Figure 2.4-d*). This is because the extruded Li needs to first fill in the void space (such as the area in B–C–F–E in *Figure 2.4-a*), which takes 1 h for the 2-μm pore. The stable Li growth rate r_{Li} after the acceleration can be obtained from *Figure 2.4-d*, with the maximum $(20.7\ \mu m/h)$ observed for the smallest pore $(0.5\ \mu m)$, followed by 10.3 and

5.1 µm/h for the 1-µm and 2-µm pores, respectively. This Li growth rate from the simulation can be directly compared with the cell-shorting time presented in *Figure 2.2-b*.

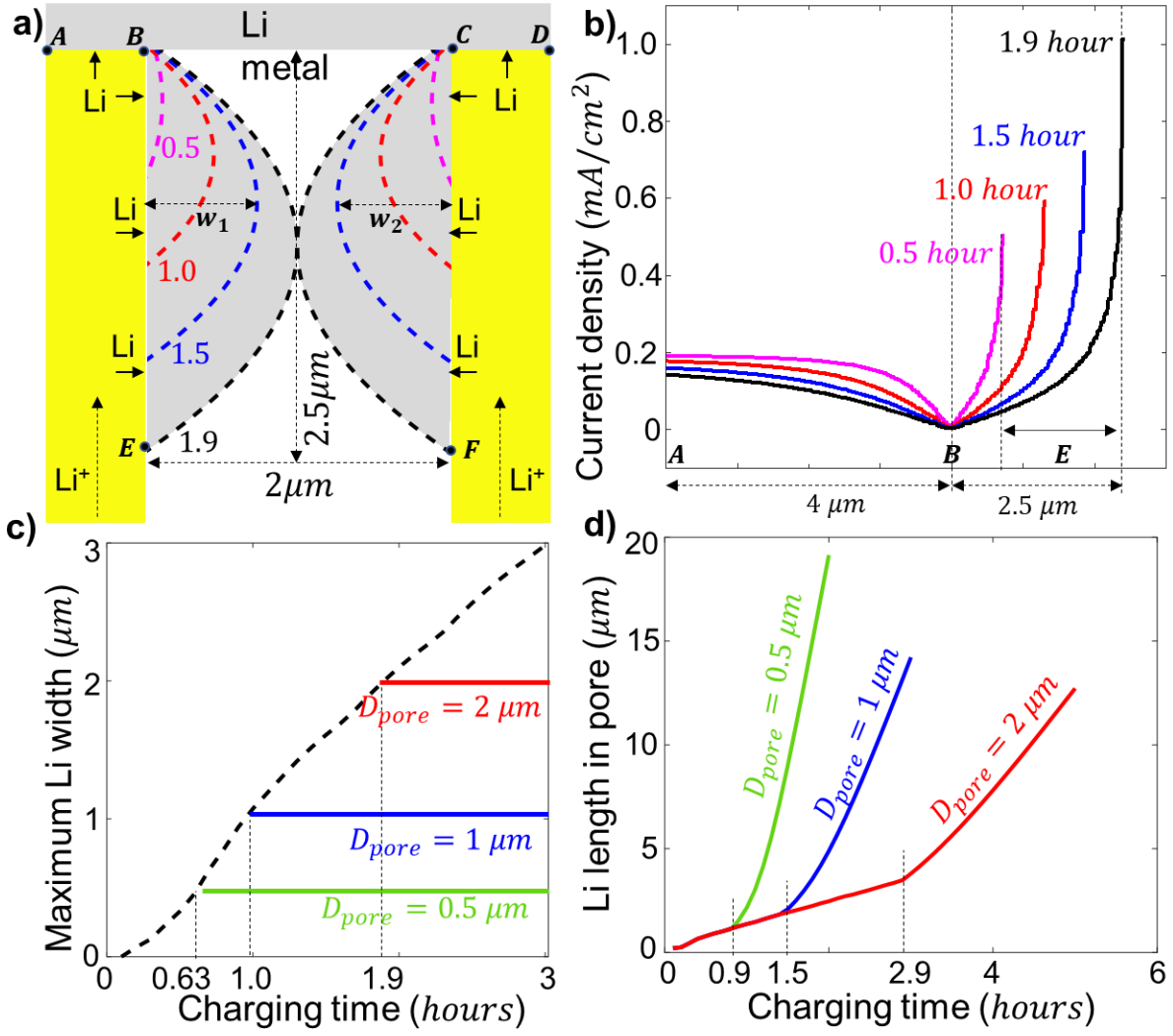

Figure 2. 4. Simulation of Li deposition in SE pores. (a) Boundaries (dashed lines) of Li filament (gray area) at different charging times (in h) within a pore of 2-µm diameter. The Li metal on the top is the anode during charging. The maximum Li width at a specific time is the summation of the Li width on each side ($W = w_1 + w_2$). **(b)** Deposition current density along line A–B–E at different charging times. The labels "A", "B", and "E" along the x-axis correspond to locations A, B, and E in 4a. Note that location E changes at different time steps. **(c)** Maximum Li width in the pore when $D_{pore} = 10\ \mu m$ (dashed black line), $D_{pore} = 2\ \mu m$ (red line), $D_{pore} = 1\ \mu m$ (blue line), and $D_{pore} = 0.5\ \mu m$ (green line). **(d)** Length of Li filament in the pore when $D_{pore} = 2\ \mu m$ (red line), $D_{pore} = 1\ \mu m$ (blue line), and $D_{pore} = 0.5\ \mu m$ (green line).

2.5Discussion

Our experimental observations in *Figure 2.2-b* demonstrate the non-monotonous behavior of shorting time with pellet density. This finding implies that two different density regimes exist: In the percolating-pore regime a higher degree of densification actually leads to more rapid shorting as the volume of pores that need to be filled decreases. Beyond a critical density where pores no longer percolate, simple growth of Li filaments through the conductor pellet is no longer possible and other mechanisms need to become active to shorten the cell. Indeed, while we find no shorting at low current density for the densest pellet, shorting of the cell can still be achieved at high current density, implying that in the non-percolating regime current-dependent mechanisms, such as stress build up[68] or internal Li deposition due to electron leakage[28,69] may contribute to failure. It should be noticed that the SE surfaces also vary with LPS relative density, as described in *Figure SI-2.6*. This surface variation may affect the nucleation and the initial growth of Li filaments, but in our case, this does not appear to modify the cell short-circuiting. This is likely since most Li filaments grow into existing pores in the bulk SE and this growth lasts until the cell failure.

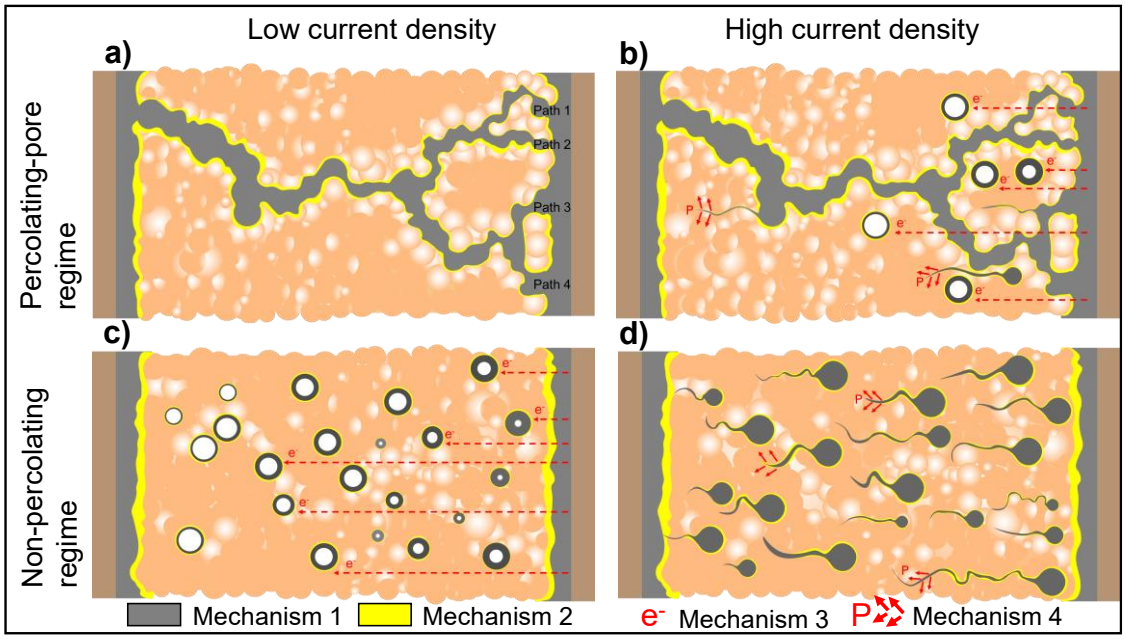

Figure 2. 5. Schematics of Li-filament (Gray) growth in the solid electrolyte (Orange) at different conditions. **a)** Li (gray) deposit within the tortuous pore network at low current density with multiple branches and varying thickness. The yellow line represents the SEI layer formed due to the chemical reaction between LPS and the Li filament. **b)** Li (Gray) deposit within the tortuous pore network and isolated pores at high current density. **c)** Li deposit in isolated pores at low current density. **d)** Li deposits in isolated pores and causes fracture at high current density. Four identified mechanisms in the symmetric SSB: percolating pores (Mechanism 1), chemical reaction (Mechanism 2), electronic conductivity (Mechanism 3), and SE fracture (Mechanism 4). Li metal, the SEI layer, and voids are colored gray, yellow, and white, respectively. The dashed lines for Mechanism 3 represent electron conduction due to electronic conductivity of the SE. The red arrows for Mechanism 4 represent the fracture directions of the SE due to the development of hydrostatic pressure **P**.

Our modeling results, incorporating both transport and mechanics confirm the hypothesis built from the experiments: Pore walls are observed to fill with lithium in a droplet-like geometry grows counter to the Li^+ flow, along a distance that is multiple times the pore diameter. For example, the 0.5µm pore fills over a length of 20µm even after only 1.5 hours charging at 0.2mA/cm^2. It is challenging to make a quantitative comparison between our simulations and experiments as in reality percolating pore networks are tortuous, have varying radius along the path, and may join and branch, as shown schematically in *Figure 2.5* and for a real pellet in Figure SI-2.10. However, the general conclusion drew from the model still holds larger pores in the SE enable the cell survives longer time than smaller pores.

Although this paper emphasizes the importance of pellet density on SSB failure due to Li-filament propagation through percolating pores, it should be noted that this is not the only mechanism but simply an easier path for Li-filament growth compared with SE fracture[70], electrochemical reaction[71], and SE electronic conductivity.[69] The four different mechanisms that have been identified as being responsible for Li-filament growth within the solid-state cell are illustrated in *Figure 2.5*: 1) propagation through a percolating pore network, 2) growth of the SEI due to chemical reaction of SE and Li, 3) isolated Li deposition due to electronic conductivity of the SE, and 4) Li penetration and SE fracture at higher current density. Mechanism 1 (percolating pores) discussed in this paper is the most prevalent cause of SSB failure because most SE pellets used in the literature never reach the required threshold density (>95%), as discussed in *Figure 2.2*. Lithium filaments prefer to propagate inside the percolating pores first because very low overpotential is needed for the growth. Mechanism 2 (chemical reaction) is present when the SE material is chemically unstable against Li metal, as is the case for all sulfides and some oxides. It has been reported that SSB failure can occur via this mechanism if an unstable SEI layer is formed.[71] Our results *in Figure 2.1-c* indicate that the chemical reaction between the Li metal and LPS pellet occurs in the first 2 h but stops after a stable SEI layer is formed. Therefore, this mechanism has limited effect in our study. Mechanism 3 (electronic conductivity) enables Li-metal deposition in the isolated pores in the SE, which eventually become interconnected and short the SSB once the percolating point is reached.[28,69] Given the non-negligible electronic conductivity ($\sim 10^{-4}$ mS/cm) of LPS we performed a control experiment using a buffer layer of Li_3N+LiF[32] to limit the possible transfer of electrons into the SE. The results shown *Figure SI-2.12* produced similar observations as those in *Figure 2.2* indicating that electron conductivity plays a minor role when the pellet is in the percolating pore regime. Mechanism 4 (SE fracture) can be observed when the SE material has low fracture toughness, and a high current density is applied.[72] As a large overpotential (or mechanical stress) is needed to trigger this mechanism, SE fracture is not likely to occur when a percolating pore network pre-exists in the LPS pellet but may become important for pellets in the "non-percolating regime" at escalated external current. Our control experiment in *Figure SI-2.13*, confirms that a short circuit can still occur in dense pellets without percolating pores (LPS-99.2% and LPS-99.9%) under higher applied current densities (3.2 and 6.4 mA/cm^2, respectively), further pointing at a current-dependent failure mechanism in this regime.

While these four mechanisms are usually entangled, it is worth noting that Mechanism 2 (chemical reaction), Mechanism 3 (electronic conductivity) and Mechanism 4 (SE fracture) are related to the material properties of the selected SE, whereas Mechanism 1 (percolating pores) is dependent on the microstructure of the SE pellet. Therefore, the detailed observations highlighted in the Results section are not exclusive to sulfide battery systems. The threshold relative density (~95% for the LPS used in this work) for closing the percolating pore network is a general requirement for the SE pellets made from other SE materials. This discovery explains the puzzling results reported in many works that Li dendrites still propagate into SEs even when the SE pellets are very dense. For example, it was reported that LLZO, even with a density close to that of a single crystal, can still have Li filaments propagating through.[30]

A straightforward solution to prevent percolating pores in SE pellets is to prepare a sufficiently dense pellet using various fabrication methods (cold pressing, hot pressing, high-temperature sintering, etc.). However, it can be challenging to densify certain SE materials, such as oxide materials. Unlike sulfides, which are soft enough for cold pressing, oxide SEs require high sintering temperature to achieve good densification. Several solutions for the densification of ceramics have been investigated with no breakthroughs yet, making the path to densification difficult.[28,73] Therefore, alternative methods should be explored. For example, the use of an interlayer or additives in the SE to reduce Li deposition in pores, or engineering on the pore connectivity in the SE to prevent the percolating network, etc.

The understanding of the mechanisms by which the current affects the propagation of Li within the SE is still puzzling. It is recognized that the growth of Li dendrites within the SE alters the distribution of local current, leading to an intensified current at the tip of the dendrite. Consequently, this results in a shift of the plating potential (the voltage at which plating, or deposition of Li occurs) inside the SE, deviating the 0V potential.[31,65,74–77] However, the specific length scale at which this current focusing occurs in the lateral direction of the SE relative to the dendrite tip remains uncertain. Further investigation is necessary to determine the spatial extent over which the intensified current is concentrated around the dendrite tip.

A systematic investigation of the effect of LPS-pellet fabrication pressure (or relative density) on the failure mechanism of SSBs was performed. We showed that SSBs with denser SE fail more easily before a critical relative density is reached; after which failure is prevented. The most prevalent failure mechanism is the Li-filament growth in percolating pores within the SE, which is suppressed when the pores become isolated and small in high density pellets above the critical relative density (>95%). While different processing conditions (such as hot, warm, or cold pressing) may be required to obtain dense SE pellets, the critical relative density requirement for closing the percolating pore networks appears to be independent of the choice of SE material. Our study provides a quantitative guide for relative density optimization of SE pellet to prevent one of the most prevalent failure modes for Li-filament growth.

2.6Methods and supplementary results

Preparation of Li|LPS|Li Cell: Glassy LPS material was synthesized by ball milling 75% Li_2S (99.9% metal basis, Alfa Aesar) and 25% P_2S_5 (99.9% metal basis, Alfa Aesar) for four hours. The Li|LPS|Li cell was prepared in the following sequence. Symmetric lithium electrodes were prepared by rolling Li-metal chunks (99.9% metal basis, Alfa Aesar) onto copper foil. The cells were assembled using an in-house-designed cell-making toolkit (as illustrated in *Figure SI-2.1*). A constant stack pressure of 5 MPa was applied to the cell to maintain the conformal Li–SE interfacial contact. Notably, the symmetric cell was assembled inside a small PEEK tube, which may be subjected to non-negligible deformation when very high pressing pressure is applied. This deformation changes the diameter of the cells; accordingly, therefore, the final cell diameter should be calculated, with detailed simulation in *Figure SI-2.2*.

Electrochemical Cycling and Electrochemical Impedance Spectroscopy: Each cell was tested following two sequential stages: 1) Initial rest stage: the cells were rested for 12 h after assembly under the stack pressure. EIS measurement was conducted every 1.3 h to monitor the temporal evolution of both the bulk and interfacial resistances. 2) Electrochemical (EC) cycle stage. The charge, cycling, and EIS measurements were performed using a potentiostat (VMP-300, BioLogic). The EC and EIS measurements were conducted in a temperature chamber to ensure a constant cycling temperature. The EC measurements were performed using a current $i = 15.84\ \mu A$, with an electrode diameter $d = 3.175$ mm to maintain the current density at $J = 0.2\ \frac{mA}{cm^2}$. The current was increased later in the investigation to adjust the current density criteria. The EIS measurements were conducted at a frequency ranging from 10^{-3} to 7×10^6Hz.

Focused ion beam and scanning electron microscopy: FIB–SEM characterization was performed on an FEI Helios G4 dual-beam FIB system equipped with a Ga^+ ion beam, as shown in *Figure SI-2.6*. Consecutive slice milling and image acquisition were performed using the FEI Slice and View software. LPS pellets of varying densities were cut in the normal direction using FIB and characterized using SEM under a tilt angle of 52°.

Image processing and reconstruction: The resulting SEM image stacks were first rescaled to compensate for the 52° angle between the electron beam and sample cross-section. Then, several representative slices were selected, and manual segmentation of different components (LPS and void) was performed. The manually segmented images were used to train a classifier using the Trainable Weka Segmentation plug-in in the ImageJ software, which was then used to segment the entire image stack. All the 3D reconstruction and visualization were reconstructed using the Dragonfly software from 100 cross-sectional slides with each slice 50 nm thick.

Permeability tests: The permeability tests were performed by pumping Ar gas through a custom-made piping and hose system, as shown in *Figure SI-2.9*. The inlet flow of Ar gas was measured and compared with the outlet Ar gas flow, which was used to determine the permeability of the tested sample. The LPS pellet was sealed inside two cylindrical tubes, with

Ar gas flowing into the pellet from the bottom tube and flowing out to the top tube. The pneumatic pressure (P_{in}) of the inlet Ar gas in the bottom tube was controlled by the valve on the Ar tank. The flow rate (Q) of the outlet Ar gas in the top tube was measured using a highly sensitive flow meter (sensitivity of $0.01\ cc/s$). The pneumatic pressure (P_{out}) of the outlet Ar was measured very close to the atmospheric pressure ($P_{out} = P_{atm}$).

Modeling of Li deposition in pores: Both the Li electrodeposition and interfacial contact loss are affected by the charge-transfer reactions (described by the Butler-Volmer relation), mass transfer in the SE (described by the Ohmic relation), and interfacial contact mechanics (described by elastoplastic continuum mechanics). A comprehensive approach combining Li electrodeposition, mass transport with elasticity and plasticity of both the Li metal and SE used in the model through coupled PDEs. A brief list of relevant PDEs is provided in the following, with a more detailed description of the individual physics and corresponding PDE in our earlier similar modeling work.[28,65]

Quasi-static mechanical equilibrium is assumed for both Li metal and the SE:

$$\nabla \cdot \boldsymbol{\sigma} = 0 \qquad (1)$$

Linear elasticity is assumed for the elastic state of both Li metal and the SE:

$$\boldsymbol{\sigma} = \frac{E}{1+\nu}\boldsymbol{\varepsilon} + \frac{\nu E}{(1+\nu)(1-2\nu)}\mathrm{trace}(\boldsymbol{\varepsilon})\mathbf{I} \qquad (2)$$

An elastic/perfect plastic model without hardening is assumed for the Li metal plastic flow, with the Von Mises criterion and associated flow rule:

$$\Phi(\boldsymbol{\sigma}) \equiv \sqrt{\frac{3}{2}}|\mathrm{dev}(\boldsymbol{\sigma})| - \sigma_y = 0, \qquad \mathrm{d}\boldsymbol{\varepsilon}^{\mathrm{p}} = \mathrm{d}\lambda\frac{\partial \Phi}{\partial \boldsymbol{\sigma}} \qquad (3)$$

Since the SE is a single-ion conductor, the conduction is therefore purely ohmic:

$$\nabla^2\phi_{SE} = 0, \qquad \mathbf{i} = -\sigma_{Li^+}\nabla\phi_{SE} \qquad (4)$$

At SE/Li metal interface, Butler-Volmer relation [29,72] is employed as the boundary condition:

$$i_{ct} = i_{exc}e^{\frac{(1-\alpha_a)\overline{V}_{Li}\Delta P_{Li}}{RT}}\left(\mathrm{e}^{\frac{\alpha_a F}{RT}\eta} - \mathrm{e}^{-\frac{\alpha_c F}{RT}\eta}\right), \qquad (5)$$

$$i_{ct} = -i_n = -\mathbf{i}\cdot\mathbf{n}_{\mathrm{SE}} \qquad (6)$$

An in-house-developed code based on the finite element method and the MOOSE framework[78] was implemented to solve all the coupled electro-chemo-mechanical PDEs numerically. The default values of the parameters (such as electronic/ionic conductivities for Li^+ transport in the SE

and electrons in the Li metal) used in this work were obtained from experimental measurements of LPS-type SE and are listed in the last column of Table-2.2.

Table-2. 2. Key parameters used in this work

NAME	SYMBOL	UNIT	VALUE	REF
Exchange current density at electrode/SE interface	i_{exc}^{k}	$\mathrm{mA/cm^2}$	1.3	[79]
Exchange current density at void/SE interface	i_{exc}^{V}	$\mathrm{mA/cm^2}$	0.01	[80]
Ionic conductivity in the SE	σ_{M^+}	mS/cm	0.1	[81]
Electronic conductivity in the SE	σ_{e^-}	mS/cm	10^{-4}	[69]
Electric conductivity in the M metal	σ_M	mS/cm	10^5	
Fracture toughness of the SE	K_c	$\mathrm{MPa \cdot \sqrt{m}}$	0.2	[82]
Bulk modulus of the M metal	K	GPa	11	[83]

The experimental setup and the house-designed cell making toolkit: Cells are assembled in a small PEEK tube (*Figure SI-2.1a-b*). SE (LPS) is first pressed in a PEEK small tube at different pressure, then Lithium metal is pressed at both sides of the SE. Copper foils are then placed on both ends of the Li-metal electrodes and then stainless-steel rods are used to press the cell. The cell is then placed in a testing setup (*Figure SI-2.1c*) which has a spring to control the stack pressure. The testing setup is then encapsulated in a sealed container to ensure the cell is running in an inert environment.

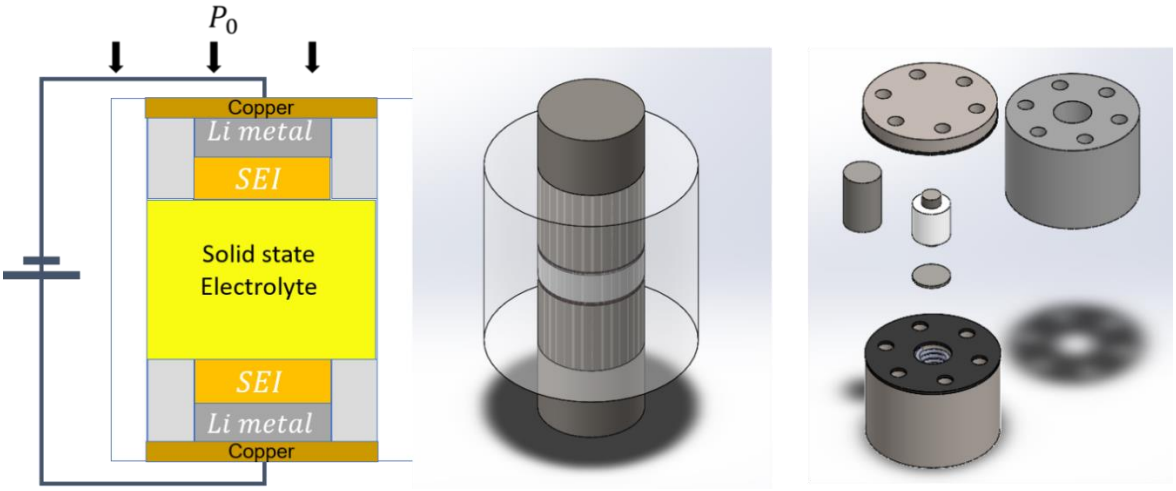

Figure SI-2. 1. The experimental setup and the house-designed cell-making toolkit.

The deformation of cell diameter due to fabrication pressure: The material for the die to make the LPS pellet is PEEK, which is subjected to non-negligible plastic deformation (6%– 8%) under high uniaxial pressures; therefore, the final cell diameter (~6.8 mm), instead of the initial value (6.35 mm), is used for the calculation of density and conductivity (*Figure 2.1-d*), with detailed calculation in *Figure SI-2.2*. This was then used to calculate the relative density of high-pressure cells.

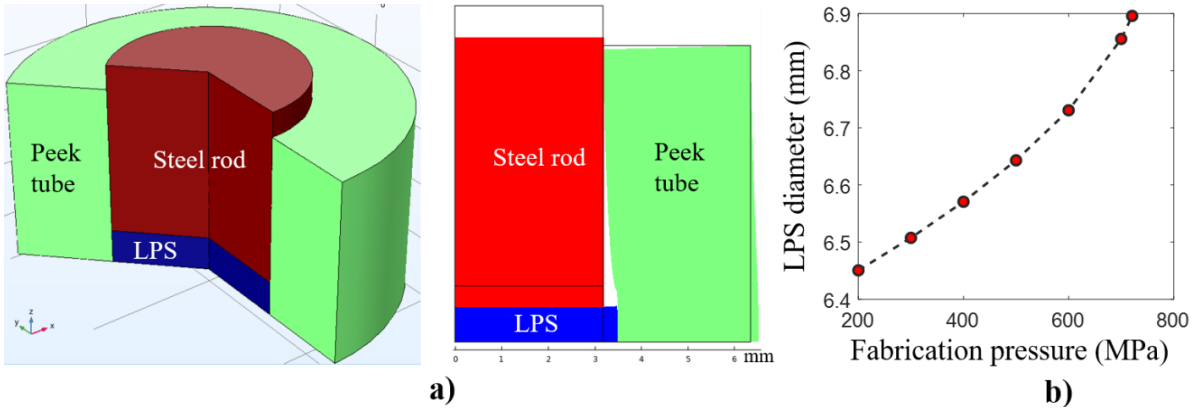

Figure SI-2. 2. The change of LPS diameter is due to the deformation of the toolkit under high fabrication pressure. (a) The shape of each part under fabrication pressure 700MPa; (b) the LPS diameters as a function of the fabrication pressure.

Figure SI-2.2. The change of LPS diameter is due to the deformation of the toolkit under high fabrication pressure. (a) The shape of each part under fabrication pressure 700MPa; (b) the LPS diameters as a function of the fabrication pressure.

The optimization of stack pressure: Stack pressure was applied on the cells as shown in *Figure-SI-2.1*. The cells were prepared with two different pressing pressure to evaluate the effect of stack pressure on both percolated and non-percolated pores pellet; LPS-89% has a percolated pore network and LPS-95% has isolated and non-percolated pores. The EIS results are plotted in *Figure SI-2.3*. We plot bulk resistance, extracted from the EIS data, vs resting time, which is the time is left without charging. We observe that for a stack pressure of 8MPa, the bulk resistance of the cells, in both the percolated and non-percolated range, decreases over time. This is because lithium metal is creeping in the LPS pellet via chemo-mechanical effects. The stack pressure applied on the SSB cell is a key parameter that affects the interfacial contact between the Li metal and LPS pellet. The interfacial resistance can be high if too low a stack pressure leads to contact loss [65], whereas SE fracture or Li extrusion into the SE pores can occur if the stack pressure is too high:[66] both cases are investigated and presented in *Figure SI-2.3* in which we show that our current experimental setup, 3-MPa stack pressure induces contact loss, whereas 8 MPa, too large, does not yield a stable interface. The optimal stack pressure in this work (~5 MPa) is different from that in related work in the literature[67], which may be due to the different wall frictions in different setups.

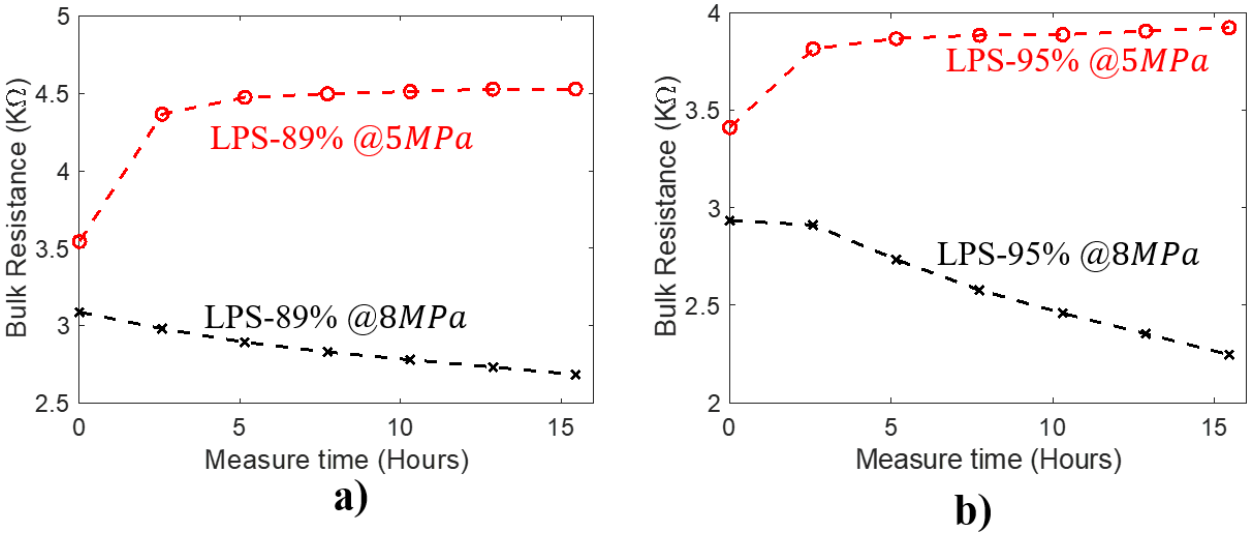

Figure SI-2. 3. Stack pressure effect. a) Comparison of bulk resistance of cell with percolated pores (a, LPS-89%) and non-percolated pores (b, LPS-95%) under two stack pressure.

The EC curves of individual LPS pellet density: The electrochemical dataset is plotted in *Figure SI-2.4* it shows all 35 cells measured with increasing density. The trend is summarized in the main body of the paper, in *Figure 2.2*. There are some noises present in the data, which are due to the sensitivity of the measurement devices, but it does not affect the results gathered. It is worth noting that, for the high-density cells, which do not short, we show in *Figure SI-2.4-e, f,* and *g* that, with varying amounts of Li-metal on the electrode the depletion time changes. We show that the depletion time can vary between 20 hours to beyond 140hours on a 600 MPa pressed pellet.

Figure SI-2. 4. Electrochemical results of all cells pressed at 200MPa, 300MPa, 400MPa, 500MPa, 600MPa, 700MPa, and 1000MPa.

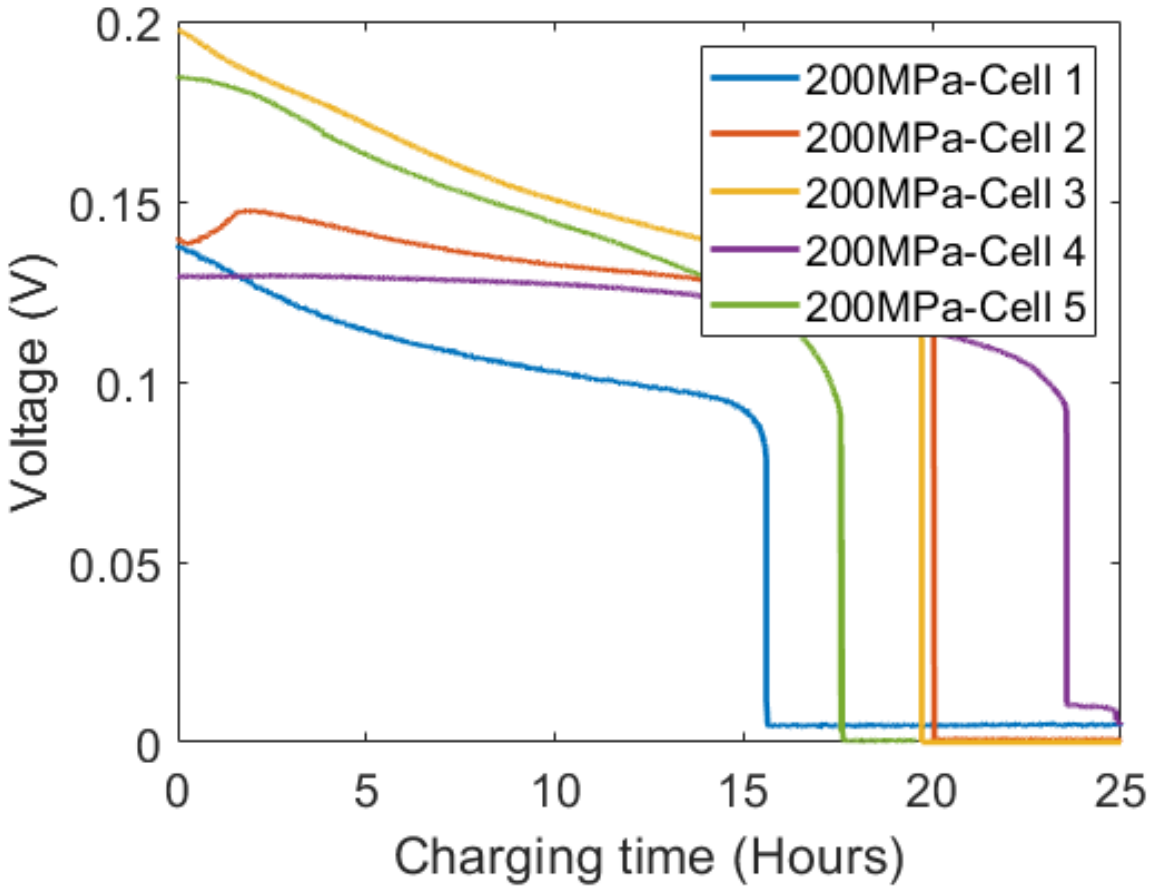

Figure SI-2.4-a. Electrochemical results of all cells pressed at pressure 200MPa.

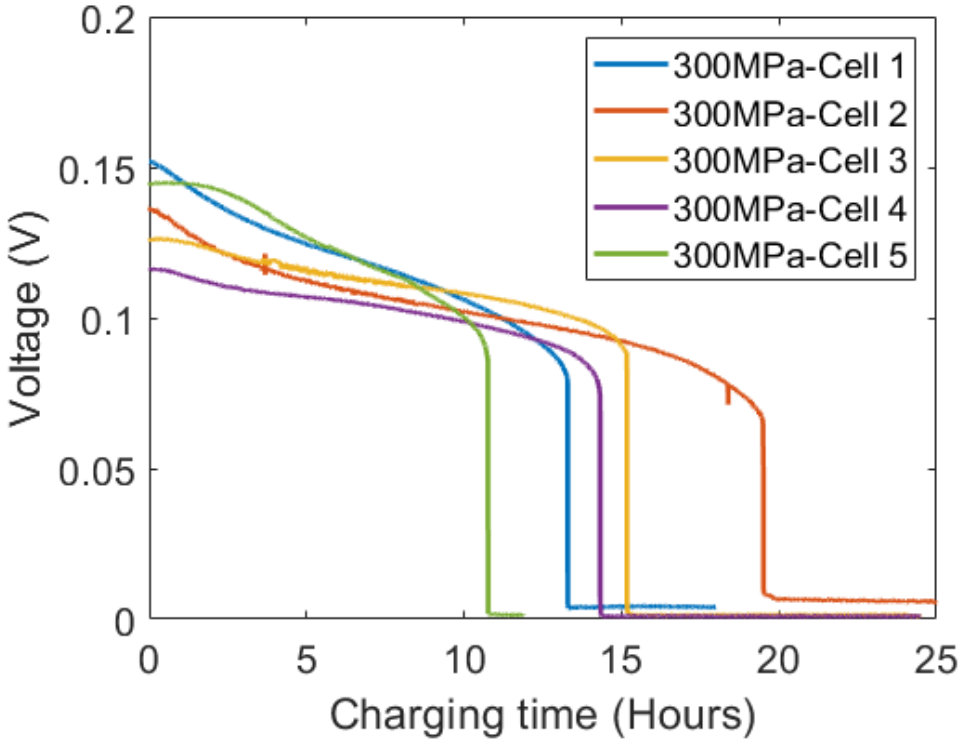

Figure SI-2.4-b. Electrochemical results of all cells pressed at pressure 300MPa.

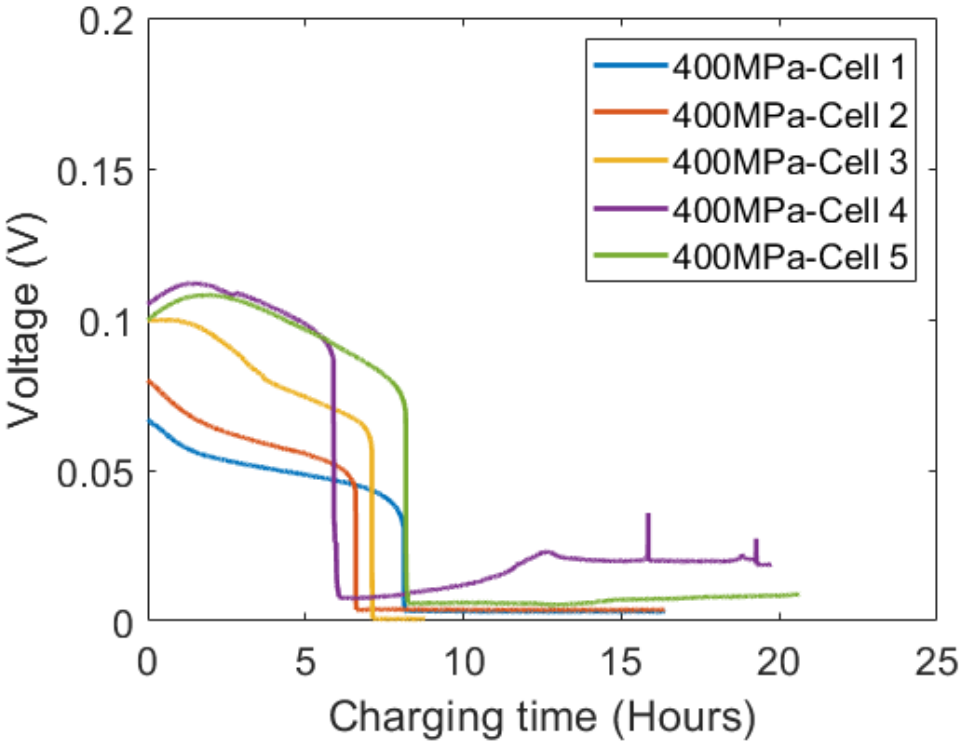

Figure SI-2.4-c. Electrochemical results of all cells pressed at pressure 400MPa.

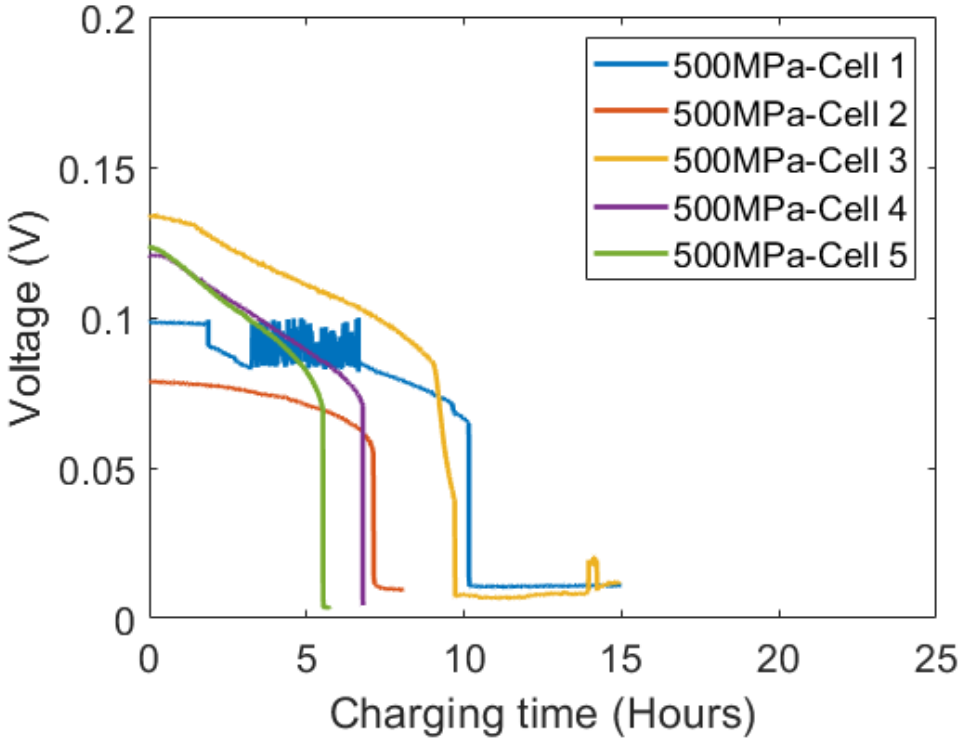

Figure SI-2.4-d. Electrochemical results of all cells pressed at pressure 500MPa.

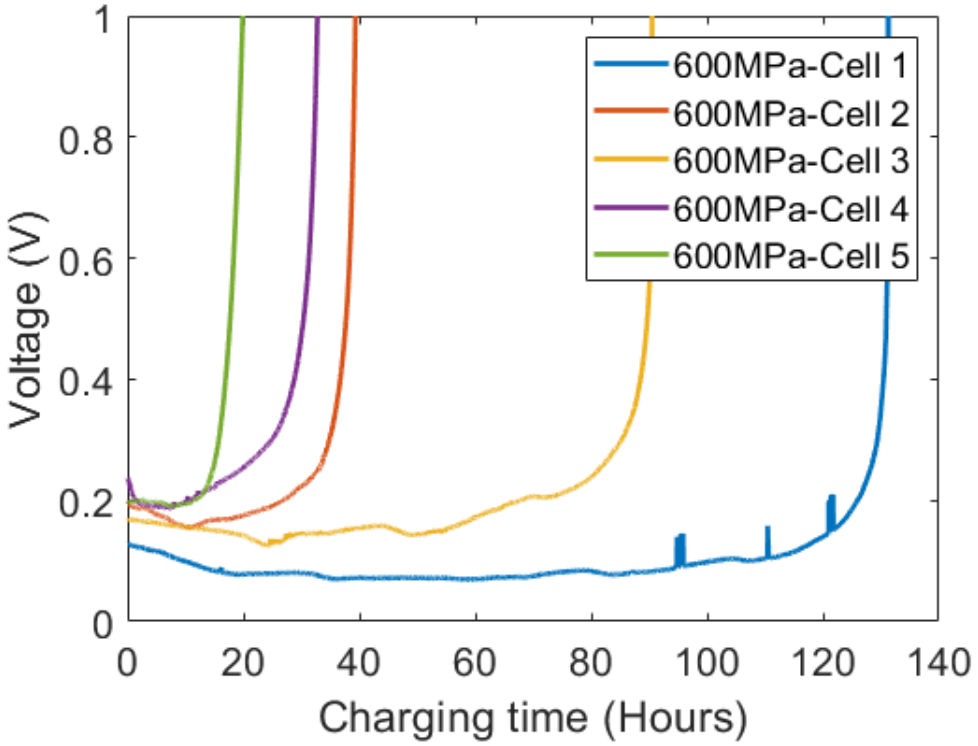

Figure SI-2.4-e. Electrochemical results of all cells pressed at pressure 600MPa.

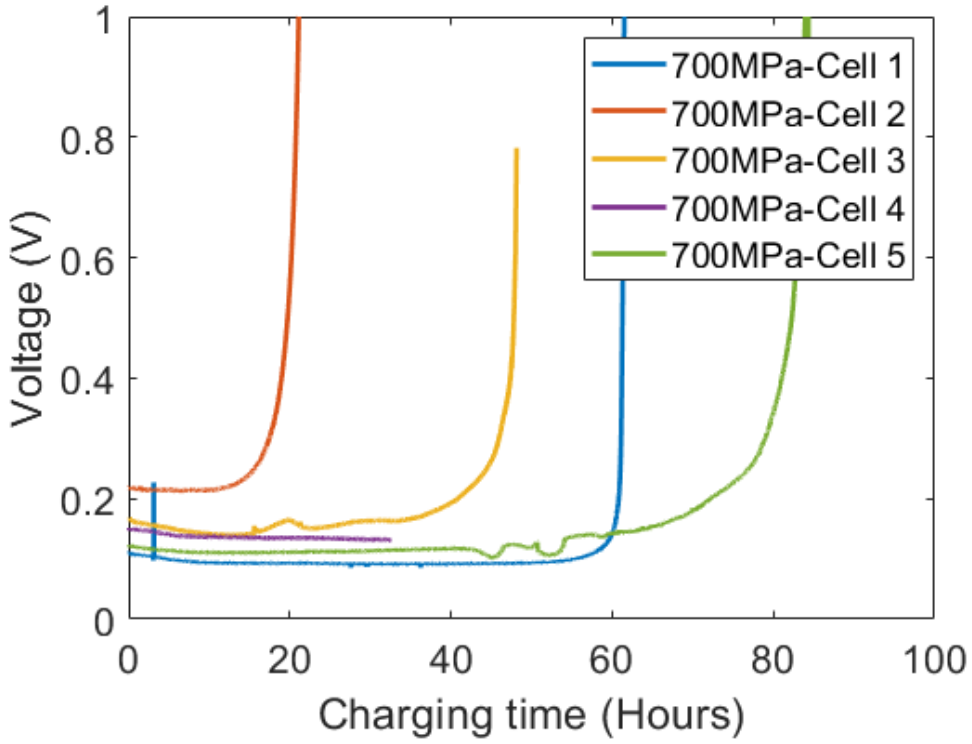

Figure SI-2.4-f. Electrochemical results of all cells pressed at pressure 700MPa.

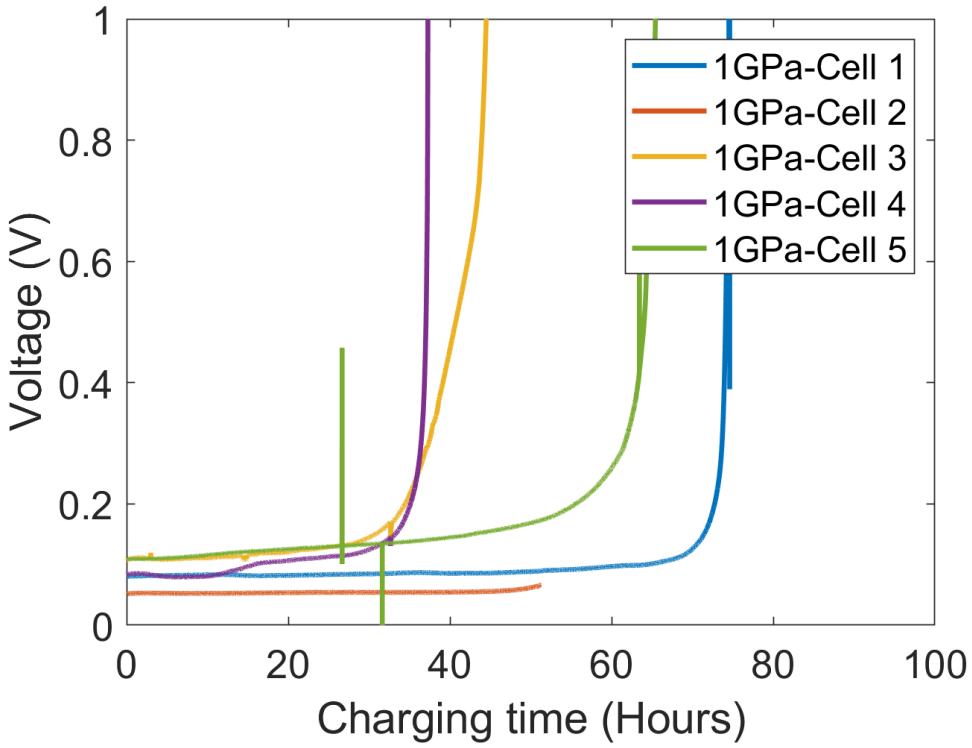

Figure SI-2.4-g. Electrochemical results of all cells pressed at pressure 1000MPa.

The clean surface at counter electrode showing the depletion: The cells which have high density, greater than 95%, are determined to be non-percolating, which means the LPS pellet has pores that are small and not connected. It is shown that, based on the lithium amount in the stripping side, the cells can survive more than 140 hours charging until depletion of the lithium. *Figure SI-2.5* shows two disassembled LPS pellets, one pressed at 700 MPa and the other at 1 GPa. For both cells both the lithium stripping side and plating side are presented, and lithium metal is fully depleted from the stripping side.

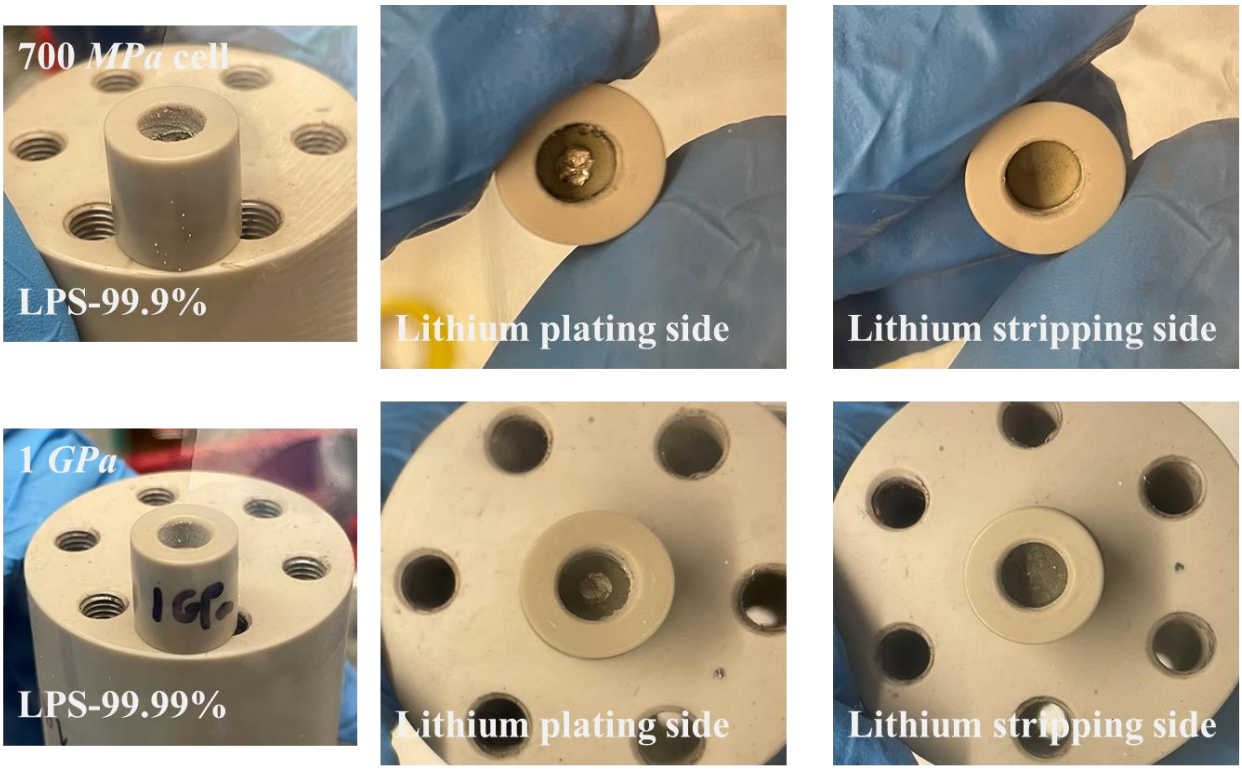

Figure SI-2. 5. The LPS surfaces at the plating side and at the stripping side of the 700MPa and 1GPa cells. The shiny metal at the plating surface is the 1/8-inch lithium metal.

High-resolution tomography reveals local microstructure in the bulk LPS pellet: LPS pellets of varying densities were cut in the normal direction using FIB and characterized using SEM under a tilt angle of 52°.The 3D pore microstructure at the bottom right (highlighted in yellow) was reconstructed from 100 cross-sectional slides along the milling direction. *Figure SI-2.6* describes the general procedure of the characterization. The LPS pellet was cut in the normal direction with FIB and characterized with SEM tilted by an angle θ (top-left image). The secondary electron image (top-right image) of the cross section (with size $50\mu m \times 50\mu m$) was captured and analyzed with the image processing software Dragonfly.[31] Multiple cross-sectional slides along the "milling direction" were obtained and analyzed following the same procedure, with final images shown in the bottom-left. The black area in the sequential images represent the pores and the gray area is the LPS material. The 3D structure is constructed from these images (bottom-right image). Pores are highlighted in yellow and LPS material in blue.

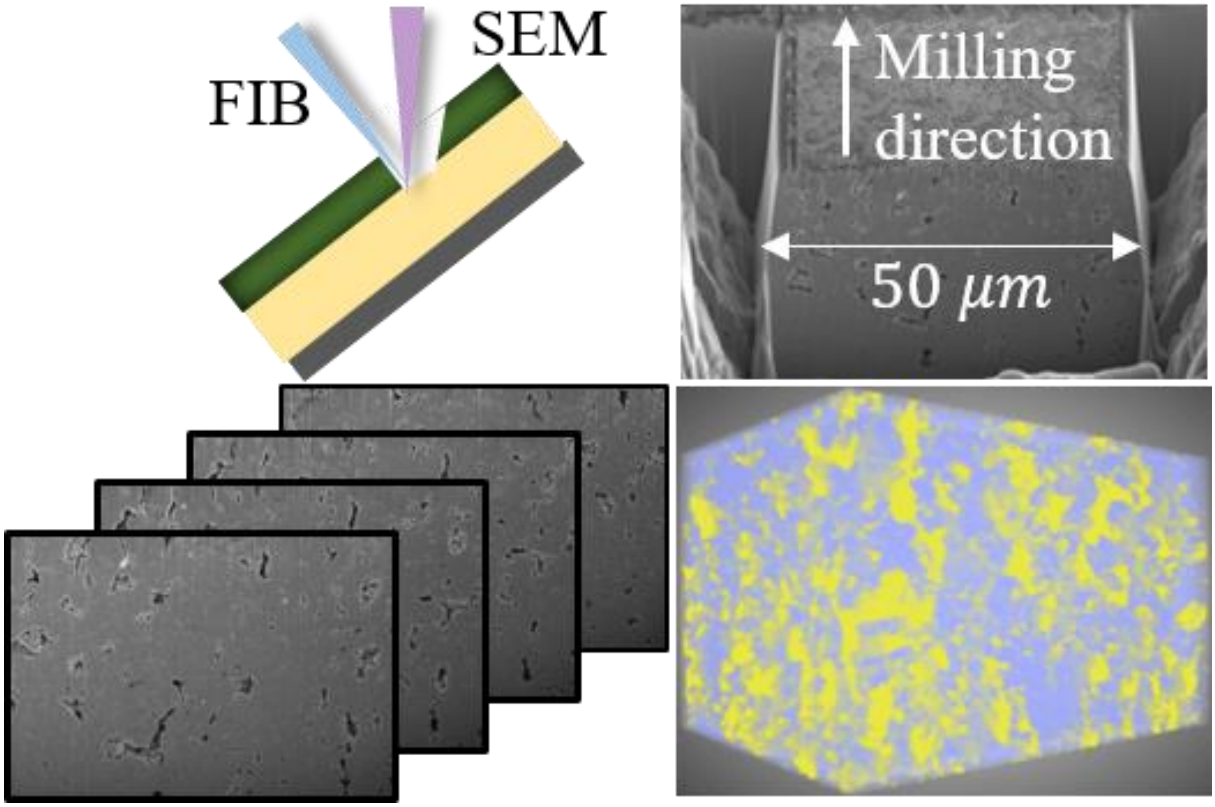

Figure SI-2. 6. General characterization procedure.

A house-developed MATLAB code is applied to the 3D tomography images for a more quantitative analysis. The pore size, porosity, and the connectivity (defined as the ratio between the largest pore volume over the total pore volume) of the three pellets in *Figure 2.3* are calculated statistically in *Figure SI-2.7*.

In summary, a range of pore size with $1\sim2\ \mu m$, $0.2\sim0.8\ \mu m$ and $< 0.1\ \mu m$ are observed in the LPS-81.3%, LPS-89.5%, and LPS-100%, respectively. The porosity of these three pellets is 8.43%, 2.28%, and 0.02%, respectively; and their connectivity values are 76.8%, 4.88%, and 3.34%, respectively.

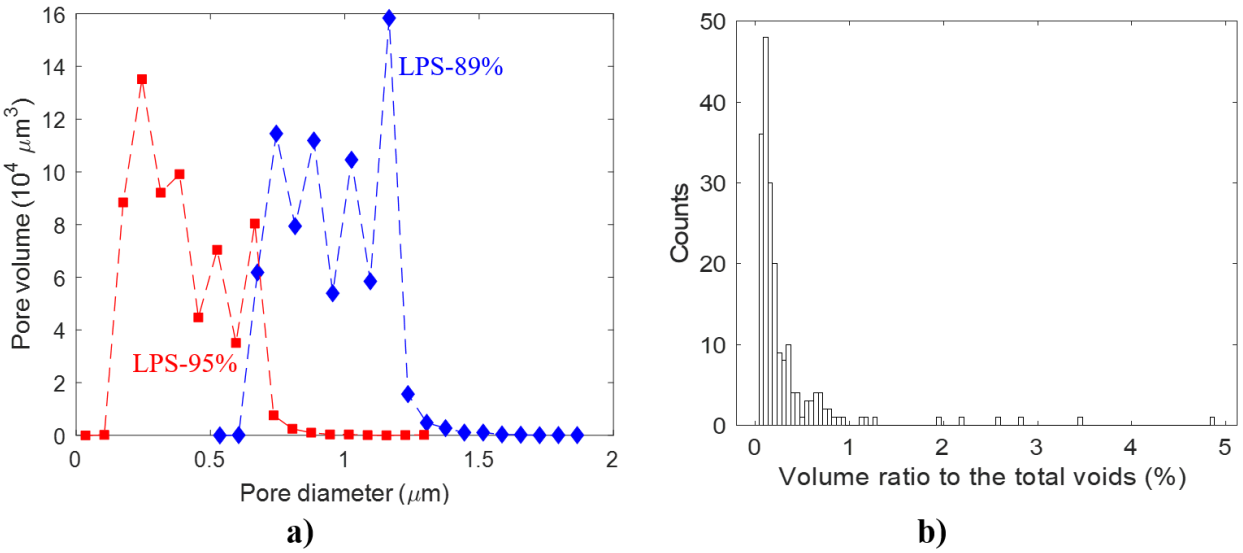

Figure SI-2. 7. The statistics of voids in pores with different densities.

SEM on the LPS pellet surface: SEM were used on LPS pellets with different densities to characterize surface morphology. *Figure SI-2.6* shows SEM images of the surface of LPS pellets at three different relative densities (LPS-89.2%, LPS-95.3%, and LPS-99.9%). It clearly shows that the pore size on the pellet surface decreases as the pellet becomes denser. Pores with diameter larger than 2 μm are frequently observed on the surface of LPS-89.2% pellet. These pores are not only interconnected on the surface, but also deep into the pellet (characterized by the dark area within the pores). In the LPS-95.3% pellet, both the size ($1\sim2\ \mu m$) and the number of connecting pores are reduced. Some pores are deep into the pellet while some only exist on the surface layer (characterized by the gray area within the pores). No connected pores (with diameter $< 1\ \mu m$) were found on the surface of the LPS-99.9% pellet, and all these pores are shallowly presented on the surface layer of the pellet. Notably, the images obtained can only represent the microstructure on the surface (or a thin surface layer) of the pellet. While the bulk microstructural properties inside the pellet may follow similar trend as that on the surface, more quantitative measurements are still needed.

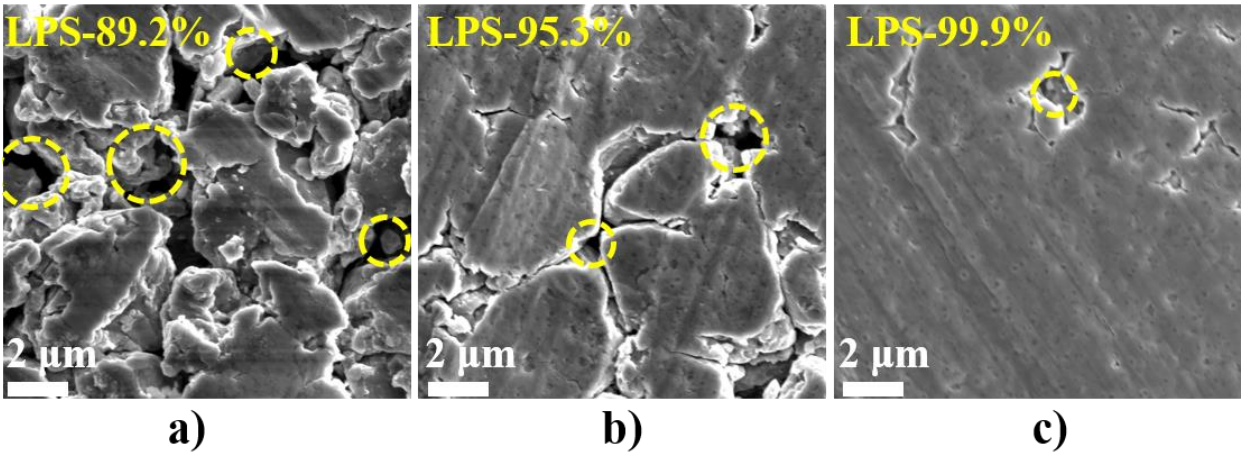

Figure SI-2. 8. The SEM results on the surface of LPS pellets at: a) 300MPa, b) 500MPa, and c) 700MPa.

The permeability tests and analysis: The pore connectivity was also quantified using the apparatus shown in *Figure SI-2.8*. The quantitative pellet permeability can be calculated using the modified Darcy's law by considering the Klinkenberg effect due to the compressible Ar[47,70]. In summary, Darcy's equation describes the linear relation between the flowrate (Q) and the pressure drop (ΔP) across the pellet thickness ($L = 2mm$): $\frac{Q}{A} = -\frac{k}{\mu L}\Delta P$, where A is the cross-sectional area of the top tube, k is the pellet permeability, and μ is the dynamic viscosity of the Ar gas within the LPS pellet ($\mu_{Ar} = 2.23 \times 10^{-5}\ Pa \cdot s$).[71] The permeability of the four pellets in *Figure 2.3-f* can therefore be extrapolated as $k_{82\%} = 1.50 \times 10^{-3}\mu m^2$, $k_{89\%} = 3.86 \times 10^{-4}\mu m^2$, $k_{95\%} = 1.82 \times 10^{-5}\mu m^2$, and $k_{99\%} \approx 0$.

The pellet permeability (k) can further be related to the microstructural parameters through the Carman–Kozeny relation: $k = \frac{d^2}{72}\frac{(1-\rho)^3}{\rho^2\tau^2}$, where d is the pore diameter, ρ is the pellet density, and τ is the tortuosity.[30,73] With the pore size ($0.2-1.2\ \mu m$) and permeability obtained in *Figure 2.3*, it is possible to evaluate the tortuosity of the LPS pellets at different densities: $\tau_{82\%} = 1.06$, $\tau_{89\%} = 1.34$, and $\tau_{95\%} = 1.94$. The percolating pore network becomes more tortuous as the LPS density increases, providing a longer growth path for the Li dendrite. However, the effect of this length increase (doubled from LPS-82% to LPS-95% based on the tortuosity value) on dendrite growth is much smaller than the effect of the pore size decrease, as will be discussed in the modeling section. Moreover, the Carman–Kozeny equation used here was derived with the assumption of cylindrical pores. The real pore network within the LPS pellet can be much more complicated with varying tortuosity.

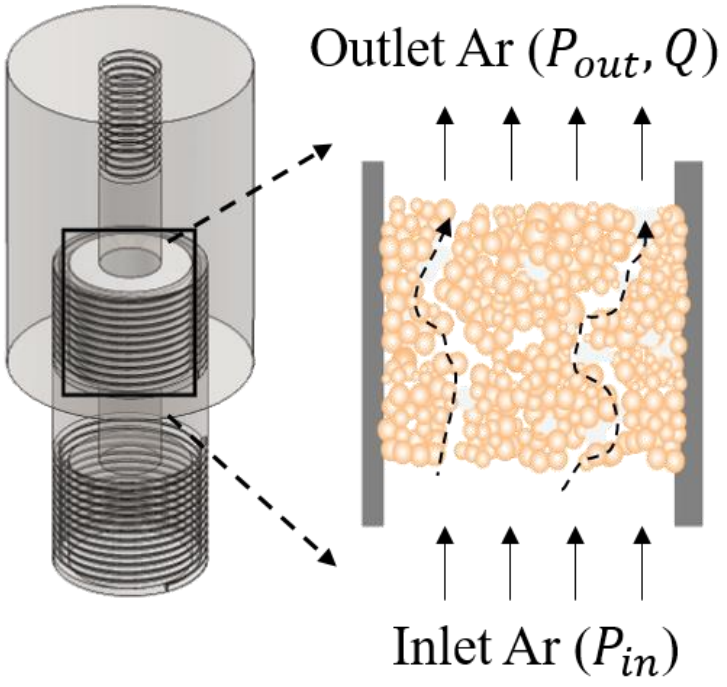

Figure SI-2. 9. Schematic of in-house-designed apparatus for permeability test.

The morphology of Li filament within the pore network: A postmortem LPS pellet in the percolating range (LPS-81.3%) is examined using the SEM to determine the lithium plating behavior inside the pellet. *Figure SI-2.10* shows the existence of two plating mechanisms. At first lithium is plated in the pores as depicted below, then lithium plates within the particle boundaries.

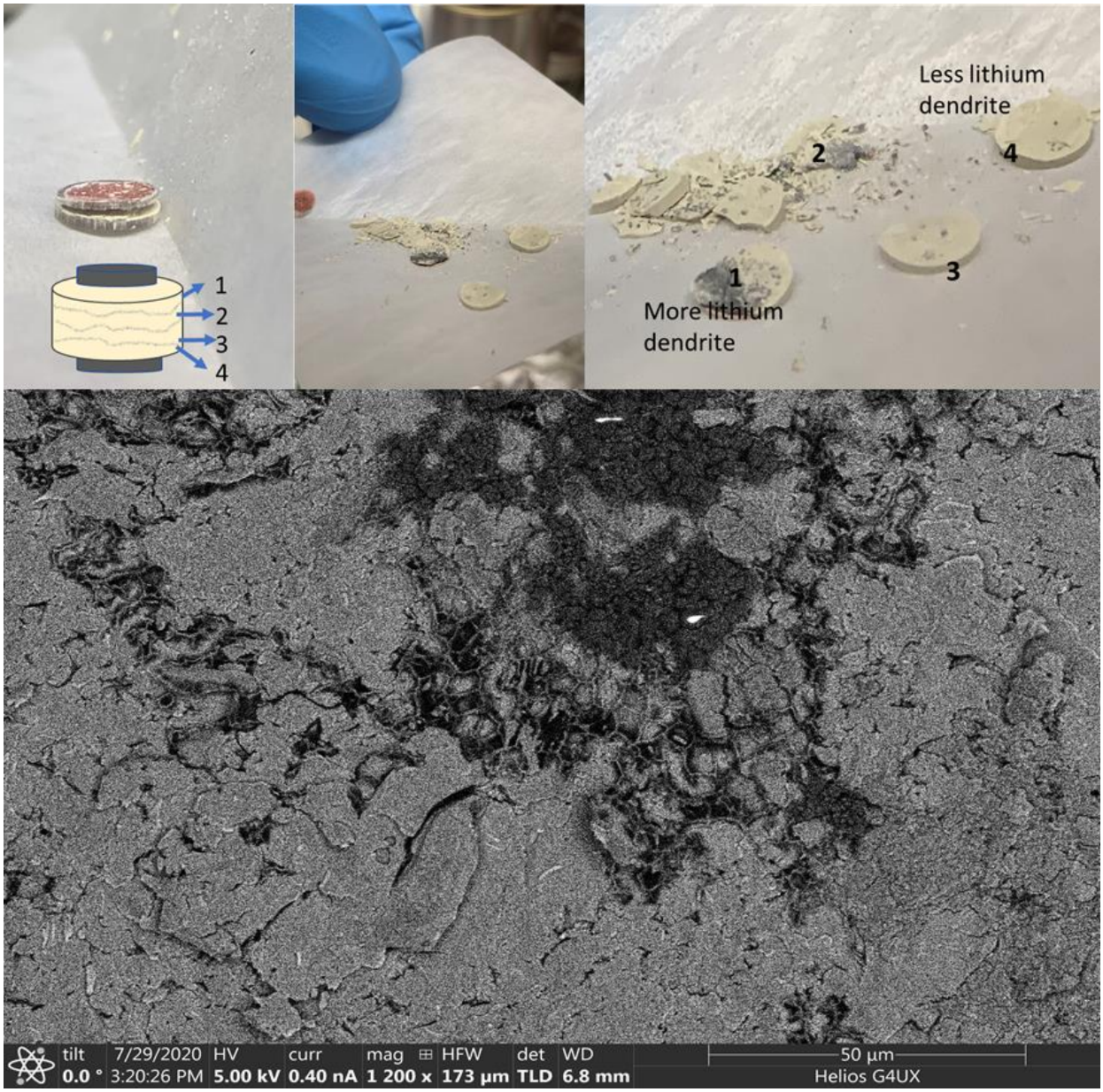

Figure SI-2. 10. The SEM results of Li filament.

The distribution of overpotential and ionic current within SE: The spatial distributions of the overpotential and the ionic current (Li+ flux) evolve in time as the dendrites propagate from the anode/SE interface into the SE. For example, the following figure shows the overpotential distribution (*Figure S-2.11-a*) and the ionic current (*Figure S-2.11-b*) when the dendrites reach a length of 10um from the Li-metal anode.

Figure S-2.11-a shows a dendrite propagating into the SE from the top lithium metal electride. The overpotential is zero at the interface between the SE and Li metal anode, and at the interface between SE and Li dendrites. This value increases to 2.6 mV at a depth of 20um inside the SE. *Figure S-2.11-b* shows the ionic current within the SE with the background color represents the overpotential. It shows that Li-ions migrate upward and deposit both on the interface at the Li metal anode and the interface at the Li dendrites.

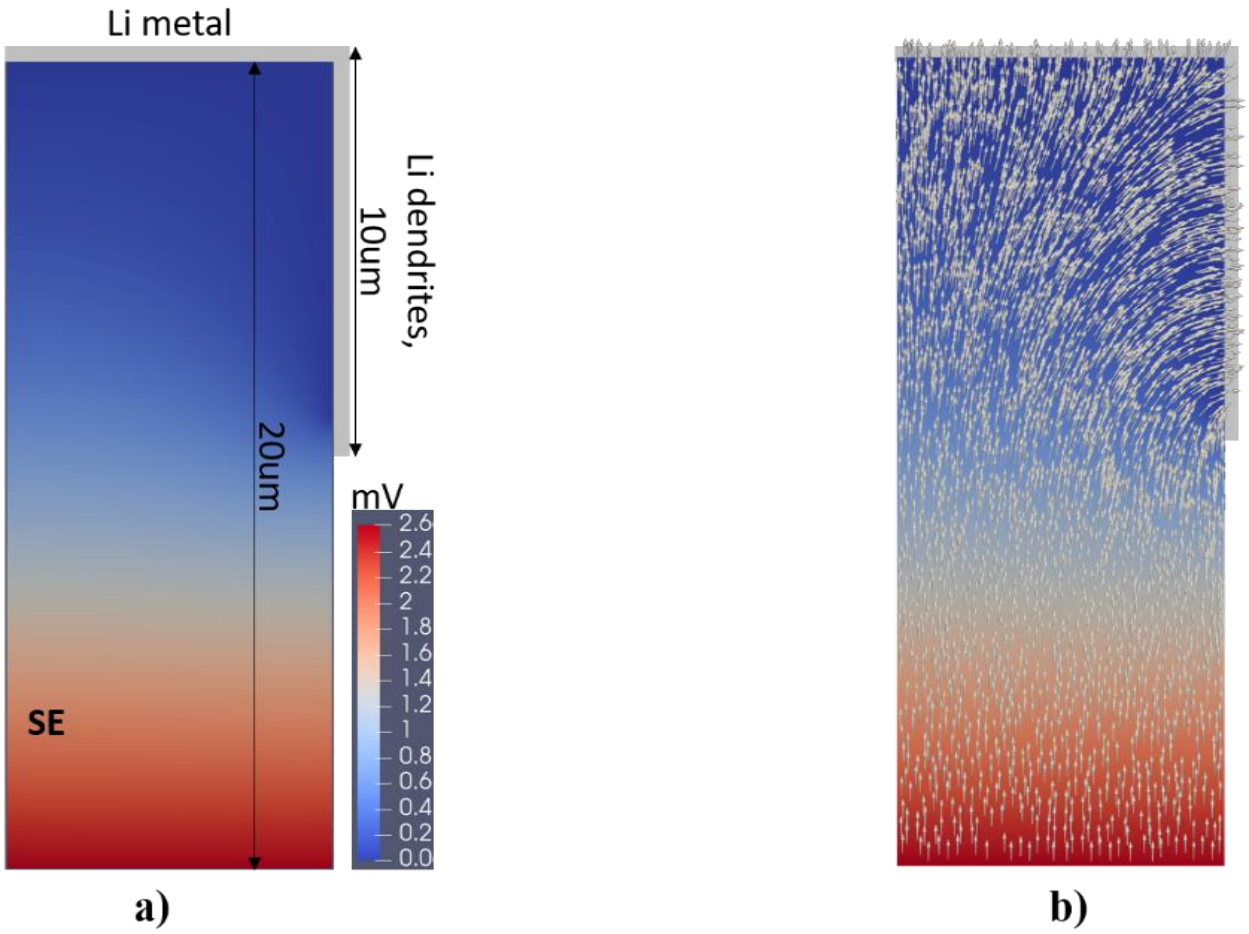

Figure SI-2. 11. a) illustrates the overpotential distribution within the SE with unit mV, where the Li metal anode is located on the top and 10 μm of Li dendrite already goes into the SE on the right top surface of the SE. Figure b) plots the corresponding ionic current in the SE.

The effect of electronic conductivity: It has been reported that the addition of Li_3N and LiF buffer layer (BL) between the Li metal and SE can increase the cyclability in argyrodite cells because the BL is believed to greatly reduce the electronic conductivity and neutralize the chemical reaction. This finding prompted the evaluation of our percolation hypothesis by mimicking the results presented in the work of Ji et al.[64]. Two cells were cycled at the same densities using the same cycling conditions of 0.2 mA/cm^2 for 1-h charge and discharge. Indeed, as shown in *Figure SI-2.12*, the BL increased the cyclability of the cells even in the pore-percolating region. This is because of the stable interface between the Li_3N–LiF buffer layer and Li metal. The cycling performance is related to the stable plating of Li metal, which does not react with the buffer layer, contrary to the known continuous reaction of Li metal and LPS. However, as shown in *Figure SI-2.12-b*, when the cell is tested using the long-charging criteria, the cell with the BL behaves similar to the cells without the BL. Li metal still plates inside the percolating pores, and the cell is shorted after 19 h. Although isolating chemical reactions and reducing electronic conductivity helps to increase cyclability, it does not prevent the deposition of lithium metal in percolated pores.

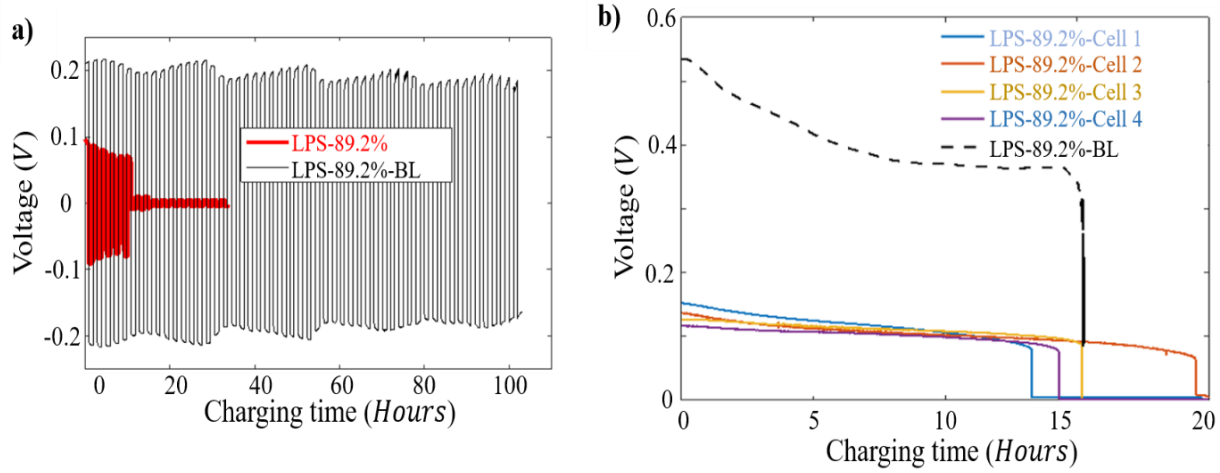

Figure SI-2. 12. The controlling experiment by adding a buffer layer

The short circuit of cell with dense LPS pellet under increasing current density: *Figure SI-2.13* shows the cell in the non-percolating range short as current density is increased. The SE fracture should not be caused by mechanical shearing of isolated pores; however, the high hydrostatic pressure developed after Li metal fills isolated pores.

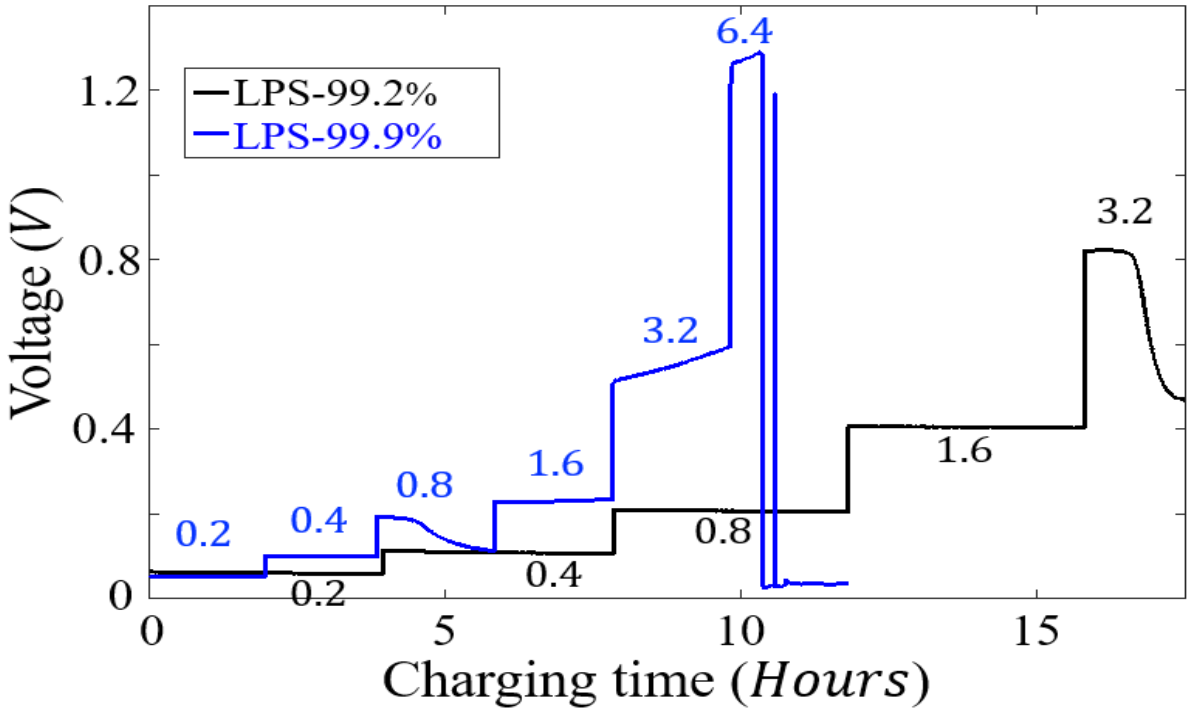

Figure SI-2. 13. Increased current density on cells in the non-percolating regime.

2.7 Acknowledgements

This work was supported by the Samsung Advanced Institute of Technology and the Office of Energy Efficiency and Renewable Energy of the U.S. Department of Energy under Contract No. 1384-1778. The SEM analysis was performed at the Molecular Foundry, Lawrence Berkeley National Laboratory, supported by the Office of Science, Office of Basic Energy Sciences, of the U.S. Department of Energy under Contract No. DE-AC02-05CH11231. This research used the Lawrencium computational cluster resource provided by the IT Division at Lawrence Berkeley National Laboratory (supported by the Director, Office of Science, Office of Basic Energy Sciences, of the U.S. Department of Energy under Contract No. DE-AC02-05CH11231) and the Savio computational cluster resource provided by the Berkeley Research Computing program at the University of California, Berkeley (supported by the UC Berkeley Chancellor, Vice Chancellor for Research, and Chief Information Officer). The authors also gratefully acknowledge Dr. Srinath Chakravarthy for all the helpful discussions and Dr. Rui Liu for providing guidance for the permeability tests for the LPS pellets.

Chapter 3: The Microscopic Mechanism of Lithiation and Delithiation in the Ag/C Buffer Layer for Anode-free Solid-state Batteries

3.1 Foreword

The work presented in this chapter is based, often verbatim, on the following publication:
Xie, F.***; Diallo, M.S***.; Kim, H.; Tu, Q.H.; Ceder, G., "Microscopic Mechanism of Lithiation and Delithiation in the Ag/C Buffer Layer for Anode-Free Solid-state Batteries." *Advanced Energy Materials* **14**, 1-18 (2024).

3.2 Abstract

Lithium metal solid-state batteries (LMSSBs) have garnered significant interest due to their enhanced energy density and operational safety. Recent research has demonstrated their high energy density and exceptional cycling performance at high current densities in an anode-free architecture, featuring a thin Ag/C composite buffer layer (BL) between the current collector (CC) and the solid electrolyte (SE). In this study, we present a comprehensive explanation of the working principles of the Ag/C BL by using first-principles atomistic and continuum modeling techniques. Our first-principles study of the thermodynamics of Ag–Li during lithiation reveals that Ag effectively acts as a homogeneous solid-solution beyond $AgLi_{2.32}$ and maintains a positive potential of ~2mV even at $AgLi_{25}$. We reveal a combination of multiple factors underlying the predominant Li deposition at the CC/BL interface and Ag migration toward the CC. These factors include: (1) a lower interfacial resistance at the BL/CC interface than at the BL/SE interface, which causes a majority of Li redox current to occur on the BL/CC side; (2) substantial volume expansion of Ag–Li alloy during lithiation, combined with stronger adhesion between the SE and BL than between the CC and BL, resulting in the separation of the BL from the CC and the extrusion of Ag–Li alloy towards the CC side. During delithiation, Ag re-precipitates as nanoparticles uniformly distributed on the CC, serving as attraction sites to Li currents. Our continuum modeling elucidates how the positive lithiation potential of Ag promotes a homogeneous distribution of Li currents during subsequent electrochemical cycles. We rationalize the reduced effectiveness of several other metals by demonstrating the development of their relatively large overpotential and premature lithiation termination. The limited volume expansions of these metals also hinder their elastoplastic movement towards the CC, making re-precipitation less feasible. This study provides insights into the BL design, including metal choice and the optimization of material and microstructural properties, such as the Li-ion conductivity and interfacial resistance.

3.3Introduction

Lithium-metal solid-state batteries (LMSSBs) offer a promising avenue for rechargeable battery technology due to their potential of enhanced safety and energy density[5,84–86]. The use of inorganic ceramic solid electrolytes (SEs) offers non-flammability and high mechanical strength, enabling the incorporation of energy-dense Li-metal anodes, which can significantly increase the energy density of rechargeable Li-ion batteries. However, several limiting fac- tors, such as the high costs associated with free-standing Li-metal-foil[21], interfacial contact loss[87], and unwanted (electro)chemical reactions between the SE and Li metal[65], hinder the practical applications of LMSSBs. Most critically, Li-metal dendrite formation, which results from non-uniform Li-metal deposition under localized currents[88–90], can penetrate SEs such as oxides (including $Li_7La_3Zr_2O_{12}$, LLZO) and sulfides (including Li_3PS_4, LPS; Li_6PS_5Cl, LPSCl)[69,91–95], leading to battery shorting. Non-uniform Li deposition stems from imperfect solid–solid interfaces and can be exacerbated by detrimental interphase growth[96] and void formation[97] during cycling.

Significant effort has been devoted to suppressing Li dendrite growth in solid-state batteries. Controlling the stack pressure[97,98] and temperature[99] of the solid-state cells can be beneficial in homogenizing Li deposition. Incorporating metal interlayers, such as gold (Au) and silver (Ag), also results in improvements[65]. Recently, Lee et al.[33] developed an Ag/C composite buffer layer (BL) and demonstrated its excellent properties in an anode-free LMSSB. In their study, $LiNi_{0.90}Co_{0.05}Mn_{0.05}O_2$ (NCM) coated with Li_2O-ZrO_2 was used as the cathode material and LPSCl argyrodite was used as the SE. Ag and amorphous carbon (Ag/C) were mixed into a composite film at a thickness of 5-10 µm, and the film was employed as a BL separating the current collector(CC) and SE with no Li metal used at the anode side. This ”anode-less” full cell delivered an energy density of 941 Wh/L, exhibited long cycling life (89% capacity retention after 1000 cycles) and high coulombic efficiency (average > 99.8%). The excellent performance was attributed to the uniform Li deposition resulting from the use of the Ag/C BL. Several key observations should be noticed from the work of Lee et al. and follow-up work. Li-metal plating occurred at the BL-CC interface during the lithium transfer to the anode. In addition, Ag was found to move to the CC and dissolved into Li metal upon full lithiation at the anode. Upon discharge of the cell, the Li metal was stripped from the anode CC and most Ag particles did not return to the BL but remained near the CC. Through comparison with other metals (Sn, Zn, Al, and Ni), Suzuki et al.[34] demonstrated Ag to be the best-performing metal in a metal/C BL. Later, Kim et al.[35] proved that the Ag/C BL can also assist with homogeneous Li-metal deposition on the CC when using LLZO as the SE, with an additional layer of Ag thin film used to enhance the adhesion between the Ag/C BL and LLZO SE.

Building on the pioneering work of Lee et al. [33] and Kim et al. [35], researchers have explored the thermodynamic and kinetic factors influencing uniform Li plating at the BL/CC interface. In a recent study, Park et al.[100] demonstrated that the stronger adhesion between the BL and SE, compared to that between the BL and CC, promotes Li deposition at the BL/CC interface rather than at the BL/SE interface. Park et al. also suggested that Li migrates through the BL via Coble

creep, with factors such as smaller pores and particles, higher temperatures, and lithiophilic surface modifications (e.g. , Ag decoration) facilitating Li movement. In a subsequent study, Kim et al.[101] found that the preferred plating location of Li metal is determined by the lithium-transport behavior in the BL, as evidenced by a comparative study where amorphous carbon was replaced with less Li-conductive graphite. The findings of Kim et al. align well with the observations of Suzuki et al. , who noticed that Li plates between the BL and the SE when graphite is used in the BL. In contrast, when carbon black is employed in the BL, Li plating shifts to the CC side.[34] Spencer-Jolly et al.[36] conducted research on an Ag-graphite composite and concluded that Ag in the BL leads to relatively homogeneous Li-metal deposition between the BL and CC. However, they also found that at high current density the Ag-modified BL is not more effective in suppressing Li dendrite formation than pure graphite without Ag.

Several fundamental questions regarding the microscopic mechanism active in the Ag/C BL remain unanswered, including (1) how Ag helps homogenize current and prevent Li dendrite formation, (2) why Ag migrates to the CC side, (3) why Li only appears at the SE/CC interface, and (4) why other metals are not as effective in enhancing the cycling performance in the BL as compared to Ag. In this paper we take a multi length-scale and multi physics approach, combining ab-initio thermodynamics of Ag–Li with continuum transport and mechanics, to understand the role Ag plays in assisting the Li plating.

Understanding the phase stability in the Ag–Li system is critical to correctly predict the behavior of Ag during lithiation. However, the commonly used Ag–Li phase diagram is based on very limited and often outdated experimental and computational data. Pastorello[102,103] first determined the Ag–Li phase diagram in the 1930s, reporting two intermetallic com- pounds: AgLi and $AgLi_3$. In the 1950s, a more comprehensive report by Freeth and Raynor[104] (*Figure 3.1-a*) disputed the existence of $AgLi_3$ and instead proposed 6 phases at room temperature (*Figure 3.1-b*): the FCC Ag solid-solution phase ($x_{Li} = 0 \sim 0.46$), the β-AgLi phase with a CsCl-like structure ($x_{Li} = 0.50 \sim 0.56$), the $\gamma 3/\gamma 2/\gamma 1$ phases with γ-brass type structures ($x_{Li} = 0.64 \sim 0.93$), and the BCC Li solid-solution ($x_{Li} = 0.99 \sim 1.00$). Based on the detection of two-phase coexistence at $x_{Li} \sim 0.75, 0.84$ in X-ray powder diffraction (XRD) and the presence of thermal arrests, Freeth and Raynor identified three γ phases which they claimed to have γ-brass-like structures, informed by the observations of Perlitz[105]. However, without any original XRD pattern or thermal measurement data provided in Freeth and Raynor's paper, the existence and structures of these γ phases, especially the γ_2 and γ_1 phases, remain unclear. More precise XRD measurements by Arnberg and Westman[106] revealed that the γ_3 structure aligns more closely with the Cu_5Zn_8-prototype than with the Al_4Cu_9 structure type, a claim that more recent measurements[107] have confirmed. Arnberg and Westman also attempted to synthesize γ_2 and γ_1, but failed as Li-rich samples easily react with air. The Ag–Li phase diagram, especially on the Li-rich side, has not been significantly updated since this early work. Pelton's work in the 1980s[108] mostly drew from the results of Freeth and Raynor[104], with some additional investigations into the liquidus line. Recently, Braga et al.[109] claimed the γ_1 phase to be nonexistent by comparing the first-principles free-energy calculation results of the γ and BCC phases. Braga et al. also suggested the γ_2 phase to be an

$Ag_{15}Li_{49}$ BCC structure instead of the Pb_3Li_{10}-like structure hypothesized by Freeth and Raynor. However, the similarity in the XRD patterns of $Ag_{15}Li_{49}$ and Ag_3Li_{10} along with potential interference from impurities make the second claim difficult to verify experimentally. Furthermore, the calculations of Braga et al.[109] in the BCC and FCC structures used only a single special quasi-random structure (SQS) at each composition[110] to represent the energy of the solid solution without any configurational entropy to evaluate its ability to destabilize ordered compounds at non-zero temperature.

In this article, we employ first-principles thermodynamic calculations to determine the free energy of each phase in the Ag–Li alloy system, incorporating the electronic energy, configurational entropy, and phonon free energy. The phase stability and lithiation voltage into Ag are analyzed using computed free energy. Continuum modeling is applied to study the Li transport in an Ag–C buffer layer (BL), the current density distribution in the BL and at interfaces, and the mechanical behavior during lithiation and delithiation, as well as to analyze the migration of Ag particles. By integrating results from various models, we provide a comprehensive explanation of the microscopic mechanism during the cycling of an Ag/C BL and suggest optimal BL metal choices and processing conditions.

3.4Results and discussion

3.4.1 Approach

We systematically investigated the phase stability in the Ag–Li system using first- principles calculations to determine low-energy Ag–Li configurations on multiple possible lattices. We iteratively searched for ground-state configurations[111], covering the FCC Ag solid-solution phase and BCC-derived phases (β-AgLi and BCC Li solid-solution) at $x_{Li} = 0 \sim 1$ (*Figure 3.1-b*)

As shown in *Figure 3.1-c*, the γ-brass crystal structure resembles the BCC crystal structure. The γ-brass structure can be obtained from a BCC 3*3*3 supercell by removing the corner and center atoms and relaxing the remaining atoms under the symmetry of the $I43m$ space group. Atoms in the γ-brass structure can be grouped into 4 symmetrically distinct sub-lattices[112]:

1. Type A (orange): 8 sites, forming the innermost tetrahedral cluster around vacancies.
2. Type B (purple): 8 sites, forming a larger tetrahedral cluster outside the cluster of A;
3. Type C (blue): 12 sites, forming an octahedral cluster outside the cluster of A and B;
4. Type D (green): 24 sites, forming the largest cluster encapsulating the clusters of A, B and C.

Different γ-type structures differ by the distribution of the components over these sites. In other studies[108,113], types A, B, C, and D are also denoted as IT, OT, OH, and CO, respectively. Each sub-lattice can be further divided based on symmetry breaking of the original positions in the BCC lattice: type 1 (squares) for sites originally on the cubic centers and type 2 (circles) for sites originally on the cubic corners. In Table-3.1, structural data from the Materials Project[114] and the ICSD database[115] are used to classify all experimentally observed γ-brass structures into six distinct prototype classes with different sub-lattice occupancies. We used these as a starting point

to evaluate possible γ-brass type phases in the Ag–Li system. Under the Cu_5Zn_8 prototype, we enumerated Ag–Li configurations from x_{Li} = 8/13 to x_{Li} = 1, assuming that Ag can only be located at B and C sites with further DFT computations performed on all five other γ-brass prototypes (as shown in Table-3.1)to validate the assumption on Ag occupancy limitation.

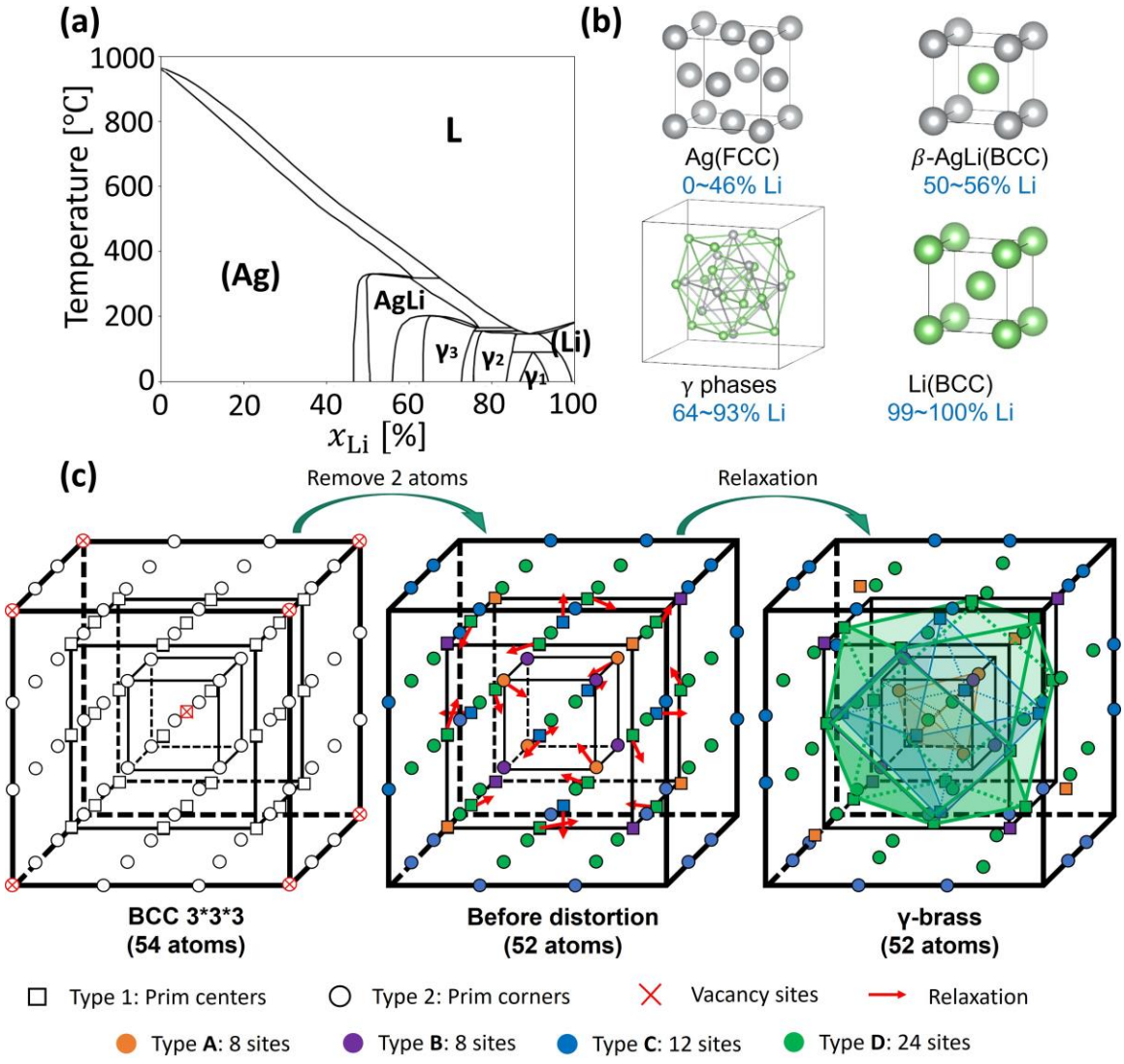

Figure 3. 1. (a) Experimental temperature–composition phase diagram of the Ag–Li system, redrawn from the data of Freeth and Raynor[104]. (b) Crystal structure of phases in the Ag–Li system at room temperature, including (Ag), β-AgLi, γ-brass phases, and (Li). (c)The γ-brass structure and its relationship to the BCC structure. The left subplot shows a 3*3*3 supercell containing 54 atoms, scaled from the conventional BCC cubic cell. Atoms located at the body centers of the conventional cube are marked as type 1 (squares), whereas atoms located at the body corners are marked as type 2 (circles). The middle subplot shows the supercell with 52 atoms remaining after removing 2 atoms at the center and corners of the supercell (red cross). The remaining sites are grouped into 4 sub-lattices: type A (orange), type B (purple), type C (blue), and type D (green). For visibility, only the relaxing direction of the A_2, B_2, C_1, and D_1 atoms are marked in red arrows. The relaxing direction of the other atoms can be found by applying symmetry in the I43m space.

Table-3. 1. Experimentally observed prototypes of γ-brass structures, extracted from the Materials Project and the ICSD database.

Prototype	Ag/Li occupancy	References	Notes
Cu_5Zn_8	A, D: Li; B, C: Ag/Li mixed	[116]	Experimentally confirmed γ_3;
Al_4Cu_9	A_2, D_1 (or A_1, D_2): Ag; Other: Li	[117]	Proposed by F&R as γ_3.
Pb_3Li_{10}	D_2 (or D_1): Ag; Other: Li	[118]	Proposed by F&R as γ_2.
$RuAl_{12}$	A_1 (or A_2): Ag; Other: Li	[119]	Proposed by F&R as γ_1.
Fe_4Zn_9	A: Ag; C: Ag/Li=2:1; B, D: Li	[120]	DFT assumed all C sites to be occupied by Ag, giving x_{Li} = 8/13.
In_5Ti_8	A_1, B_1, D_1 (orA_2,B_2,D_2): Ag; Other: Li	[121]	

To capture the free energy of Ag–Li phases, we fit cluster-expansion (CE) models for BCC, FCC, and γ (exclusively Cu_5Zn_8 prototype) lattices. A cluster expansion[122,123] is a well-established approach in ab-initio alloy theory to parameterize the configurational energy dependence so that it can be sampled with Monte-Carlo (MC) techniques[124]. We performed MC simulation at varied temperatures (T) and Li contents (x_{Li}) and integrated the sampled energy over temperatures to obtain the configurational free energy. The configurational free energy values are interpolated over compositions using a B-Spline fit to represent the free energy as a continuous function of composition. We accounted for lattice vibrations by adding phonon free energy into the CE-MC result. Details about these methods can be found in the Methodology section.

The transport behavior of Ag and Li in the BL was investigated with electro-chemo- mechanical modeling. We described the conduction of Li-ions and electrons in the BL by applying mixed ionic-electron conducting theory[125], modeled the redox reaction of Li at the SE/BL and CC/BL interfaces with the Butler–Volmer relation [126], simulated the diffusion of Li and Ag in the alloy using the Cahn–Hilliard equation[127], and investigated the plastic flow of Li in BL with elastoplastic mechanics[128]. Key parameters that govern Li deposition at the BL/CC interface and the Ag migration towards CC were systematically examined. These factors include the area-specific charge transfer resistance (ASR), the adhesive strength at different interfaces, the lithiation potential in the Ag particles, and the pressure developed within the BL. We also investigated the factors that affect the Li-current distribution on the CC surface, aiming to understand the role of Ag in homogenizing Li deposition and provide strategies for optimizing anode-free battery design. More detailed explanations about these simulations are provided in the

Methodology section. All the relevant partial differential equations were solved with self-developed programs based on the Finite Element Method[129]. Parameters used in these simulations can be found in the Supplementary Information.

3.4.2 Results

3.4.2.a *Phase stability in the Ag–Li System*

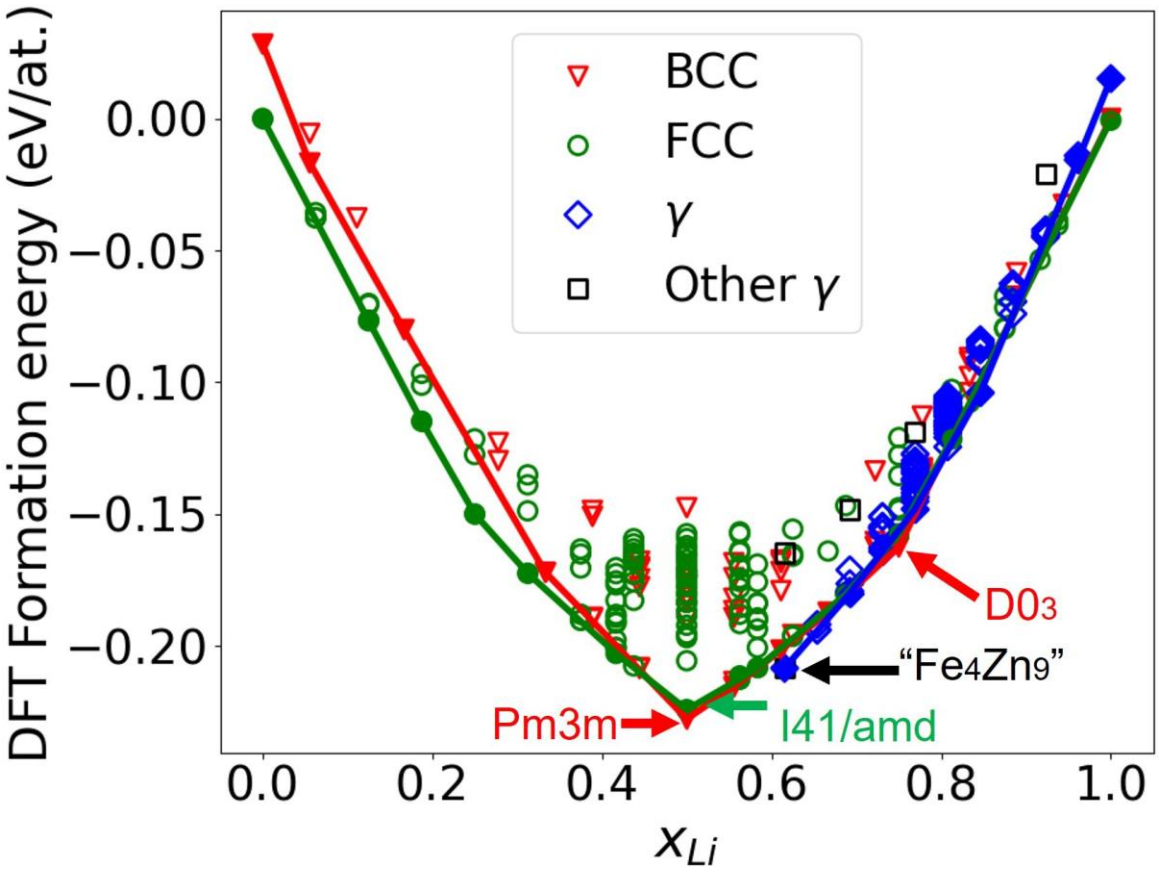

Figure 3. 2. DFT computed zero-K formation energy of Ag–Li structures in BCC (red triangles), FCC (green circles), Cu_5Zn_8 γ-brass (blue diamonds), and other γ prototypes (black squares). Convex hulls are shown for all compounds within a structural type, with structures on the convex hulls marked by solid markers. The formation energy of the FCC I41/amd structure, BCC Pm3m structure at x_{Li} = 0.5, and BCC $D0_3$ structure at x_{Li} = 0.75 are marked with arrows.

Figure 3.2 presents the zero-K formation energy of each structure enumerated within BCC, FCC, Cu_5Zn_8-γ lattice models, along with the other five γ prototypes shown in Table-3.1. The energy of FCC Ag and BCC Li were used as references. As shown in *Figure 3.2*, the ground-state configurations on BCC and FCC lattices at x_{Li}=0.5 were found to be a Pm3m CsCl-type cubic structure (indicated by a red arrow) and an $I4_1/amd$ tetragonal structure (indicated by a green arrow), respectively. The energy of the Pm3m cubic structure is 5.2 meV/atom below the $I4_1/amd$ structure. The ground state at x_{Li} = 0.75 appears to be a BCC $AgLi_3$ structure (*Figure 3.2)* with $D0_3$ ordering (*i.e.* , BiF_3 ordering). All the other γ prototypes (hollow black squares) exhibit

significant instability (> 50meV/atom) relative to structures belonging to the Cu_5Zn_8 prototype, with the exception of the Fe_4Zn_9-like structure which relaxes to the Cu_5Zn_8-like structure and therefore yields the same energy(hollow black square overlapping with solid blue diamond at x_{Li}=8/13; refer to the Supplementary Information for structural relaxation details). This high energy of other γ-prototype structures may arise from repulsive short-ranged Ag–Ag interactions occurring between A and D sites, validating our assumption that Ag should only exist on B and C sites. Thus, we should exclude other γ-brass prototypes with Ag on A and D sites, including those proposed by Freeth and Raynor[104].

Based on the DFT ground-state analysis we proceed with the computation of free energy for the BCC, FCC, and γ(Cu_5Zn_8-prototype only) lattice structures. *Figure 3.3* shows the formation free energy as a function of x_{Li} (ΔF (x)) at T = 200 K and 300 K. At T = 200 K (*Figure 3.3-a*), we identify four stable phases: the FCC Ag phase from xLi = 0 to 0.512, the β-AgLi phase with a CsCl-like crystal structure from x_{Li} = 0.524 to 0.548, a γ-brass phase with x_{Li} = 8/13 stoichiometry and a BCC solid solution for x_{Li} = 0.693 ~ 1. Only one γ phase emerges in *Figure 3.3-a*, corresponding to the γ_3 phase proposed by Freeth and Raynor[104]. Upon increasing the temperature to T = 300 K (*Figure 3.3-c*), BCC is stabilized over γ_3 due to both configurational and vibrational entropy effects (refer to Supplementary information). At this temperature, only the FCC Ag phase and the BCC solid solution persists. The transformation of γ_3 into BCC at high temperatures agrees well with the qualitative trends seen in the experimental phase diagram (*Figure 3.1-a*) though it is clear that our computations predict too low a temperature at which γ3 transforms into BCC. It should be noted that the transformation temperature is highly sensitive to small errors in the energy or entropy differences between the structures. In *Figure 3.3-b* and *3.3-d*, the D03-$AgLi_3$ structure is determined to be the equilibrium structure at xLi = 0.75, with its free energy being 1.9 and 1.5 meV/atom below the interpolated free energy of the BCC solid solution at T = 200 K and 300 K, respectively. This could potentially indicate that D03-$AgLi_3$ is a new phase within the BCC lattice; however, this claim may lack statistical robustness considering the magnitude of the interpolation error(~1 meV/atom) and the BCC CE error(3.3 meV/atom). Further results from semi-grand canonical MC simulations on the BCC lattice can be found in the Supplementary Information, showing the presence of the D03-$AgLi_3$ structure manifests in chemical potential–composition curve at xLi = 0.75 when T ≤ 300 K. This finding suggests that D03-$AgLi_3$ may indeed precipitate from the disordered BCC solid solution as a new phase when x_{Li} ~ 0.75 and T≈300 K. The Supplementary Information also features simulated XRD patterns of the BCC D03-$AgLi_3$ structure and a representative γ-brass structure at x_{Li} = 0.75 drawn from MC samples. These patterns suggest a significant structural similarity between the two structures such that they might not be easy to distinguish in experiments. Therefore, it is possible that the previously reported γ_2 phase might in fact be BCC D03-$AgLi_3$. The γ_1 phase described by Freeth and Raynor could potentially represent a Li solid solution as no phase transformation can be identified in our calculations for xLi > 0.85. The free energy difference between BCC and γ-brass in *Figure 3.3* is very small, usually less than 5 meV/atom. This similarity in energy can be rationalized by their structural similarity (*Figure 3.1-c*) given that γ-brass is essentially BCC with vacancies and partial ordering. The energy similarity of BCC and γ also hints at the possibility that once Ag is lithiated over x_{Li} ~ 0.6, the Ag–Li system

will behave practically as a BCC solid solution that retains a driving force to absorb Li, even though some γ phases can form and coexist with the BCC solid-solution.[36]

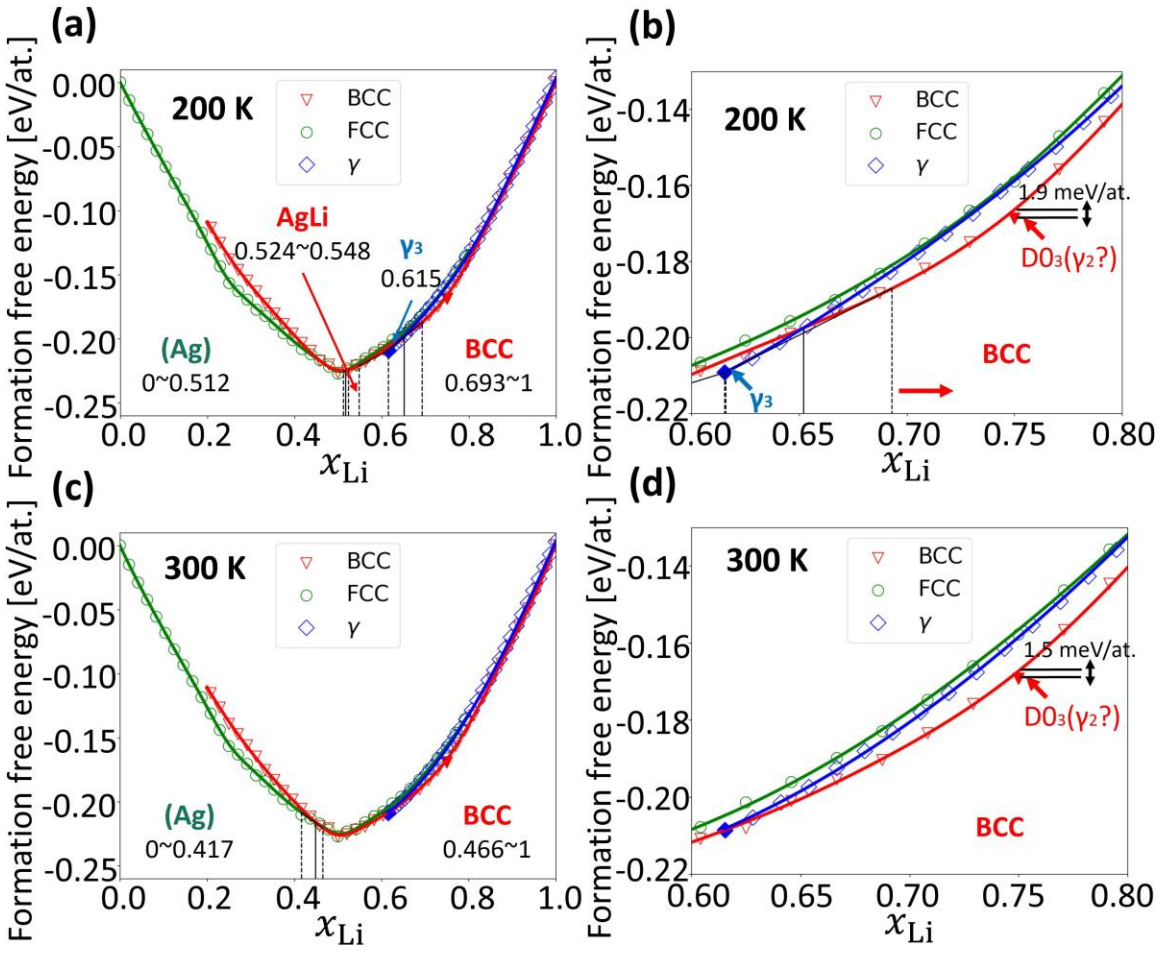

Figure 3. 3. Formation free energy of Ag–Li BCC (red), FCC (green), and γ (blue) phases as a function of Li content (xLi) at T=200 K (a–b) and 300 K (c–d). (a) and (c) show free energy functions in the range of xLi = 0 ~ 1. (b) and (d) show free energy functions in the range of xLi = 0.6 ~ 0.7. Predicted phase boundaries are marked with black dashed lines, and the intersections between the free energy curves are marked with black solid lines.

We considered both the equilibrium voltage curve derived from these free energy curves as well as possible non-equilibrium voltage behavior through the phase transitions. The phase transformations within the Ag–Li system can be broadly classified into two types:

- Incoherent transformations. These transformations involve changes in the crystal lattice geometry, such as the transformations from FCC Ag to BCC β-AgLi, from β-AgLi to γ_3, and from γ_3 to BCC.
- Coherent transformations. These transformations maintain the topology of the lattice while atom ordering on the lattice varies with composition. For example, the formation of $D0_3$-$AgLi_3$ from BCC solid solution.

For incoherent transformations, the Ag lithiation potential can be estimated by differentiating

the free energy along two transformation paths, as indicated in *Figure 3.4-a,b*:

1. The equilibrium path, represented with green arrows, involves phase segregation to form distinct phases separated by moving interfaces, causing the free energy of the system to follow the common tangent line in the two-phase region ($x_\alpha < x_{Li} < x_\beta$).
2. The over-saturation path, depicted by purple arrows, includes over-lithiation of Ag particles past the equilibrium composition ($x_{Li} > x_\alpha$) until the particle undergoes spontaneous transformation between phases at fixed composition, thereby avoiding the need for long-range diffusion and two-phase coexistence. Such a process occurs when particle sizes are small, and phase separation is energetically unfavorable due to the energy penalty of forming interfaces.[127]

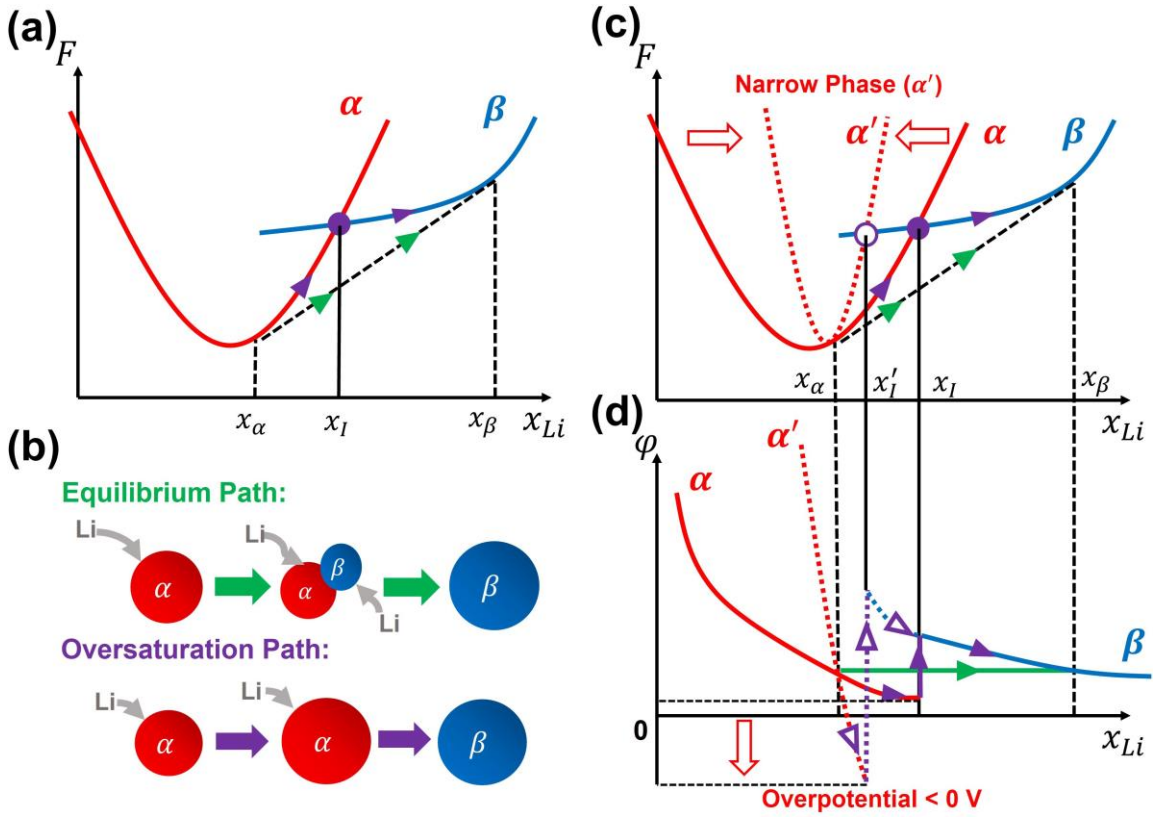

Figure 3. 4. (a)The path of metal-Li free energy (F) during lithiation when undergoing an equilibrium (green arrow) or over-saturation (purple arrow) transformation from the α phase (red curve) to the β phase (blue curve). x_α, x_β, and x_I represent the solubility limits of α, β, and the intersecting composition of α and β free energy, respectively. (b) Microscopic mechanism for both the equilibrium and over-saturation transformation. (c) Free-energy paths assuming that the free energy of phase α will increase more rapidly when the composition deviates from the minimum free-energy composition, with a sharper free-energy curve (α′, red dashed curve). (d) Lithiation potential when comparing the original phase α and the narrowed phase α′. The overpotential of α′ drops below 0 V at the intersecting composition x'_1.

Because it can be difficult for phase transformations to occur in equilibrium at room temperature, we assume in this study that oversaturation of a phase can occur as long as the oversaturated phase has a lower free energy than the new phase that needs to form. For the example in *Figure 3.4*, phase α can be metastable up to composition x_I, which is larger than the composition x_α where the equilibrium transition would occur. Such interpretation has previously been used to understand non-equilibrium paths in other intercalation electrodes.[130] Over-saturation reduces the potential of the alloy below the equilibrium potential and can even bring it below 0 V. As *Figure 3.4c* and *3.4-d* show, when the free energy (F) of α(solid red curve) increases more rapidly away from the equilibrium composition x_α, resulting in a narrower curve (α', red dashed curve), the lithiation potential (ϕ) of α' decreases more rapidly below the equilibrium potential for $x_{Li} > x_\alpha$, eventually reaching a minimum overpotential below 0 V. Once the lithiation potential dips below 0 V, lithiation stops within the alloy, instead causing Li-metal deposition elsewhere. Hence, in such a situation, it can be difficult to form the new phase β.

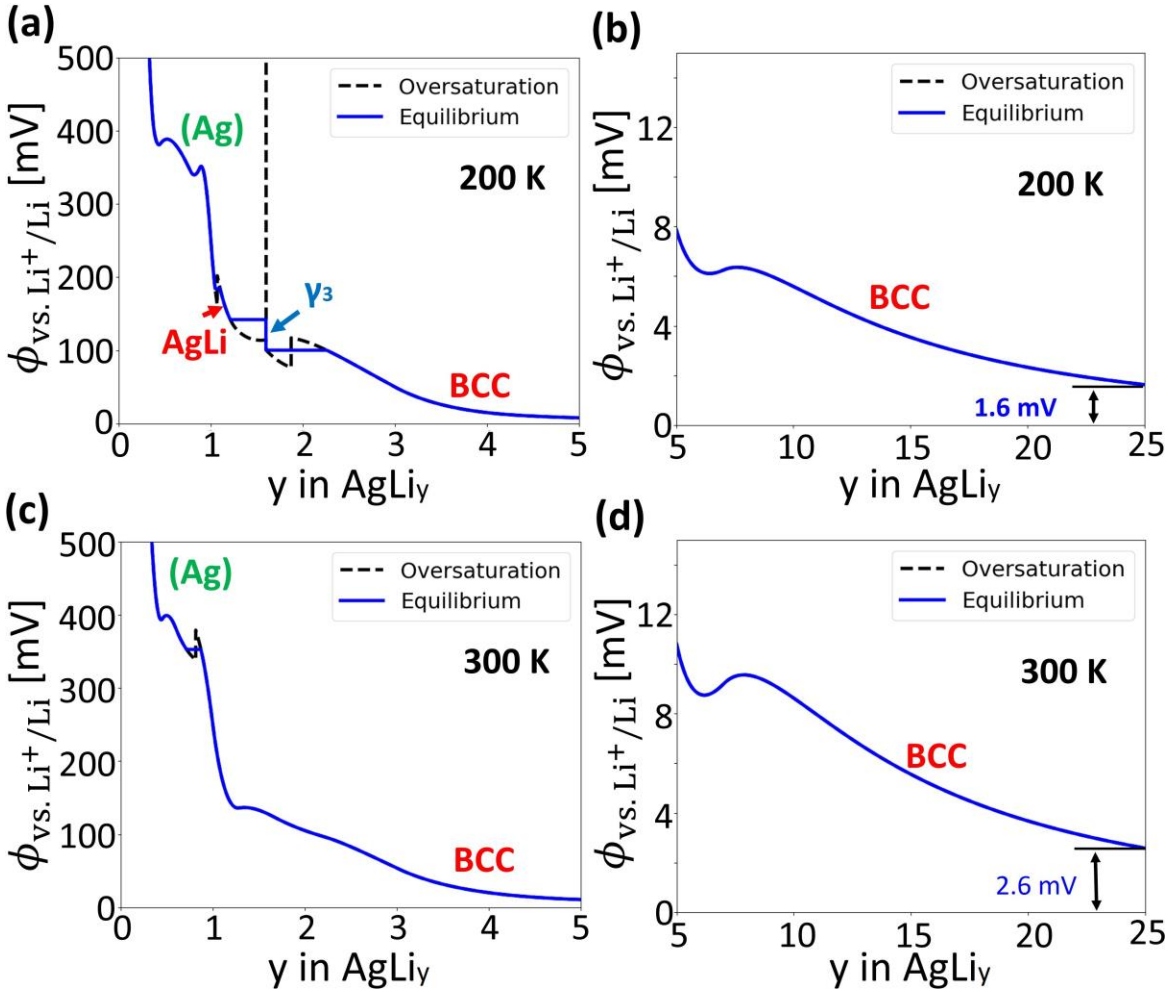

Figure 3. 5. Computed lithiation potentials of Ag from equilibrium (blue solid) and over-saturation (black dashed) paths as functions of y in formula $AgLi_y$, calculated at (a–b) T=200 K and (c–d) T=300 K. (a) and (c) show the lithiation potentials in y = 0 ~ 5, and (b) and (d) show the lithiation potentials in y = 5 ~ 25.

For the coherent transformation between BCC-Li and BCC $D0_3$-$AgLi_3$, the formation of $D0_3$-$AgLi_3$ can be reasonably disregarded. In-situ XRD experiments[131] suggest that the formation of $D0_3$-$AgLi_3$ (denoted as Ag_3Li_{10} by Spencer-Jolly *et al.*) is slow under high charging current, with noticeable Ag_3Li_{10} formation after ~ 1 h at 2 mA/cm^2.

Figure 3.5 shows the Ag lithiation potential as a function of y in the formula $AgLi_y$ at temperatures of 200 K and 300 K. At these temperatures, no incoherent transformations occur that would yield a negative over-saturation potential (see *Figure 3.5-b* and *3.5-c*), indicating that they can occur without causing Li plating reactions. As shown in *Figure 3.5-b* and *3.5-d*, even at a high Li content (y = 25), Ag possesses a positive lithiation potential of 1.6 and 2.6 mV at 200 K and 300 K, respectively. As a result, Ag will continue to lithiated, forming a solid solution, and the Ag–Li alloy will maintain this ability, even at very high Li content. The chemical driving force introduced by Ag is essential in rationalizing its role in equalizing Li deposition, as will be demonstrated in the Discussion section.

3.4.2.b ***Transport of Ag and Li in the Ag/C BL***

Figure 3.6-a provides the schematics of a BL model used to investigate the dominant factors governing the transport and reactions of Ag and Li inside the BL. This model BL is comprised of an Ag particle (green) of diameter d = 40 nm in the center and an amorphous carbon layer (dark grey) of thickness H = 10 μm.[33] The Li-ion conductivity of the BL is estimated to be 1 mS/cm.[80] Given that carbon lithiates before silver[36], the amorphous carbon is assumed to be saturated already to LiC_6 and serve as a mixed ionic-electronic conductor (MIEC) due to its substantial ionic and electronic conductivity.[132–135] It is important to note that we reference a 40% porosity in the BL, which is derived from the data provided by Lee et al.[33] This estimation is inherently subject to the influence of the material's microstructure, the methodologies employed during pre-processing, and the external conditions such as the stacking pressure. Consequently, the actual BL could be denser than our estimations, potentially driving the true porosity well below 40%. Additionally, given the relatively small amount of Ag (constituting merely 1.6% of the BL's volume[33]) in comparison to the BL's porosity (approximated at 40% of the BL's volume), it is likely that Ag particles might not be present within every pore. Considering that an Ag particle is only required to occupy the pore it resides in to effectively extrude, the volumetric expansion necessary prior to Ag extrusion could also be less than that required by the 40% estimation. Given these considerations, determining the exact volumetric expansion required for extrusion could be challenging. Thus, we employed a 40% porosity estimate for demonstrative purposes in our study, while welcoming future experimental works to accurately determine the BL's porosity. The detailed simulation parameters are provided in the Supporting Information.

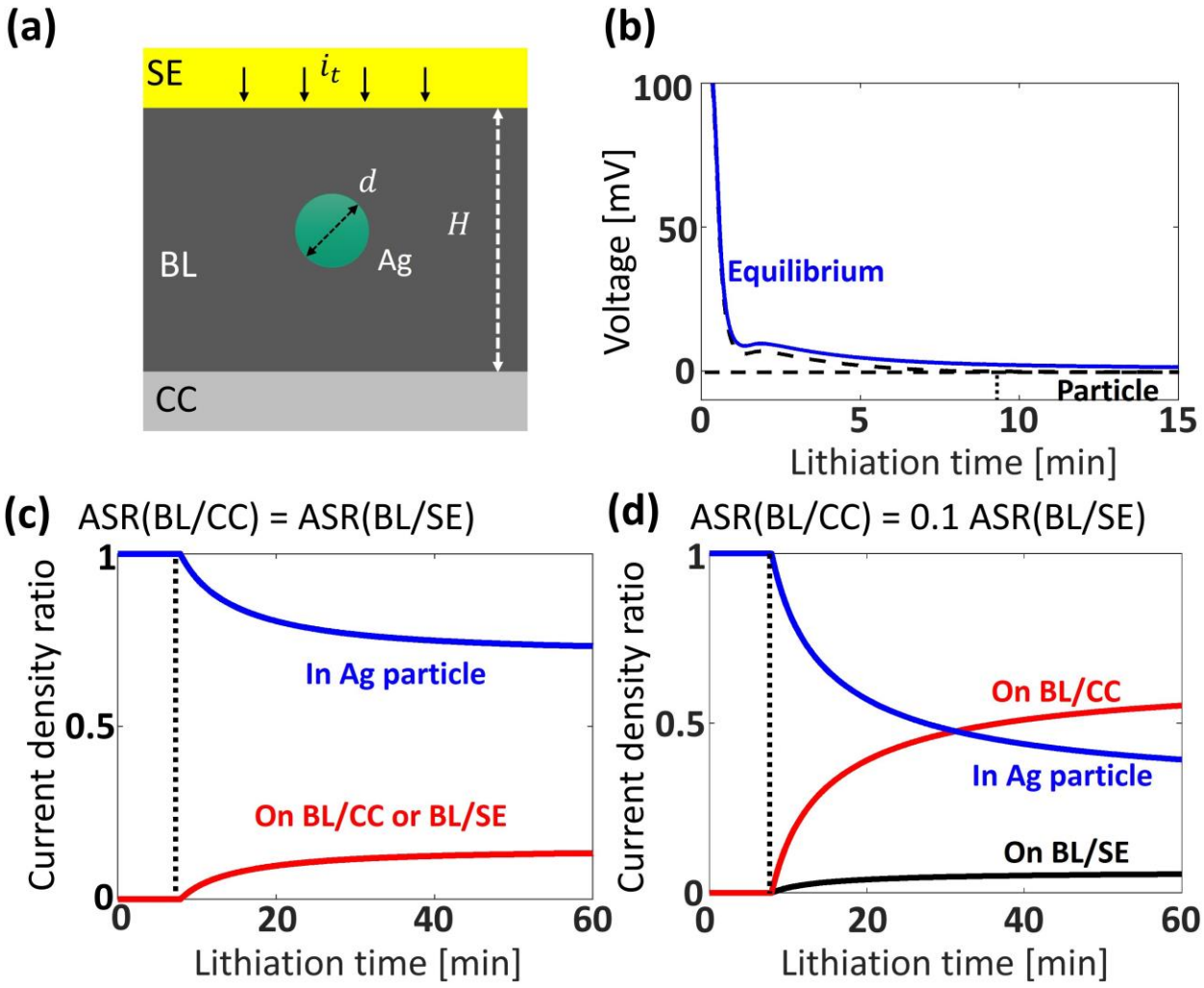

Figure 3. 6. Continuum simulation results of a single particle in the BL under symmetric (ASR(BL/SE) = ASR(BL/CC) = 20 Ω*cm^2) and asymmetric interface ASRs (ASR(BL/SE) = 20 Ω*cm^2, ASR(BL/CC) = 2 Ω*cm^2). (a) Simulation setup. A silver particle (green) of diameter d = 40 nm was placed within a BL (grey) of thickness H = 10μ m, and the system was lithiated under a constant current density i_t = 0.68 mA/cm^2. (b) Simulated electrochemical potential of the Ag particle (black dashed) and the equilibrium bulk potential (blue solid) as functions of lithiation time. (c)–(d) Ratio of Li current flowing into the Ag particle, depositing on the BL/CC and BL/SE interfaces as functions of lithiation time, assuming (c) equal ASRs on the BL/CC and BL/SE interfaces and (d) lower ASR on the BL/CC interface.

Continuum transport simulations were performed under constant lithiation current density of i_t = 0.68 mA/cm^2 for two scenarios: (1) equivalent interfacial charge-transfer area-specific resistance (ASRs) at interfaces BL/SE and BL/CC of 20 Ω*cm^2 to highlight the alloying effect from the Ag particle; (2) nonequivalent interfacial charge-transfer ASRs (BL/SE: 20 Ω*cm^2, BL/CC: 2 Ω*cm^2, *Figure 3.6-d*) to represent a more realistic scenario as the ASR at the BL/CC interface is lower than that at the BL/SE interface[136,137]. *Figure 3.6-b* illustrates the evolution of the voltage in the Ag particle as a function of lithiation time by assuming that the Li distribution within the Ag nanoparticle can be homogenized instantly. The blue curve represents the equilibrium lithiation

voltage re-plotted from *Figure 3.5-a* and *3.5-b* with the x-axis converted to lithiation time under the given charge rate. The potential of the actual Ag particle (black dashed) declines more rapidly than the equilibrium potential in the bulk alloy due to the additional overpotential required to overcome the Li-ion transport resistance in the bulk BL and the charge transfer resistance at the Ag/BL interfaces (*Figure 3.6-b*) . *Figure 3.6-c* and *3.6-d* show the fraction of Li current alloying with the Ag particle or depositing on the BL/SE and BL/CC interfaces as functions of lithiation time. In *Figure 3.6-c* the ASRs for BL/SE and BL/CC are equal, whereas in *Figure 3.6-d* the ASR at BL/CC interface is lower. At the beginning of lithiation, the Ag particle exhibits a positive potential, absorbing nearly all the Li. However, after ~ 8 min, the Ag particle potential becomes negative (dashed lines), triggering Li deposition on the BL/SE and BL/CC interfaces. When the ASRs at both interfaces are equal, Li deposits at approximately equal rates on the BL/SE and BL/CC interfaces, as shown in *Figure 3.6-c*. However, studies[33,34,136,137] suggest that the ASR at the BL/CC interface is usually lower than that at the BL/SE interface, causing the CC side to attract a larger portion of Li current as is evident in *Figure 3.6-d*.

As lithiation continues, the Ag–Li alloy expands within the pores of the BL and densifies it. According to the research of Lee *et al*.[33,34], Ag particles initially constitute roughly 2% of the total volume in the BL, which possesses an initial porosity of approximately 40%. We used these values to plot (*Figure 3.7-a*) the relative volume percentage the Ag–Li will take up in the BL as a function of time at a charge rate of 0.68 mA/cm^2. The volumes of $AgLi_y$ alloys are taken from the DFT computations. At a current density of 0.68 mA/cm^2, Ag particles are expected to expand and entirely occupy the pores within the BL after ~ 15 min. At this point, internal stress begins to accumulate, eventually causing separation at either the BL/SE or BL/CC interface. *Figure 3.7-c* quantifies the evolution of internal hydro- static pressure in the BL with lithiation time, assuming that the adhesive strengths at both the SE/BL and CC/BL interfaces are substantial enough to preserve the interfacial bonding. Under this assumption, the internal pressure can reach a maximum of ~ 8 MPa before Ag–Li alloying is restrained by an overpotential emerging from mechanical stress [65,125,138]. Interfacial adhesion is limited and heavily reliant on the properties of the contacting surfaces. Consequently, the interface with lower adhesion strength will be separated first, causing the Ag–Li solid solution to extrude toward that interface, resulting in an elastoplastic flow (*Figure 3.7-b)*. The BL/SE interface has been found to have stronger adhesion than the BL/CC interface[34,136], with respective values indicated by horizontal lines in *Figure 3.7-c*. Once the internal stress is large enough to counterbalance the adhesion strength of the BL/CC interface (~ 2 MPa) and the externally applied stack pressure (~ 1 MPa)[33] the BL/CC interface will separate, relieving the internal stress and causing the Ag–Li alloy to extrude towards the CC.

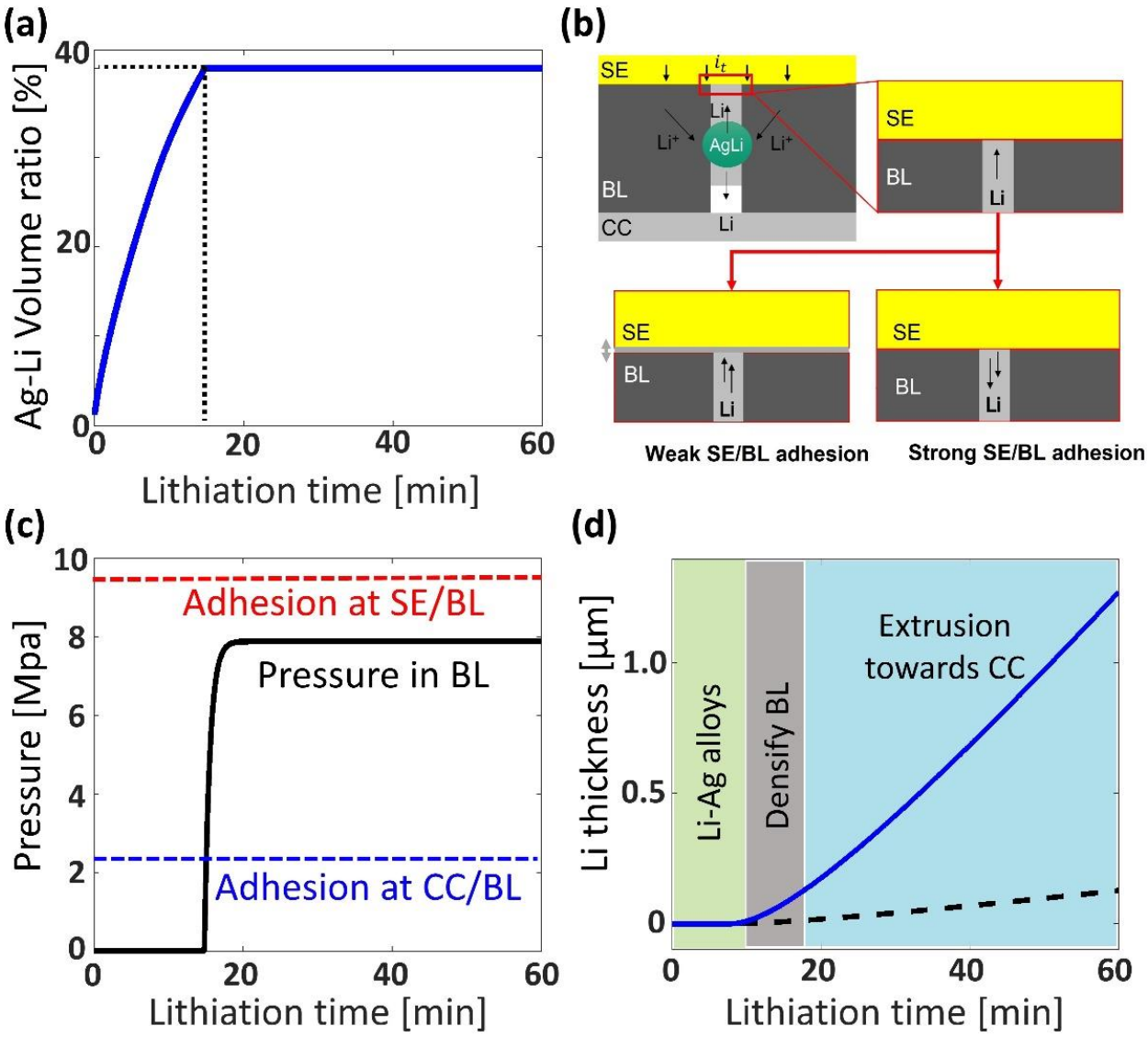

Figure 3. 7. (a) Volume percentage of Ag–Li alloy in the BL as a function of lithiation time, assuming the same experimental conditions as those in the work of Lee et al.[33] .The volume of Ag–Li alloy at varied compositions is estimated from the DFT computations in 2(a). (b) The mechanism for interface separation between the BL and SE. When the adhesion on the SE side is weaker than that on the CC side, the BL/SE interface separates first, and the solid solution extrudes towards the SE. When the adhesion on the SE side is stronger than that on the CC side, the BL/CC interface separates first and the solid-solution extrudes towards the CC. (c) Calculated internal stress as a function of lithiation time in an anode-free setup using LLZO as the SE. (d) Calculated evolution of deposited Li layer thickness as a function of the lithiation time on BL/SE and BL/CC interfaces combining electrochemical and mechanical effects.

Figure 3.7-d combines both electrochemical factors (ASR) and mechanical factors (volume expansion, surface adhesion, plastic flow) to portray the evolution of the Li deposition thickness at the BL/CC and BL/SE interfaces with lithiation time. Ag particles are lithiated in the BL during the initial ≈ 10 min without significantly filling the BL pore volume. Over the next ≈8 min, the BL is densified as the Ag–Li alloy expands into the BL pores. During the subsequent

≈45 min, the Ag–Li solid solution mechanically extrudes toward the CC. This mechanism accounts for the predominant migration of Ag toward the CC after lithiation, as observed in scanning electron microscopy studies.[33,34] Overall, the preference of Li metal to deposit on the BL/CC interface can be explained by the lower interfacial charge transfer resistance and the lower adhesion strength between the BL and CC compared to the BL and SE. The migration of Ag can be attributed to the elastoplastic flow of the Ag–Li solid solution resulting from the alloy's volume expansion and extrusion toward the CC.

3.4.3 Discussion

With a better understanding of the working mechanism of the Ag/C composite BL, we discuss the factors affecting the homogeneity of the Li current. When current concentration in typical intercalation or alloying electrode causes a local increase in lithiation, the local voltage decreases with respect to the rest of the electrode. This negative feedback mechanism reduces current concentration driving the electrode towards more homogeneous lithiation. Because the plating of metallic lithium occurs at constant voltage, no such negative feedback occurs, and a homogeneous current profile is fundamentally unstable leading to dendrite formation. To reduce the current instability one can either try to dampen the instability or provide negative feedback to any local excess Li deposition. Two examples of damping mechanisms, conductivity and ASR increase, are shown in *Figure 3.8*. *Figure 3.8-a* schematically presents a defected interface between the SE and CC, featuring a single 2 μm* 2 μm Gaussian-shaped Li-metal tip positioned on the CC. At a constant lithiation current (i_t = 0.68 mA/cm^2), *Figure 3.8-b* shows the voltage (blue, upper panel) and Li current (red, lower panel) distribution on the interface. Indeed, as the tip protrudes into the SE it presents a higher voltage (lower chemical potential) to the arriving lithium so that an excess Li plates at the tip. In our simulation, the 2 μm wide tip attracts nearly 7% of the total current in the 50 μm area around it, despite being only 4% of the line area. Improvement in the Li-ion conductivity of the SE can enhance the current homogeneity and reduce the speed at which dendrites grow. This behavior is displayed in *Figure 3.8-c* where the Li current becomes less concentrated at the tip as the SE ionic conductivity increases. This can be understood from the fact that an SE with high ionic conductivity (σ) effectively redirects current density (j) laterally to mitigate the voltage difference (ΔV) within a length l from the protruding defect tip and can be qualitatively understood with the Ohmic relation $j = \frac{\sigma}{l} \Delta V$. For example, at a constant current of 1 mA/cm^2, if the ionic conductivity is increased from 0.1 mS/cm to 1 mS/cm, the length scale over which the voltage drops by 1 mV will be increased from 1 μm to 10 μm.

Similarly, maintaining an appropriate ASR on the CC surface can also lead to more homogeneous Li plating. *Figure 3.8-d* illustrates how a decrease in the ASR exacerbates the Li current inhomogeneity, thereby increasing the risk of dendrite formation. This can be easily understood since a high ASR essentially "backs up" current at the interface negating any voltage advantage of a dendrite tip. However, it is important to note that although a relatively raised ASR aids in suppressing dendrite growth, an excessively high ASR can result in high internal resistance, which is detrimental to the power density of the cell. Thus, an optimal interface design should account for the

trade-off dictated by the interfacial ASR value. It should also be noted that the ASR that is varied in *Figure 3.8-d* is the actual ASR of a SE/CC or BL/CC contact, unlike the macroscopically measured ASR which often reflects the presence of voids. An increase of ASR because of voids will lead to increased current inhomogeneity due to the reduction in contact.

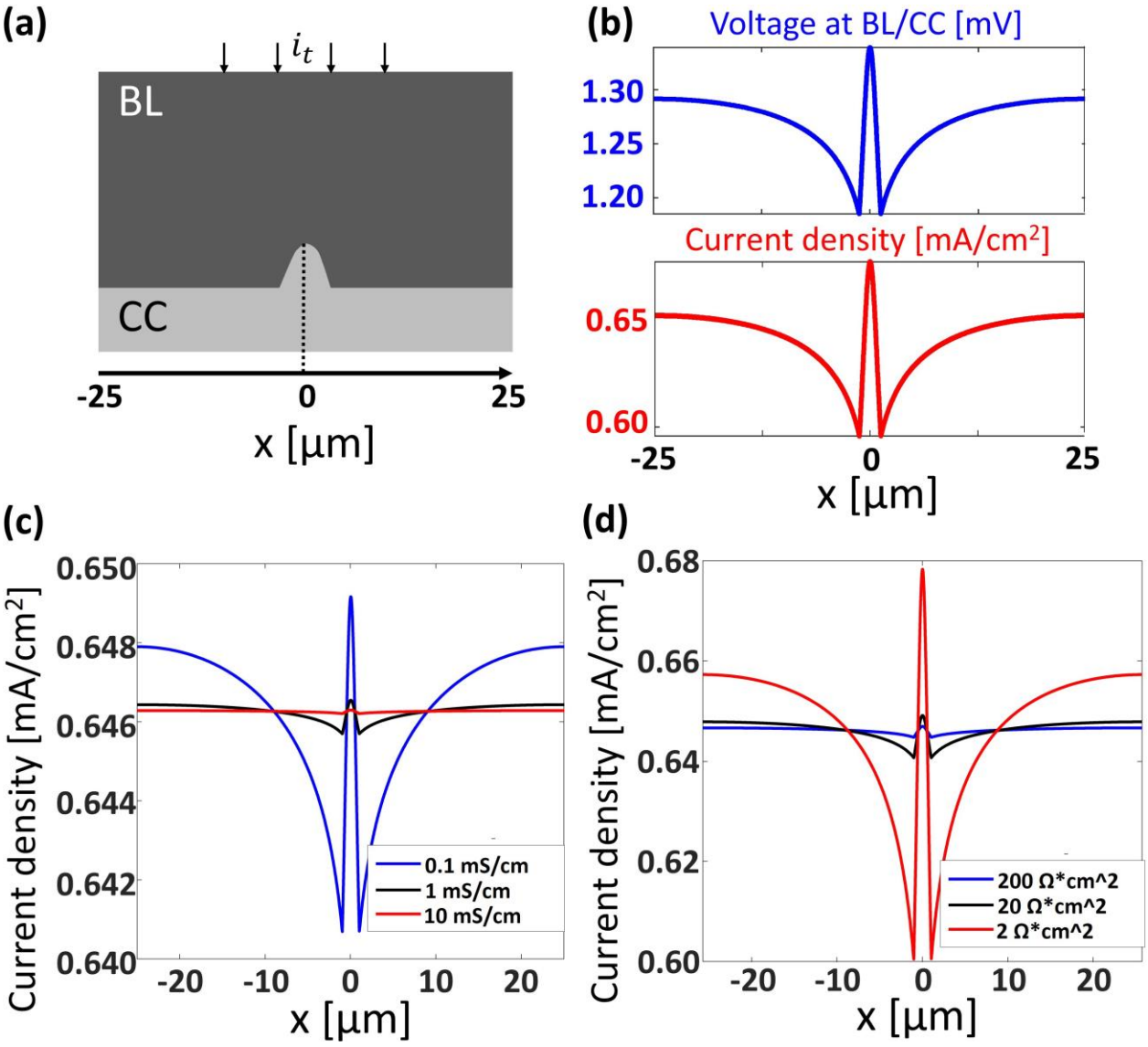

Figure 3. 8. (a) Schematics of a model interface between the SE and CC with a single 2μm * 2μm tip defect on the CC. The x-axis measures the horizontal distance from the tip center. (b)Simulated distribution of voltage (blue, upper panel) and Li current (red, lower panel) on the defected interface. The SE ionic conductivity is set to 1 mS/cm and the ASR is set to 2Ω*cm^2. (c)Simulated distribution of Li current on the defected interface at varied SE ionic conductivity: 0.1 mS/cm(blue), 1 mS/cm(black, close to the conductivity of LPS), and 10 mS/cm(red). The interfacial ASR is fixed to 2Ω*cm^2. (d)Simulated distribution of Li current on the defected interface at varied interfacial ASR: 200Ω*cm^2 (blue), 20Ω*cm^2 (black), and 2Ω*cm^2 (red, close to the ASR between LPS and Li metal). The ionic conductivity of the SE is fixed to 0.1 mS/cm.

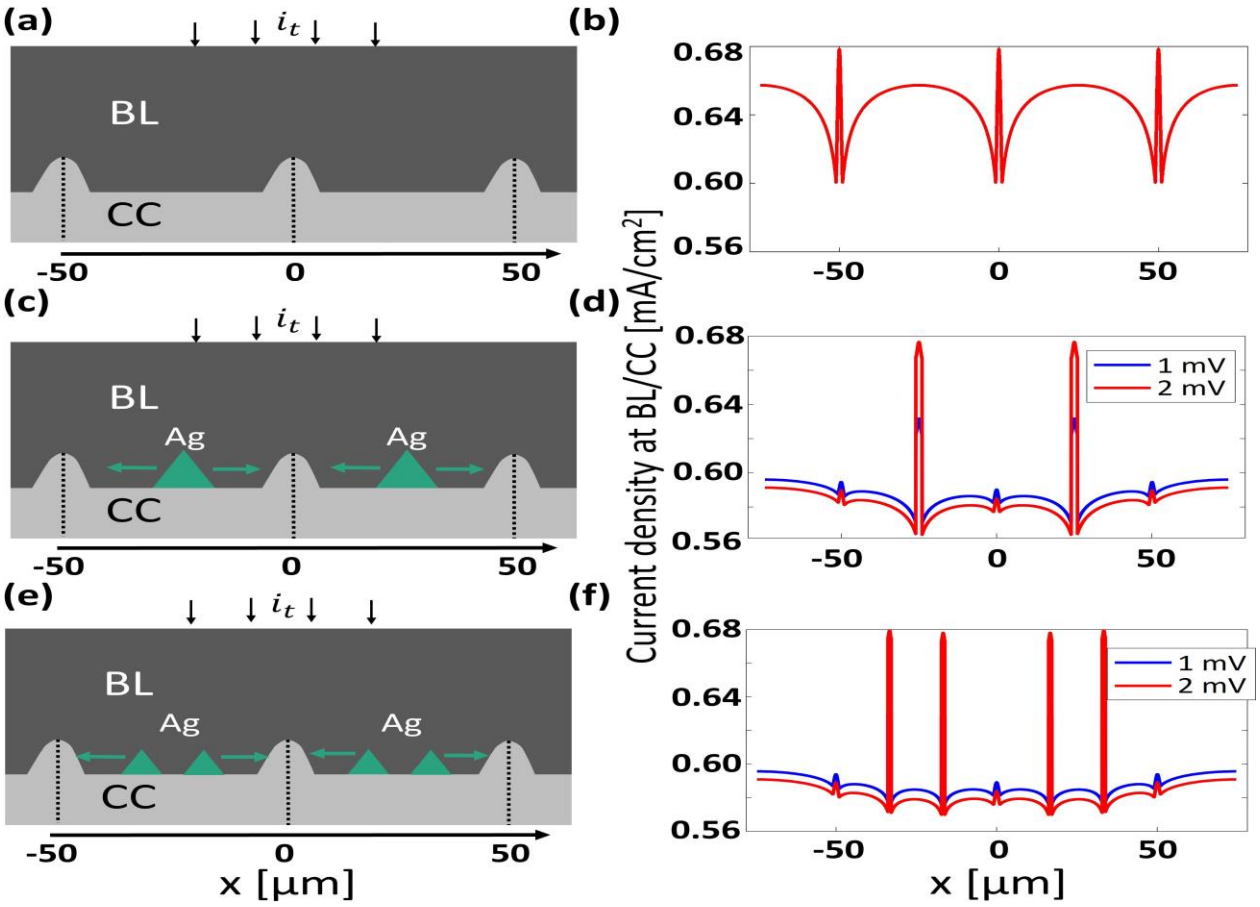

Figure 3. 9. Effect of Ag particles on Li current distribution on a defective SE/CC interface. Simulations were performed imposing a constant average current i_t=0.68 mA/cm^2 at the top surface. The SE ionic conductivity is fixed at 1 mS/cm and the ASR is fixed at 2Ω*cm^2. (a) Schematics of a SE/CC interface having three 2μm * 2μm tip defects on the CC with a 50μm distance between peaks. No Ag particles are included. The x-axis measures the horizontal distance from the central tip. (b) Simulated current distribution on the x-axis by using the schematics described in (a). (c) Schematics of a SE/CC with three tip defects, as described in (a), and two additional 2μm * 2μm Ag particles at x = −25μm and x = 25μm. (d) Simulated current distribution on the x-axis for the geometry in (c). A lithiation driving force of 1 mV (blue) and 2 mV (red) is added to the regions where a Ag particle is present. (e) Schematics of a SE/CC with three tip defects, as described in (a), and four additional 1μm * 1μm Ag particles at x = −33.3μm, x = −16.7μm, x = 16.7μm, and x = 33.3μm. (f) Simulated current distribution on the x-axis by using the schematics described d in (e). A lithiation driving force of 1 mV (blue) and 2 mV (red) is added to the regions where an Ag particle is present.

While increases in the ASR or ionic conductivity dampen the current concentration caused by inhomogeneities, the presence of Ag as an alloying component of the electrode can con- tribute negative feedback to excess current in a particular area. We show the influence that Ag particles on the current collector have on the current distribution in *Figure 3.9-c,f*. To simplify the problem, we assume that Ag particles introduce a lithiation driving force of either 1 mV(blue) or 2 mV(red). This example is intended to understand the modification of the current distribution when even minor cathodic potential variations occur. In the absence of Ag particles (*Figure 3.9-a* and *3.9-b*), the Li current concentrates at defect centers, as expected. However, with the introduction of a small

amount of Ag nanoparticles between the tip defects (*Figure 3.9-c* and *3.9-d*), the Li currents are redistributed from the defects and preferentially flow towards the Ag. Remarkably, even with only a 1 mV difference in local potential, the Ag can pull current away from the defect, which is 25 μm away, illustrating the remarkable influence of small voltage variations on the anode, and pointing at the potential to artificially engineer Li deposition sites and homogeneity. When the total amount of Ag is kept constant, a larger amount of small Ag nanoparticles (*Figure 3.9-e* and *3.9-f*) is more effective than fewer large particles, as more sites can be created to attract Li, thereby further preventing growth of the tip. As Ag particles lithiate and expand, the roughness on the CC surface can be filled, resulting in a more uniform surface for subsequent Li deposition. Hence the benefits of Ag nanoparticles at the CC may arise from the creation of a homogeneous set of Li nucleation sites, unrelated to the interfacial unevenness, as well as from its ability to fill in surface roughness through its large volume expansion upon lithiation. Ag nanoparticles at the interface effectively hide the surface irregularities from the current.

We now turn our attention to the specific and rather unique role that Ag–Li chemistry plays. The superior performance of Ag over other metals (Sn, Zn, Al, Ni, etc.) in the experiments of Lee *et al*.[33] can be attributed to its ability to maintain an attractive driving force through the formation of a wide-ranging solid-solution. *Figure 3.5-d* shows that even for y = 25 in $AgLi_y$ the alloying potential is above zero. Using the Zn–Li system as a comparative system, we illustrate the challenges in substituting Ag by other metals. *Figure 3.10-a* presents the composition–temperature phase diagram of Zn–Li, reproduced from the work of Pelton[139]. At room temperature, various compounds with narrow homogeneity ranges exist, including Li_2Zn_5, $LiZn_2$, Li_2Zn_3, and LiZn. A narrow phase field implies a rapid increase of free energy with Li excess and, therefore, a sharp free-energy landscape. As shown in *Figure 3.4-c,d* compared to the α phase, the potential of the α' phase with a sharper free energy drops more rapidly as it is overlithiated. Once the lithiation potential becomes negative, the alloy particle will cease to attract Li flow and redistribute Li currents, potentially causing dendrite formation. *Figure 3.10-b* illustrates the non-equilibrium lithiation potential of Zn at T = 300 K computed from a CALPHAD model[140] by Liang *et al*.[141].The Zn–Li system exhibits significant negative overpotential across phases Li_2Zn_3 (-3.4 mV) and LiZn (-19.0 mV), suggesting that Zn is likely to stop lithiating prematurely and lose its attractiveness to Li unless two-phase nucleation can occur.

Table-3. 2. Ratio (R) of volume expansion in various metals at the maximum-Li-content phase, measured at room temperature and 1 atm. Molar volumes of the metal–Li alloys and the pure metal were computed from XRD data, as referenced. The data of Pt is marked with "?" as the phase $PtLi_5$ has not been confirmed

Metal	Phase	Max x_{Li}	R	References	Metal	Phase	Max x_{Li}	R	References
Ag	γ_1	0.94	17.7	[108]	Bi	$BiLi_3$	0.94	2.1	[142]
Au	Au_4Li_{15}	0.789	4.7	[143]	Pt(?)	$PtLi_5$	0.833	6	[144]
Zn	ZnLi	0.5	2.0	[139]	Ga	$GaLi_2$	0.667	2.4	[145]
Sn	Sn_4Li_{17}	0.809	3.6	[146,147]	Ge	Ge_4Li_{17}	0.809	3.7	[147,148]
Al	Al_4Li_9	0.692	3.4	[149]	Pb	Pb_4Li_{17}	0.809	3.2	[147,150]
Cu	(Cu)	0.25	1.4	[151]	Tl	Tl_5Li_{22}	0.815	3.5	[152]
Ni	(Ni)	0	1	[153]	Sb	$SbLi_3$	0.75	2.3	[154]
Si	Si_4Li_{17}	0.809	4.1	[155,156]	In	In_3Li_{13}	0.812	4.0	[157]

The inability of other metals to absorb enough Li (and hence be unable to expand sufficiently during lithiation) is the reason why other metals do not perform as well as Ag. Two important mechanisms are controlled by the maximum Li uptake in the metal. The more Li the metal takes up, the longer the current at the anode is controlled by the dispersion of the metal, rather than by geometric irregularities at the interface. Secondly, if a metal cannot densify pores in the BL after alloying with Li, it will not be able to extrude towards the CC and cannot precipitate on the CC after delithiation. Table-3.2 estimates the volume expansion ratio (R = Metal–Li molar volume/Pure metal molar volume) of various metals at ambient conditions from experimentally measured crystal structure and phase diagram data, under the assumption that all metals can be maximally lithiated to their most Li-rich alloy phase. As argued in our example, for Zn–Li this may actually be an overestimation. Ag provides the largest volume expansion ratio (R = 17.7) compared to all other metals in the table, which mostly stop at $R < 4$. It is likely that Ag is the only metal capable of expanding sufficiently to extrude from the pores and deposit uniformly as nanoparticles on the CC surface after the first few cycles. Even accounting for the overpotential effects at practical current densities, Ag maintains a notable capacity for expansion compared to other metals. As illustrated in *Figure 3.6-b*, at a current density of 0.68 $mA*cm^{-2}$, the electric potential of the Ag particle drops below 0V at around 8 mins, corresponding to approximately y = 25 in AgLiy and thereby occupying roughly 20% of the buffer layer's (BL's) volume (*Figure 3.7-a*). This behavior of Ag significantly contrasts with that of other metals, which cease to absorb Li at much lower Li contents. However, despite their inability to migrate during the pre-cycling like Ag, other metals could still be used to guide the Li current if their nanoparticles can be uniformly distributed on the

CC during anode pre-processing. This has recently been evidenced by the study of Haslam *et al.* using Au nanoparticles as nucleation sites[37]. Achieving this requires understanding the specific characteristics of each metal and the corresponding processing methods when designing LMSSB systems.

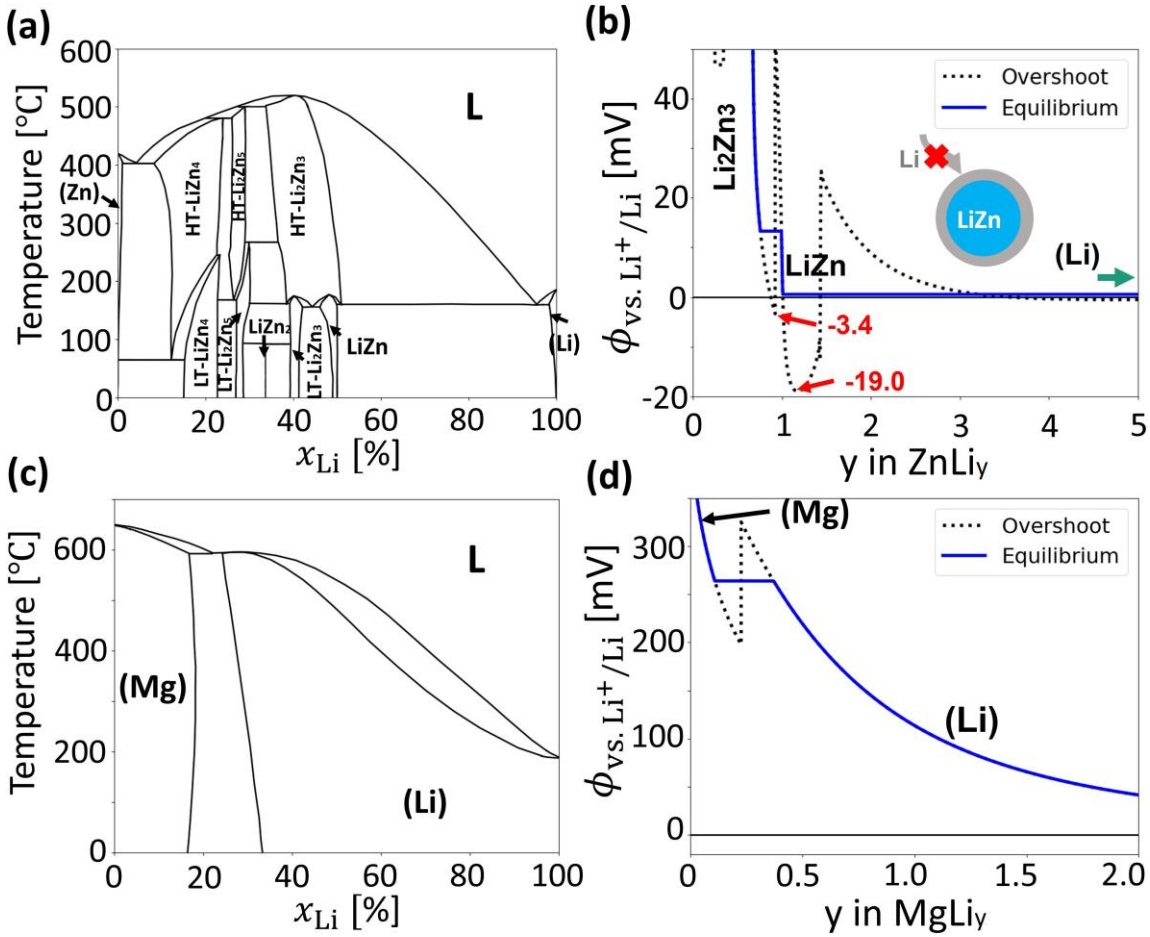

Figure 3. 10. (a)Composition–temperature phase diagram of the Zn–Li system, redrawn from Pelton[139]. (b)Lithiation potential of Zn as a function of y in formula ZnLiy at T=300 K, computed from a CALPHAD model. Both the equilibrium (blue solid) and over-saturation potentials (black dashed) are plotted. The sub-figure shows the Zn–Li alloy being unable to absorb more Li because of the negative overpotential. (c)Composition-temperature phase diagram of the Mg–Li system reproduced from Nayeb et al.[158]. (d)Lithiation potential of Mg as a function of y in the formula MgLiy at T=300 K computed from a CALPHAD model[159]. Both the equilibrium potential (blue solid) and over-saturation potential (black dashed) are plotted.

Finally, our research suggests that Mg could also serve as a promising candidate for the BL. As illustrated by the Mg-Li phase diagram[158] (*Figure 3.10-c*). Mg and Li possess high intersolubility without the presence of any intermediate phase. *Figure 3.10-d* indicates that the lithiation potential of Mg, computed from the model of Braga *et al.*[159], remains above 0 V. Therefore, Mg might operate via a solid-solution mechanism similar to that of Ag in the BL. Employing Mg in anode-free battery design could thus be a promising future direction for research, though its high enthalpy of oxidation could make it challenging to use as a pure metal.

In summary, *Figure 3.11* demonstrates the microscopic operating mechanism during the initial few charge-discharge cycles within an Ag/C BL. At the beginning of lithiation, the amorphous carbon within the BL rapidly saturates with Li and subsequently functions as an MIEC. The Ag particles then begin alloying with Li, forming a solid-solution phase. As lithiation continues, the Ag–Li alloy expands and separates the BL/CC interface under internal pressure, leading to extrusion towards the CC. Meanwhile, the remaining Ag and Ag-rich phases dissolve into the solid solution and plastically flow toward the CC. During delithiation, Li is extracted from the solid solution, resulting in the precipitation of Ag as uniformly distributed nanoparticles on the CC. These Ag nanoparticles help guide Li currents away from surface tips, suppressing surface coarsening and dendrite growth in subsequent cycles.

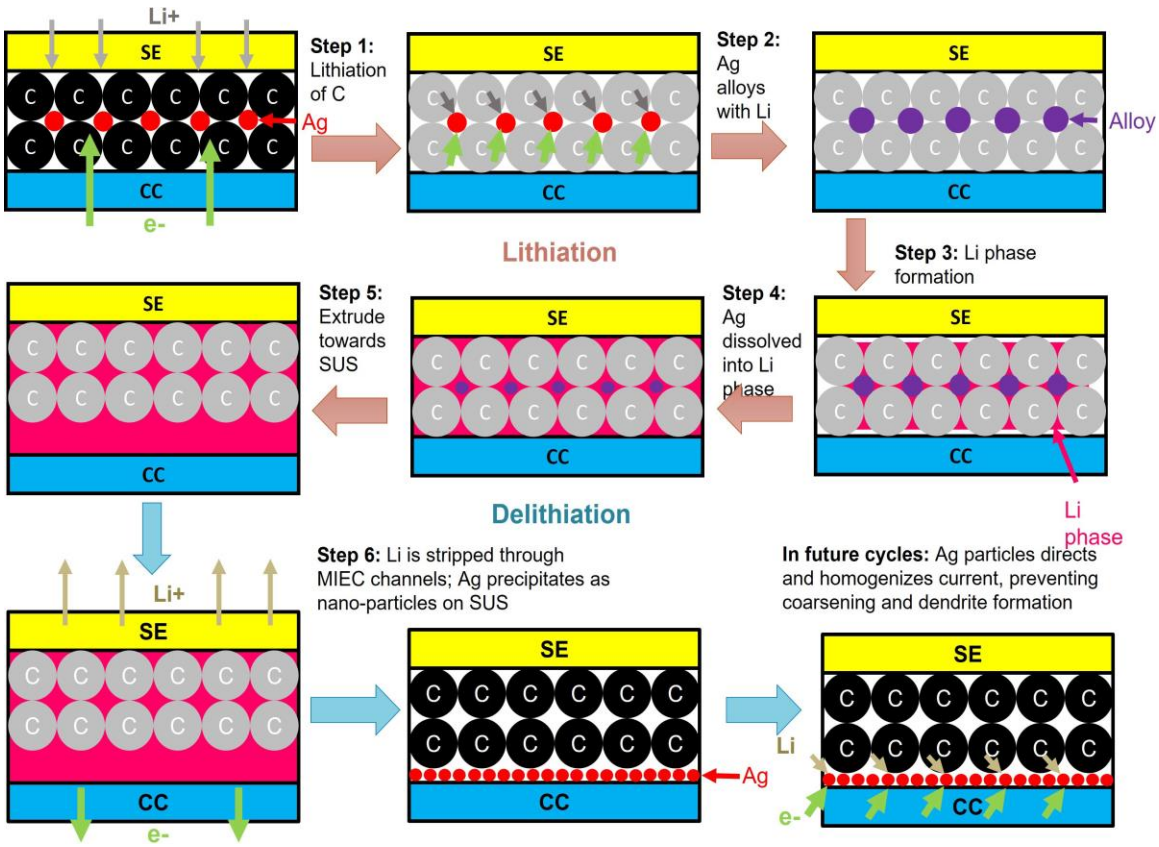

Figure 3. 11. Proposed microscopic lithiation-delithiation mechanism of Ag/C BL during the first few cycles in the Ag/C BL. Amorphous carbon particles are shown as black and gray circles before and after saturating with Li, respectively Ag-metal particles are drawn as red circles. Ag-rich phases in the Ag–Li mixture is marked as purple circles while the Li-rich solid-solution is colored pink.

3.5 Conclusion

By integrating first-principles thermodynamic calculations and continuum modeling approaches, we have examined the lithiation and delithiation processes in Ag/C BL for an anode-free LMSSB. Our study identifies several key properties of the Ag–C buffer layer in creating homogeneous Li plating

conditions. Computationally, we found that Ag can continuously alloy with and dissolves into Li, forming a solid solution that consistently presents a positive attraction potential to Li, even at the $AgLi_{25}$ stage. This is unlike other metals for which equilibrium or non-equilibrium lithiation leads to negative potential at low Li content. This capability of Ag to absorb Li renders Ag nanoparticles as sinks to the Li flow, effectively homogenizing the current and mitigating the risk of Li-dendrite formation due to uncontrolled growth on surface defects. The large volume expansion is key to extruding the Ag–Li alloy from the pores, carrying Ag towards the CC where it is most effective in homogenizing the current. Our continuum modelling reveals that Li deposition is more favorable at the BL/CC interface than at the BL/SE interface, due to the lower interfacial resistance (ASR). The extrusion process predominantly occurs towards the CC due to the stronger surface adhesion between the SE and BL compared to that between the CC and BL. Our study also suggests that other metals may not perform well as they exhibit possible negative overpotentials due to near-stoichiometric compounds, cease to lithiate early, or lack the ability to sufficiently expand during lithiation.

3.6Methodology

3.6.1 DFT calculations

DFT calculations were performed within *Vienna ab initio simulation package* (VASP) using the projector-augmented wave method[160,161] with a plane-wave basis set at an energy cutoff of 680 eV and a reciprocal space discretization of 800 *k*-points per Å. Ag 4p electrons were treated as valence electrons. All the calculations were converged to 10^{-5} eV in total energy for electronic loops and 0.01 eV/Å in inter-atomic forces for ionic loops. The calculations relied on the Perdew-–Burke-–Ernzerhof (PBE) generalized gradient ap- proximation (GAA)[162] exchange-correlation functional . Automated choice of parameters in structural relaxations and static calculations was performed using the **Atomate**[163] and **Fireworks**[164] packages.

3.6.2 Cluster expansion and free-energy calculation

The CE model for BCC-related phases (β-AgLi and Li solid-solution) was derived from a conventional BCC cubic cell with a lattice constant a = 3.50 Å(*Figure 3.12-a*) The CE model for the FCC Ag solid-solution phase was constructed using a conventional FCC cubic cell with a = 4.27 Å(*Figure 3.12-b*) The γ phase CE model was constructed from the γ-brass structure with a = 9.62 Å with only B(OT) and C(OH) sites allowed to be occupied by Ag (*Figure 3.12-c*) For the BCC lattice, configurations were enumerated within a diagonal supercell matrix defined by ((3, 0, 0)^T, (0, 3, 0)^T, (0, 0, 3)^T) and a non-diagonal supercell matrix given by ((−2, 2, 2)^T, (2, −2, 2)^T, (2, 2, −2)^T) to minimize the chance of having duplicated correlation functions between clusters. For the FCC phase, supercells ((4, 0, 0)^T, (0, 2, 0)^T, (0, 0, 2)^T) and ((3, 0, 0)^T, (1, 2, 0)^T, (0, 0, 2)^T) were used. For the γ phase, enumeration was performed within the original 1*1*1 cubic cell. The cluster correlation functions were constructed from an indicator site basis.[165] Among clusters with duplicate correlation functions in the feature matrix, only the shorter-ranged cluster was kept. A lasso regularization method[166] was employed, where the l_1-norm of effective interactions (ECIs, **J**) was

incorporated to penalize the objective function ($f(\mathbf{J})$) during the fitting. This step is crucial for improving model sparsity and avoiding overfitting. The regularization hyper-parameter (α) was fine-tuned using a grid-search approach to minimize the 5-fold cross-validation error. The cluster cutoff diameters, count of cluster correlation functions, number of training structures, optimal α, root-mean-square errors (RMSE), and cross-validation errors (CV) from fitting are provided in Table-3.3. No quadruplet cluster could be included in the γ-phase CE within a cutoff of 4.5Å. Further details about the clusters and ECIs can be found in the Supplementary Information.

$$f(\boldsymbol{J}) = ||\boldsymbol{EDFT} - \Pi\boldsymbol{J}||_2^2 + \alpha||\boldsymbol{J}||_1 \quad (1)$$

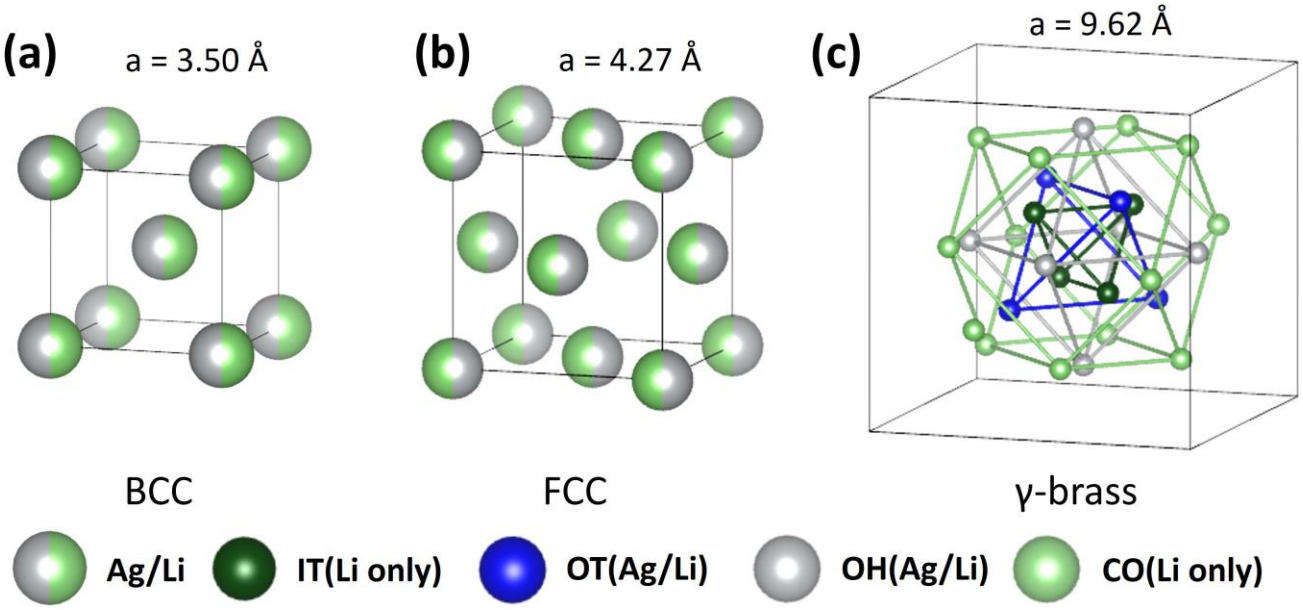

Figure 3. 12. Primitive structures used for cluster expansions in the BCC, FCC, and the γ phase. Ag and Li are allowed to mix on all sites in BCC and FCC, whereas γ allows Ag to occur on OT(B) and OH(C) sites only. For visibility, only half of the sites in γ are shown. Other sites can be obtained by applying the I43m symmetry.

The CE models, which function as effective Hamiltonians, were used to perform MC simulations in canonical ensembles at varying temperatures and compositions (x_{Li}). The simulations were executed within 8*6*6, 6*6*4 and 3*3*2 supercells for BCC, FCC and γ lattices, respectively. The simulation temperature was gradually reduced (*i.e.* , T=10000, 7000, 5000, 3000, 2000, 1500, 1200, 1000, 800, 700, 600, 500, 440, 400, 340, 300, 280, 260, 240, 220, 200, 180, 160, 140, 120, 100, 80, 60, 40, 20 K) to approach the configurational ground states at each x_{Li} and subsequently increased back to 500 K by steps. At each temperature higher or equal to 2000 K, 250,000 metropolis steps were run. For temperatures between 500 K and 2000 K, 500,000 metropolis steps were used. For temperatures below or equal to 500 K, 1,000,000 metropolis steps were used.

$$\beta F_c = \beta_0 E_0 + \int_{\beta_0}^{\beta} \langle E \rangle d\beta, \quad (2)$$

The configurational contribution to free energy at each composition can be evaluated using where F_c is the configurational free energy at temperature T, $\beta = 1/k_BT$, k_B is the Boltzmann constant, $\langle E \rangle$ is the average energy computed at temperature T, and E_0 is the average energy at a very low starting temperature T_0 corresponding to β_0, where configurational entropy can be ignored. In this study, we used T_0 = 20 K, and integrated upwards in T. Only the latter half of the metropolis steps at each temperature were used to compute the average energy to ensure that only the equilibrium distribution is sampled. All programming tools required for building the CE, fitting the ECIs and performing the MC simulations are available in the **smol**[167] and **sparse-lm**[168] packages.

Due to the computational challenges of running phonon calculations for all enumerated structures, and considering that the temperatures of interest are relatively low ($T \approx$ 300 K), we computed the phonon free energy for only the end-point composition structures in each lattice (x_{Li} = 0, 1 for BCC and FCC, x_{Li}= 8/13, 1 for γ) and several ordered ground- state structures at intermediate compositions. Using the quasi-harmonic approximation implemented in Phonopy[169,170], the vibrational frequencies and phonon free energy at T = 0∼10000 K were calculated from a supercell of each structure with a lattice constant $a \sim 10$ Å. We linearly interpolated the vibrational free energy (F_{vib}) of structures over x_{Li} on each lattice and added the interpolated free energies as correction terms to the total free energy (see Supplementary information).

$$F^i(x,T) = F_c^i(x,T) + F_{vib}^i(x,T), \qquad (3)$$

$$\Delta F^i(x,T) = F^i(x,T) - xF^{\mathrm{BCC}}(x = 1,T) - (1 - x)F^{\mathrm{FCC}}(x = 0,T). \quad (4)$$

The total free energy (F^i) of each phase (i =BCC, FCC and γ) was represented as a function of composition (x) and temperature (T) and the formation free energy (ΔF^i) was computed using the free energy of BCC Li ($F^{\mathrm{BCC}}(x = 1, T)$) and FCC Ag ($F^{\mathrm{FCC}}(x = 0, T)$) at the same temperature T as references.

Table-3. 3. Detailed information of CE models, including cluster cutoff diameters, number of fitted clusters (N_c), number of training structures (N_s), RMSE and CV for BCC, FCC and γ.

Model	Cluster cutoffs(Å)	N_c	N_s	α	RMSE(meV/at.)	CV(meV/at.)
BCC	8.0(pair);7.0(triplet);4.5(quadruplet)	25	64	3.8×10^{-6}	3.3	4.8
FCC	8.0(pair); 7.0(triplet);4.5(quadruplet)	32	134	9.5×10^{-7}	1.5	2.5
γ	8.0(pair); 7.0(triplet)	38	96	6.1×10^{-5}	0.5	0.6

The equilibrium lithiation potential in each phase (ϕ^i) at temperature T can be calculated as:

$$e\phi^i(x,T) = F^{BCC}(x=1,t) - F^i(x,T) - (1-x)\frac{\partial F^i}{\partial x}, \quad (5)$$

Where e is the elementary charge.

3.6.3 Mixed ionic-electronic conduction in the Ag/C BL

We described the transport of Li^+ and electron in the BL using the Ohmic relations

$$i_{Li^+} = -\frac{\sigma_{Li^+}}{F}\nabla\tilde{\mu}_{Li^+}, \; i_{e^-} = \frac{\sigma_{e^-}}{F}\nabla\tilde{\mu}_{e^-}. \quad (6)$$

In these equations, $\boldsymbol{i}_{\mathrm{Li}^+}$ and $\boldsymbol{i}_{\mathrm{e}^-}$ represent the current density of Li ion and electron in the BL, respectively. The symbols σ_{Li^+} and σ_{e^-} denote the Li-ion and electronic conductivity of the BL, respectively. Additionally, $\tilde{\mu}_{\mathrm{Li}^+}$ and $\tilde{\mu}_{\mathrm{e}^-}$ are the electrochemical potentials of Li^+ and electron, respectively. The sum of these two electrochemical potentials is required to be equal to the chemical potential of Li in the BL ($\tilde{\mu}_{\mathrm{Li}^+} + \tilde{\mu}_{\mathrm{e}^-} = \mu_{\mathrm{Li}}$). We can further characterize the concentration of Li^+ in the BL by employing both the Ohmic relations and the Nerst-Planck equation, as shown below:

$$\frac{\partial C_{Li^+}}{\partial t} = -D_{\mathrm{Li}^+}\nabla^2 C_{\mathrm{Li}^+} - \sigma_{Li^+}\nabla\tilde{\mu}_{Li^+}. \quad (7)$$

In this equation, D_{Li^+} represents the diffusivity of Li ions in the BL.

3.6.4 Charge-transfer kinetics for Li deposition at the interfaces

The lithiation rate at the interfaces can be represented by the current density of Li^+ participating in the redox reaction. As proposed by Ganser *et al.*[171],the Bulter-Volmer equation provided below reflects the relationship between the interface overpotential (η) and the lithiation current (i_n).

$$i_n = -i_{ex}e^{\frac{(1-\alpha_a)\bar{V}_{Li}\Delta P}{RT}}\left(e^{\frac{\alpha_a F}{RT}\eta} - e^{-\frac{\alpha_c F}{RT}\eta}\right) \quad (8)$$

In the Butler-Volmer equation, i_n represents the local current density normal to the interface and i_{ex} is the reference exchange current density for the Li^+/Li redox reaction. The parameters α_a and α_c denote the anodic and cathodic charge-transfer coefficients, respectively, whereas V_{Li} is the molar volume of the Ag–Li alloy (estimated with that of Li metal). R refers to the ideal gas constant, and F is the Faraday constant. To account for the effect of mechanical stress on Li deposition, we performed a mechanical correction to the interface overpotential, as shown below:

$$\eta = \phi - \phi_{BL} - \phi_0 - \frac{\bar{V}_{Li}\Delta P}{F} \quad (9)$$

Here, ϕ denotes the electric potential at the interface, ϕ_{BL} represents the electric potential in the BL, and ϕ_0 is the equilibrium open-circuit potential without external stress. The symbol ΔP denotes the compressive stress within the BL.

3.6.5 Modelling mechanical stress within the BL

To simulate the development of compressive stress within the BL, we assumed that mechanical equilibrium can be achieved in a much shorter time than chemical equilibrium[172]. Therefore, a quasi-static mechanical equilibrium can always be maintained within the BL. We enforced this equilibrium using the following linear-momentum balance constraint:

$$\nabla \cdot \sigma = 0, \qquad (10)$$

In this equation, $\boldsymbol{\sigma}$ symbolizes the second-order stress tensor that must have zero divergence. The stress tensor can further be decomposed into a deviatoric and hydrostatic component as:

$$\sigma = -P\,I + s, \qquad (11)$$

Here, P represents the hydrostatic pressure ($P = -\frac{1}{3}\,Tr(\boldsymbol{\sigma})$) with positive and negative values indicating compression and expansion states, respectively.

We have derived the evolution of mechanical stress within the BL as follows:

$$\frac{dP}{dt} = \frac{K\bar{V}_{Li}}{VF} I,\ I = \oint i_n dS. \qquad (12)$$

In these equations, V indicates the volume of the alloy particle, K represents the bulk modulus of the alloy (estimated similarly to that of Li metal), and I denotes the total lithiation current integrated across the Ag–Li particle surface. After substituting Equations (8) and (9) into Equation (12) and solving the resulting differential equation, we obtained the following relationship, which was used to compute the stress evolution displayed in *Figure 3.7-c*.

$$P = \frac{\oint F\eta dS}{\bar{V}_{Li}S}(1 - e^{-\gamma t}),\ \gamma = \frac{K\bar{V}_{Li}{}^2 S}{RTFV} i_{ex}. \qquad (13)$$

Note that in these equations, the starting time (t = 0) corresponds to the moment when the pores in the BL were entirely filled, which occurred at approximately 15 min in *Figure 3.7-c*.

3.7Supplementary results

Cluster features and effective cluster interactions in fitted cluster expansions: *Figure SI-3.1* shows the formation energy of structures used in fitting the cluster expansion (CE), computed with only the density functional theory(DFT) electronic energy. *Figure SI 3.1-b, d* show effective interactions (ECIs) of cluster features in BCC, FCC, and γ models. Table-S3.1, S3.2 and S3.3 provide detailed information about cluster shapes, ECI values and the sub- lattices involved clusters in BCC, FCC and γ CE models. As required by the indicator basis, only Li-Li interactions are included.

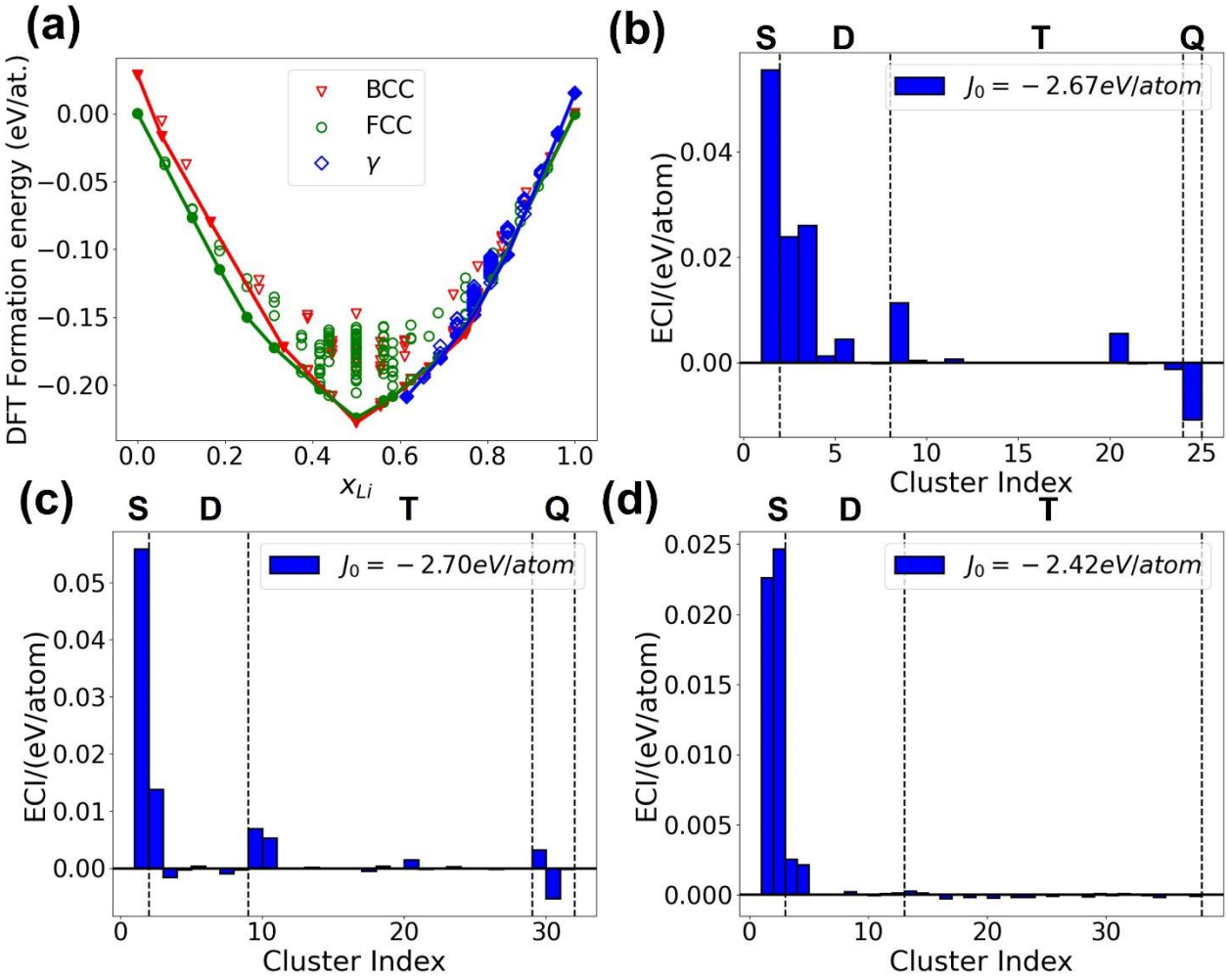

Figure SI-3. 1. (a) Formation energy of structures used to fit CEs (DFT electronic energy only). (b)–(d) The ECIs in the (b) BCC, (c) FCC, (d) γ-Cu_5Zn_8 prototype cluster expansions. The symbols S, D, T, and Q represent point, pair, triplet and quadruplet clusters, respectively. The zero-point terms (i.e. , the intercept) are shown in the figure legends.

Table SI-3. 1. Detailed information of clusters in BCC cluster expansion. The shape of a cluster is expressed as the cluster diameter(the longest distance between sites), the second longest distance between sites, and the second longest distance between sites

ID	Degree	Cluster diameter/Å	2nd longest/Å	3rd longest/Å	ECI [eV/at.]
0	0	N/A	N/A	N/A	-2.67403
1	1	N/A	N/A	N/A	0.055554
2	2	3.0311	N/A	N/A	0.023845
3	2	3.5	N/A	N/A	0.025967
4	2	4.9497	N/A	N/A	0.001304
5	2	5.8041	N/A	N/A	0.0045
6	2	6.0622	N/A	N/A	0
7	2	7.6281	N/A	N/A	-0.00013
8	3	3.5	3.0311	3.0311	0.011386
9	3	4.9497	3.0311	3.0311	0.000451
10	3	4.9497	3.5	3.5	0
11	3	4.9497	4.9497	4.9497	0.000667
12	3	5.8041	4.9497	3.0311	0
13	3	5.8041	3.5	3.0311	0
14	3	5.8041	5.8041	3.5	0
15	3	5.8041	5.8041	4.9497	0
16	3	5.8041	5.8041	4.9497	0
17	3	6.0622	5.8041	3.0311	0
18	3	6.0622	4.9497	3.5	0
19	3	6.0622	5.8041	5.8041	0
20	3	6.0622	3.0311	3.0311	0.005519
21	3	7	4.9497	4.9497	-0.00041
22	3	7	6.0622	6.0622	0
23	3	7	3.5	3.5	-0.00126
24	4	3.5	3.5	3.0311	-0.01079

Table SI-3. 2. Detailed information of clusters in FCC cluster expansion. The shape of a cluster is expressed as the cluster diameter(the longest distance between sites), the second longest distance between sites, and the second longest distance between sites

ID	Degree	Cluster diameter/Å	2nd longest/Å	3rd longest/Å	ECI(eV/at.)
0	0	N/A	N/A	N/A	-2.70465222
1	1	N/A	N/A	N/A	0.05589891
2	3	3.0193	N/A	N/A	0.01384766
3	2	4.2700	N/A	N/A	-0.00157443
4	2	5.2297	N/A	N/A	-0.00027392
5	2	6.0387	N/A	N/A	0.00036392
6	3	6.7515	N/A	N/A	0.00000000
7	3	7.3959	N/A	N/A	-0.00088606
8	4	7.9848	N/A	N/A	-0.00030065
9	3	3.0193	3.0193	3.0193	0.00694888
10	3	4.2700	3.0193	3.0193	0.00525269
11	3	5.2297	5.2297	3.0193	0.00000000
12	3	5.2297	5.2297	3.0193	0.00000000
13	3	5.2297	4.2700	3.0193	0.00022367
14	3	5.2297	5.2297	4.2700	0.00000000
15	3	5.2297	5.2297	5.2297	0.00000000
16	3	6.0387	5.2297	3.0193	0.00000000
17	3	6.0387	4.2700	4.2700	-0.00044292
18	3	6.0387	5.2297	5.2297	0.00036811
19	3	6.0387	6.0387	6.0387	0.00000000
20	3	6.0387	3.0193	3.0193	0.00145949
21	3	6.7515	5.2297	3.0193	-0.00011005
22	3	6.7515	5.2297	5.2297	0.00000000
23	3	6.7515	6.0387	5.2297	0.00028342
24	3	6.7515	6.0387	3.0193	0.00000000
25	3	6.7515	4.2700	3.0193	0.00000000
26	3	6.7515	6.7515	3.0193	-0.00019367
27	3	6.7515	6.7515	4.2700	0.00000000
28	4	6.7515	6.7515	6.0387	0.00000000
29	4	3.0193	3.0193	3.0193	0.00317817
30	4	4.2700	3.0193	3.0193	-0.00525771
31	4	4.2700	4.2700	3.0193	-0.00017985

Table SI-3. 3. Detailed information of clusters in γ cluster expansion. The shape of a cluster is expressed as the cluster diameter(the longest distance between sites), the second longest distance between sites, and the second longest distance between sites. Sub-lattice of cluster sites can be either B(OT), or C(OH)

ID	Degree	Cluster Diameter/Å	2nd longest/Å	3rd longest/Å	ECI(eV/at.)	Sub-lattices
0	0	N/A	N/A	N/A	-2.42093490	N/A
1	1	N/A	N/A	N/A	0.02259629	C
2	1	N/A	N/A	N/A	0.02467135	B
3	2	2.8199	N/A	N/A	0.00257291	C, C
4	2	2.9188	N/A	N/A	0.00215172	B, C
5	2	4.4645	N/A	N/A	0.00000000	B, C
6	2	4.6837	N/A	N/A	0.00000000	B, B
7	2	4.8056	N/A	N/A	0.00000000	C, C
8	2	5.1280	N/A	N/A	0.00023084	B, C
9	2	5.2051	N/A	N/A	0.00003439	B, C
10	2	5.2530	N/A	N/A	-0.00000929	B, B
11	2	5.4103	N/A	N/A	0.00009547	B, C
12	2	7.0843	N/A	N/A	0.00016005	C, C
13	3	4.6837	2.9188	2.9188	0.00027854	B, B, C
14	3	4.6837	4.6837	4.6837	0.00016876	B, B, B
15	3	4.8056	2.9188	2.9188	-0.00000001	B, C, C
16	3	4.8056	4.4645	4.4645	-0.00023316	B, C, C
17	3	4.8056	4.8056	4.8056	0.00003828	C, C, C
18	3	4.8056	4.8056	4.8056	-0.00016807	C, C, C
19	3	5.1280	2.9188	2.8199	0.00000001	B, C, C
20	3	5.1280	5.1280	4.6837	-0.00021537	B, B, C
21	3	5.2051	5.2051	2.8199	0.00000000	C, C, C
22	3	5.2051	4.4645	2.9188	-0.00013816	B, C, C
23	3	5.2051	5.1280	4.4645	-0.00013765	B, C, C
24	3	5.2051	5.2051	4.8056	0.00005190	C, C, C
25	3	5.2051	5.2051	4.8056	-0.00007824	C, C, C
26	3	5.2530	4.4645	2.9188	0.00000000	B, B, C
27	3	5.2530	5.128	4.4645	0.00000000	B, B, C
28	3	5.2530	5.2530	4.6837	-0.00010878	B, B, B
29	3	5.4103	5.2051	2.9188	0.00012772	B, C, C
30	3	5.4103	5.2530	5.1280	-0.00000099	B, B, C
31	3	5.4103	5.2051	5.1280	0.00010346	B, C, C
32	3	5.4103	4.4645	2.8199	0.00000001	B, C, C
33	3	5.4103	5.2530	2.9188	-0.00000129	B, B, C
34	3	5.5702	4.6837	4.8056	-0.00015053	B, B, C
35	3	5.5702	4.8056	2.9188	0.00000000	B, C, C
36	3	5.5702	5.5702	4.8056	-0.00000002	B, C, C
37	3	6.7961	4.8056	4.8056	-0.00005143	C, C, C

Ground-state structures computed with vibration: *Figure SI-3.2* shows intermediate composition ground-state structures beyond the endpoint structures used in the phonon calculations. *Figure SI-3.3* shows the vibrational free energy contribution in each phase as an interpolated function of x_{Li} at T=300 K .

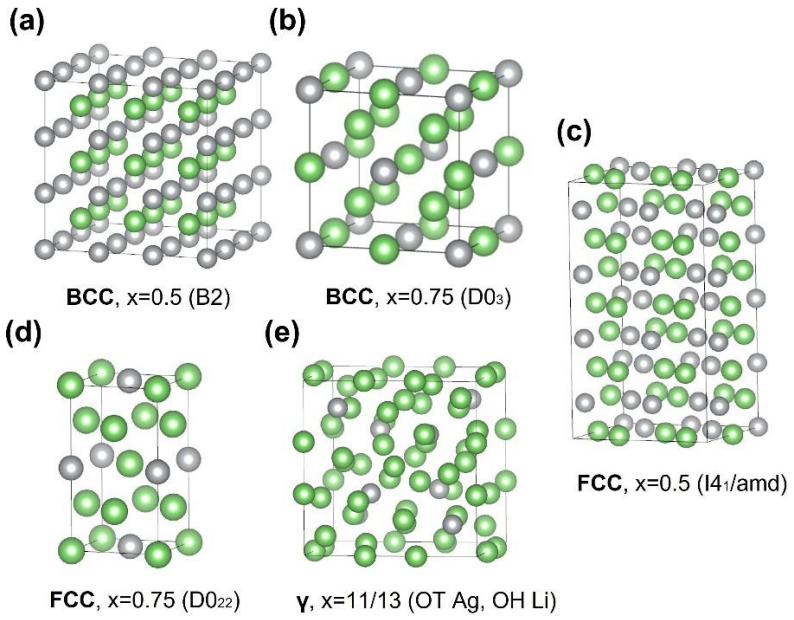

Figure SI-3. 2. Intermediate ground-state structures are used to calculate vibrational free energy. (a) BCC β-AgLi structure at x=0.5 in B2(CsCl-like) ordering; (b) BCC structure at x=0.75 with $D0_3$(BiF_3- like) ordering; (c) The FCC $I4_1$/amd structure at x=0.5; (d) FCC $AgLi_3$ structure in $D0_{22}$ ordering at x=0.75; (e) γ-brass structure with all B(OT) sites occupied by Ag and all other sites occupied by Li at x=11/13.

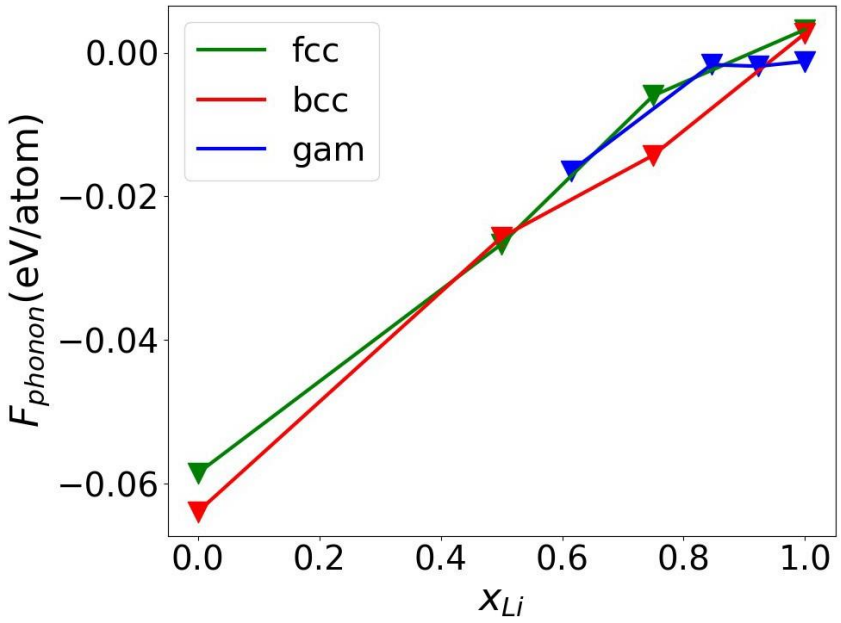

Figure SI-3. 3. Vibrational free energy of BCC, FCC and γ-brass configurations interpolated as functions of Li content (x_{Li}) at T=300 K.

Structural relaxation from Fe_4Zn_9 γ-BRASS to the Cu_5Zn_8 prototype: *Figure SI-3.4* shows the relaxation of the hypothetical Ag–Li γ-brass structure in Fe_4Zn_9 ordering structurally to Cu_5Zn_8 ordering during DFT calculation. Neighboring Ag atoms on IT sites (i.e. , A sites) in the Fe_4Zn_9 ordered structure repel each other and move away to OT sites (i.e. , B sites), while Li atoms originally on OT sites move inward and take over IT sites, resulting in the Cu5Zn8 ordering.

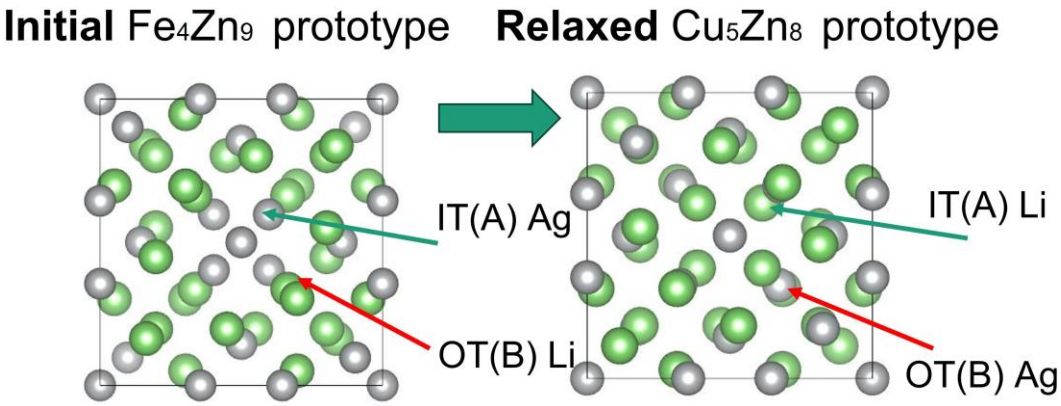

Figure SI-3. 4. Hypothetical Ag–Li γ-brass structure in Fe_4Zn_9 ordering structurally relaxes to Cu_5Zn_8 ordering. Ag atoms originally on IT(A) sites move away to OT(B) sites, and Li atoms on OT(B) sites move inward to IT(A) sites.

Configurational and vibrational contributions to BCC stability over γ: In the main text, BCC configurations appear to be stabilized over γ-brass with increasing temperature. *Figure SI-3.5* shows the total free energy difference between BCC and γ (F (BCC) − F (γ)) at increasing temperatures with (blue) and without (green) phonon correction. When xLi = 8/13, although the BCC phase can be stabilized at increasing temperatures by merely configurational entropy (green), including the vibrational entropy (blue) can significantly decrease the transformation temperature from γ to BCC. At x_{Li} = 0.75, γ-brass shows higher configurational entropy as F (BCC) − F (γ) increases to 0 as the temperature increases without phonon correction; however, including vibrational entropy reverses this trend and stabilizes BCC. Overall, including vibrational entropy corrections in free energy is important in predicting BCC and γ-brass stability in the Ag–Li system.

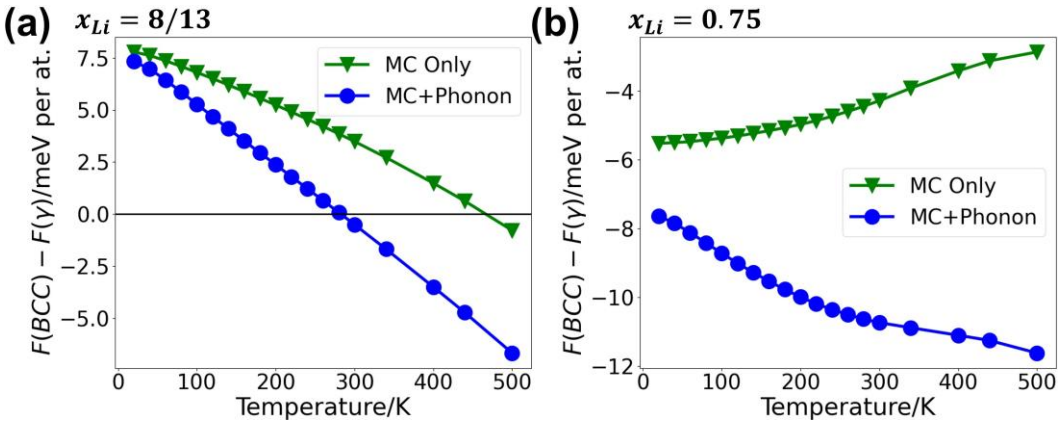

Figure SI-3. 5. Total free energy difference between BCC and γ (F (BCC) − F (γ)) at increasing temperatures with (blue) and without (green) phonon correction, at (a)x_{Li} = 8/13 and (b)x_{Li} = 0.75.

γ_2 Phase as a *D*0_3BBC $AgLi_3$ structure: *Figure SI-3.6* presents the results of semi-grand canonical MC simulations on the BCC lattice. Composition plateaus can be found corresponding to the D03-$AgLi_3$ structure at x_{Li} = 0.75 when T<=300 K, suggesting D03-$AgLi_3$ as a new phase to be formed out of disordered BCC solid solution. The simulated XRD patterns in *Figure SI-3.7* suggest a large portion of intense peaks in BCC D03-AgLi3 and γ-brass structures are close in their positions and can confusingly overlap. When the experimental resolution is low and other impurity phases are present, BCC D03-$AgLi_3$ may not be clearly distinguished from γ-brass.

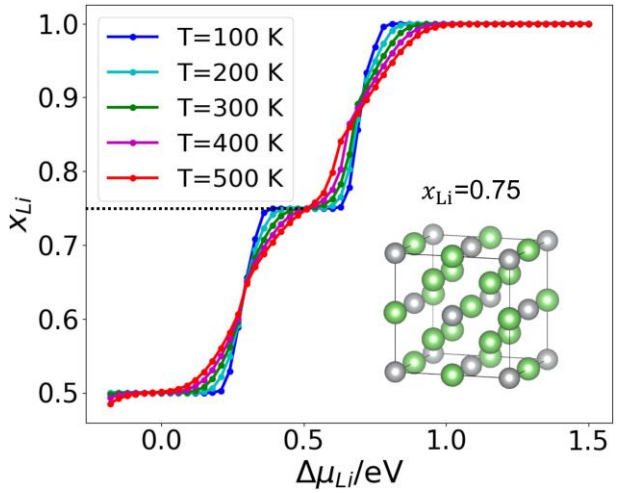

Figure SI-3. 6. Li content (x_{Li}) as a function of Li chemical potential ($\Delta\mu_{Li}$) at varied temperatures, plotted from MC simulation results in a semi-grand ensemble on BCC lattice. The $D0_3$ structure corresponding to the plateau at x_{Li} = 0.75 is provided in the figure.

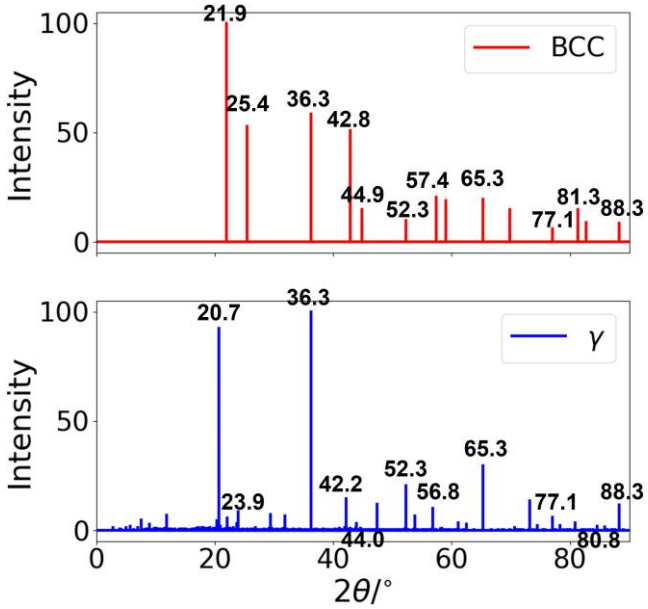

Figure SI-3. 7. Simulated X-ray powder diffraction (XRD) patterns computed from the BCC (red) and γ-brass (blue) snapshot structures taken from MC simulations at x_{Li} = 0.75, T=300 K. Possibly overlapping peaks are marked with their corresponding 2θ values in both phases.

Continuum simulation parameters: Parameter values used in our work are presented in Table S3.4. Corresponding experimental references to these parameter values are listed in the last column of the table.

Table SI-3. 4. Parameter values used in our continuum simulations and their corresponding experimental references.

Name	Symbol	Unit	Value	Reference
Li-ion current density	i_{Li}	$mA/cm2$		
Electron current density	i_{e-}	$mA/cm2$		
Applied current density (external)	i_t	mA/cm^2	0.68	
Li-ion conductivity in the BL	σ_{Li^+}	mS/cm	[0.05~5]	[81]
Electron conductivity in the BL	σ_{e-}	mS/cm	10^4	[69]
Electrochemical potential of Li^+ in the BL	$\bar{\mu}_{Li^+}$	eV		
Electrochemical potential of e^- in the BL	$\bar{\mu}_{e-}$	eV		
Faraday constant	F	$A \cdot s/mol$	96485	
Exchange current density at the BL/SE interface	i_{ex}^{SE}	mA/cm^2	1.3	[78]
Exchange current density at the Ag-Li surface	i_{ex}^{Ag}	$mA/cm2$	0.65	[79]
Anodic reaction coefficient	a_c	N/A	0.5	[29]
Cathodic reaction coefficient	a_c	N/A	0.5	[29]
Ideal gas constant	R	$J/(mol \cdot K)$	8.31	
Temperature	T	K	298	
Interface overpotential	η	eV		
Hydrostatic pressure developed in the BL	P	MPa		
Bulk modulus of Li metal	K	GPa	11	[83]
Molar volume of Li metal	$\bar{V}_{Li}$	cm^3/mol	12.97	
BL thickness	H	μm	10	
Electronic area specific resistance (ASR)	R_e	$\mu m\ \Omega \cdot cm^2$	Varied	

3.8 Acknowledgements

This work was funded by the U.S. Department of Energy (DOE), Office of Science, Office of Basic Energy Sciences, Materials Sciences and Engineering Division under Contract No. DE-AC0205CH11231 (Materials Project program, KC23MP), and the Assistant Secretary for Energy Efficiency and Renewable Energy (EERE), Vehicle Technologies Office, under the Advanced Battery Materials Research (BMR) Program of the U.S. Department of Energy under Contract No. DE-AC02-05CH11231. The work was also supported with the computational resources provided by the National Energy Research Scientific Computing Center (NERSC), a U.S. Department of Energy Office of Science User Facility located at Lawrence Berkeley National Laboratory, the computational resources sponsored by the DOE Office of Energy Efficiency and Renewable Energy (EERE) and located at the National Renewable Energy Laboratory(NREL), and the Lawrencium computational cluster resource provided by the IT Division at Lawrence Berkeley National Laboratory. The authors thank Dr. Nathalie Dupin for helpful discussions on CALPHAD models. The authors also gratefully acknowledge Dr. Srinath Chakravarthy from Factorial Energy, Dr. Eric Yang Wang from Samsung Advanced Institute of Technology, and Dr. Lincoln Miara from Pure Lithium, for insightful discussions on the modeling and experiments of the anode-free solid-state system.

Chapter 4: Mitigating battery cell failure: Role of Ag-nanoparticle fillers in solid electrolyte dendrite suppression

4.1 Foreword

The work presented in this chapter is based, often verbatim, on the following publication: ***Diallo, M.S***.; Ogunfunmi, T.; Yang, X.C.; Oyakhire, S.T.; Avvaru, V.S.; Scott, M.C.; Tu, Q.H.; Ceder, G., "Mitigating battery cell failure: The role of Ag nanoparticle-fillers in Solid Electrolyte dendrite Suppression." *In preparation*

4.2 Abstract

The development of solid-state batteries (SSBs) with lithium (Li) metal anodes holds significant promises for enhancing energy density and safety in next-generation energy storage systems. However, the commercialization of these batteries is hindered by challenges related to Li dendrite formation, which can lead to short circuits and battery failure. In this study, we investigate the role of silver (Ag) nanoparticles in suppressing dendrite propagation within solid electrolytes (SEs). Our results demonstrate that Ag nanoparticles effectively mitigate two key failure mechanisms: (1) dendrite growth within porous networks at low current densities and (2) stress intensification-induced SE fracture at higher current densities (12.8mA/cm^2). Ex-situ characterization through Focused-ion beam – scanning electron microscopy (FIB–SEM) and energy dispersive X-ray spectroscopy (EDS), reveal that Ag nanoparticles migrate alongside advancing Li dendrites, promoting homogeneous dendrite growth and reducing the likelihood of localized stress concentrations. Additionally, the incorporation of Ag nanoparticles facilitates a more uniform distribution of Li, which could potentially enable higher charging rates in SSBs. This study provides a new perspective on Li dendrite suppression and opens new opportunities for enhancing the performance and safety of solid-state batteries.

4.3Introduction

The commercialization of SSBs is highly anticipated due to the replacement of the flammable liquid electrolytes in Li-ion batteries with SEs. In addition to enhancing safety by reducing the risk of leakage and thermal runaway, SSBs also enable the use of Li-metal anodes and high-voltage cathodes. The remarkable specific capacity (3860 mAh/g) and low redox potential (−3.04 V vs. SHE) of Li-metal anodes make them a prime candidate for next-generation high-energy-density batteries,[18–21] particularly for applications in electric vehicles and portable electronics.[5] SSBs using Li-metal anodes are thus positioned as a key technology for the future of energy storage.[17,173]

However, the current prospects of Li-metal SSBs remain limited due to failures during the electrochemical process. Li is known to deposit unevenly[28], leading to dendrite-promotion phenomena including current focusing, surface-crack proliferation[174], and Li-metal filament infiltration.[60,74,75,83,175] Several approaches have been explored in the literature to understand the initiation, propagation, and suppression of dendrites, highlighting the role that the microstructure plays in the failure of SSBs.[23]

The use of tri-layer SEs has been shown to improve cell survivability by enabling crack-blunting[176] or crack-deflection[177] mechanisms that actively stop the spread of dendrites. However, these techniques do not inhibit other failure mechanisms such as those stemming from chemical reactions and electronic conductivity, which are known to affect the chemical stability of the cell. The introduction of carbon-metal interlayers in the design space of SSBs has further enhanced the survivability of SSBs by enabling homogeneous Li plating and providing physical separation between the anode and electrolyte to avoid chemical reactions[33]. Although many reports highlight the benefits of carbon-metal interlayers, several challenges must be addressed before their commercialization. Capacity retention requires minimization of the irreversible reaction between Li and the active components in the interlayer. Although the metal component homogenizes the current[40], strong adhesion is still needed to preserve the contact between the interlayer and current collector. More importantly, to enable high-rate capability, Li transport in the interlayer is crucial to avoid Li plating at the interlayer and SE interface, which ultimately lead to dendrite growth.[34–36,41]

In our recent study, which constitutes a prequel to this work, the impact of the SE pellet density on SSB failure was highlighted, revealing two distinct regimes: a pore-percolating regime (SE pellet density < 95%) and a non-percolating regime (SE pellet density > 95%). In the percolating regime, failure occurs faster due to the presence of small, connected pores, whereas in the non-percolating regime, the cells do not short-circuit. These findings emphasize the importance of controlling the microstructure of SE pellets to mitigate dendrite formation.[178] In the current investigation, we aim to build upon the above-mentioned findings by exploring the addition of Ag nanoparticle fillers to the SE and the role of their interaction with Li during electrochemical cycling in impeding dendrite growth. We find that the short-circuiting behavior of cells in the pore-

percolating regime is suppressed and high-current-density cycling is achieved. To explain the underlying mechanisms, the microstructure of post-mortem pellets is analyzed using SEM and EDS to showcase the role of Ag particles in electrochemical cycling.

4.4Results

Synthesis and characterization of Ag-mixed solid electrolytes

The SE in the SSB cells was synthesized by dispersing Ag nanoparticles in amorphous $75Li_2S{-}25P_2S_5$ (LPS). The mixing was performed using a vertical shaker to ensure uniform dispersion of Ag nanoparticles in the SE. The mixed LPS-Ag SE was then pressed at 300 MPa, which corresponds to the pore-percolating regime[178], to form a dense SE layer before assembling the cell.

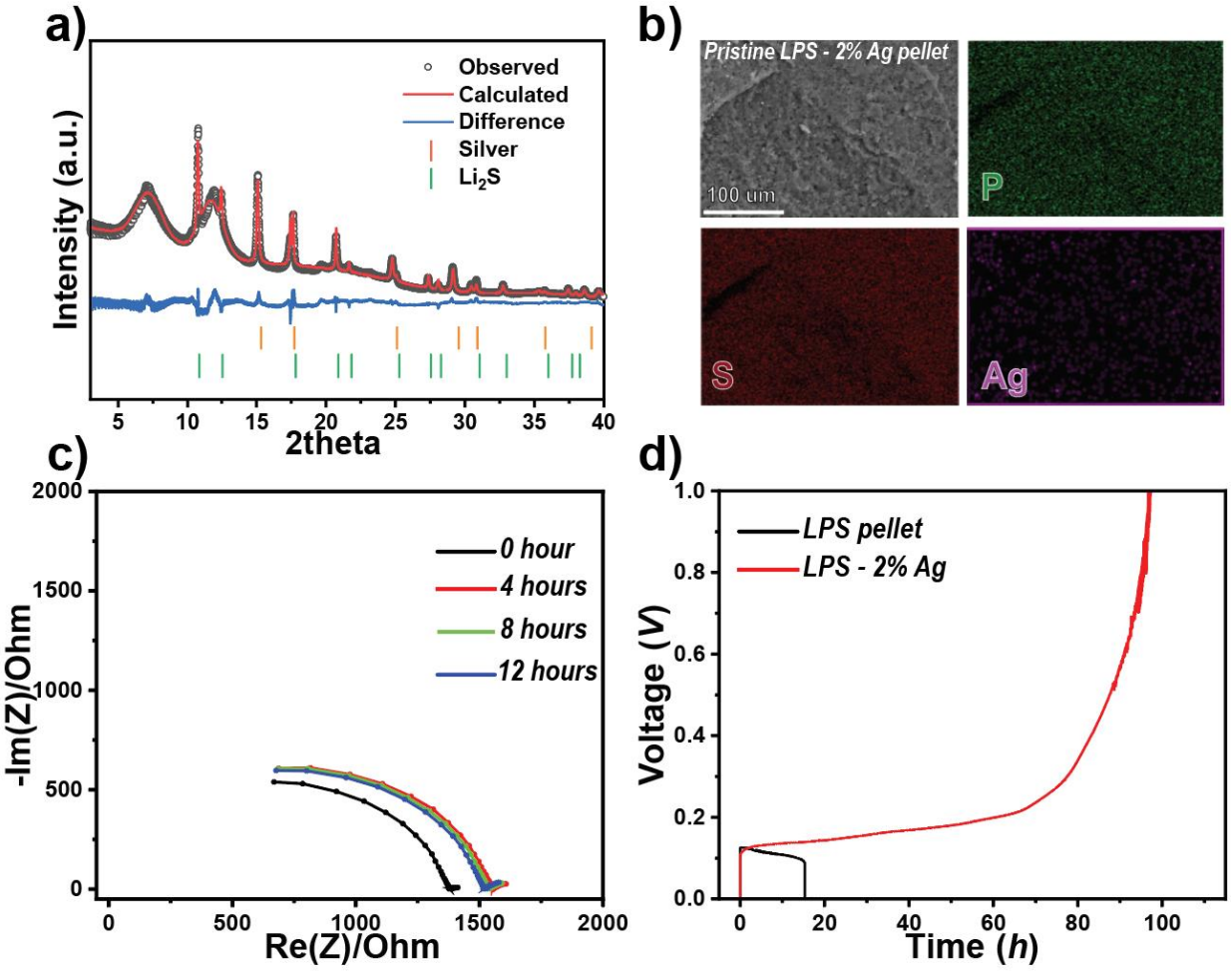

Figure 4. 1. Comprehensive analysis of LPS and LPS with Ag nanoparticles dispersed in the solid electrolyte. 1a) Synchrotron XRD pattern of LPS with distributed Ag nanoparticles. 1b) SEM/EDS images of pellet surface. 1c) Nyquist plots of symmetric cell with mixed SE at various rest times. 1d) Voltage profiles for LPS and LPS + 2% Ag symmetric cells charged at 0.2 mA/cm^2.

To ensure that the Ag nanoparticles did not react with LPS and were well dispersed, synchrotron X-ray diffraction (XRD) and SEM/EDS elemental mapping were performed on the as-prepared mixed SE pressed pellet. Electrochemical impedance spectroscopy (EIS) was used to monitor the impedance of the cell before conducting electrochemical (EC) charging experiments.

Figure 4.1-a presents a synchrotron XRD pattern of the mixed LPS-Ag SE powder, indicating that Ag and Li_2S were the main compounds identified in the SE. The broad peaks are indicative of the amorphous LPS with no evidence of derived Ag phases, confirming that Ag remains unreacted when mixed with LPS. *Figure 4.1-b* presents the EDS elemental mapping of phosphorus (P), sulfur (S), and Ag on a cleaved surface of the SE pellet, showing that the Ag particles are homogeneously distributed within the LPS matrix. *Figure 4.1-c* displays the EIS spectrum of the assembled cell during the resting period, defined as the time when the cell is idle between cell assembly and EC. The impedance increased from ~1400 to 1500 Ω within the first 4 h of cell assembly and then stabilized due to the formation of the SEI layer, consistent with our past observations.[178] *Figure 4.1-d* presents the EC voltage profile of two symmetric cells with the configuration stainless steel (SUS) | Li | SE | Li | SUS, where the SEs are LPS and LPS + 2% Ag. These cells were charged at 0.2 mA/cm² until either failure or Li-source depletion occurred. Failure occurs when the voltage drops to zero (short-circuit), whereas Li-source depletion is indicated by a rapid increase in the cutoff voltage. The cell with bare LPS as the SE short-circuited after 18 h, consistent with our previous findings.[178] In contrast, Li-source depletion of the mixed SE cell occurred after 80 h. At a constant current density of 0.2 mA/cm², this result corresponds to 80 µm of Li plated. This significant difference indicates that the presence of Ag nanoparticles effectively suppresses the short-circuiting effects of pore percolation. Various Ag concentrations were also investigated, as shown in *Figure SI-4.2* (Supplementary Information). The results indicate Li-source depletion behavior at Ag concentrations up to 10%.

Post-mortem analysis of charged solid-state electrolyte pellets

To elucidate the role of Ag nanoparticles in suppressing failure via pore percolation, post-mortem characterization was conducted using optical microscopy (OM) and SEM/EDS to examine the polished surface of charged pellets. Half cells with the configuration SUS | Li_{source} | LPS + 2% Ag | SUS were prepared and charged at 0.2 mA/cm² to different states of charge: 5, 10, 20, and 40 h, as shown in *Figure SI-4.3*. After EC charging, the cells were disassembled, and the charged pellets were recovered and sealed in epoxy to preserve their structural integrity during polishing. The pellets charged for 5, 10, and 20 h were polished in a top-down fashion, starting on the plated Li side, to reveal the interaction between the plated Li and the mixed SE, and the pellet charged for 40 h was polished along the cross-section.

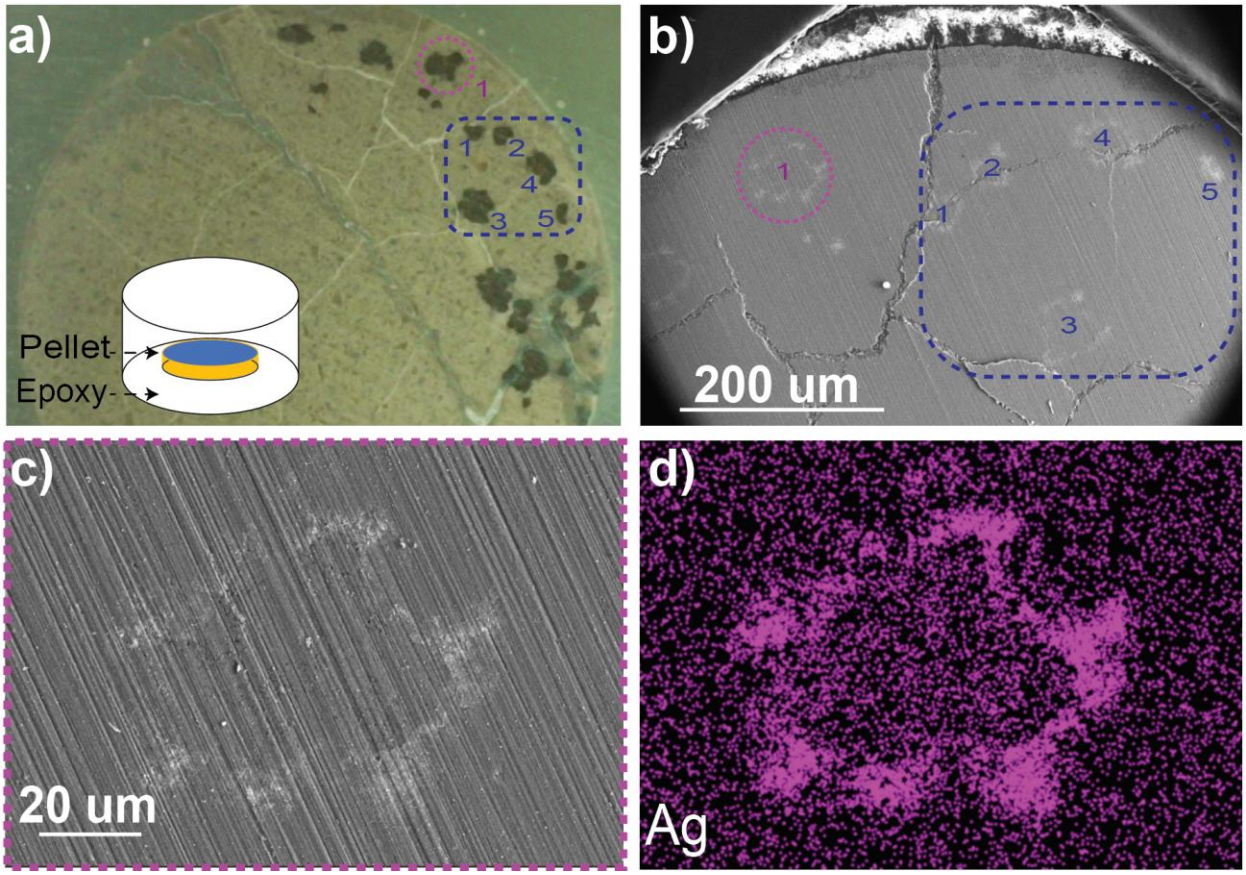

Figure 4. 2. SEM/EDS characterization of post-charged LPS pellet with Ag nanoparticles. 2a) Top-down OM image of polished LPS+2%Ag pellet after charge. 2b) Backscattered-electron SEM image of polished pellet surface. 2c–d) SEM/EDS elemental mapping of Ag on polished SE pellet surface.

Figure 4.2-a shows the surface of a cell that was charged for 20 h, recovered, and then sealed in epoxy and polished. The accumulated dark spots on the polished surface are identified as regions where Li reacted with LPS, which is consistent with reported Li dendrites in garnets and sulfides[53,179]. Multiple OM images were acquired at different states of charge and at different steps during the polishing to monitor the evolution of the Li–SE interaction. The results are presented in *Figure SI-4.4, SI-4.5,* and *4.6*. *Figure 4.2-b* presents a low-magnification SEM image of the same region shown in *Figure 4.2-a*. The pink circle and blue square indicate corresponding regions in both imaging modes, ensuring that the same areas are consistently represented. The presence of heavier elements around the dark spots is revealed, as evidenced by the bright contrast in the SEM image. Further analysis of the pink-circled region is presented in *Figure 4.2-c* and *4.2-d*. The EDS mapping reveals that Ag is concentrated around the dark spots, correlating with the distribution of advancing Li dendrite clusters within the SE. Notably, the shape of the Ag clusters differs at various depths within the SE. For example, in the blue rectangle region, Ag at position #3 (*Figure 4.2-b*) is concentrated around the edges, whereas Ag at position #5 is smaller and more uniform, suggesting different stages in the evolution of advancing Li filaments. This behavior is also highlighted in *Figure SI-4.5*, which shows the evolution of the surface morphology of the cell

presented in *Figure 4.2-b*. These observations hint at a significant divergence from conventional Li-dendrite evolution in SEs, which typically involves a localized dendrite path rather than spread-out propagation.[175,179,180]

***Ex-situ* cross-sectional SEM/EDS and FIB/SEM tomography of charged solid-state cells**

Further cross-sectional characterization was conducted to better understand the suppression mechanism of the Ag nanoparticles. The half-cell charged for 40 h under a constant current density of 0.2 mA/cm^2 was sealed in epoxy and polished for cross-sectional SEM/EDS analysis.

Figure 4.3-a and *4.3-b* present the cross-sectional SEM/EDS results of the charged cell after brief oxygen exposure. A concentrated Ag band deep within the SE is observed, with a more concentrated oxygen spectrum between the plated Li side and Ag front. Oxygen exposure was conducted to highlight areas where Li infiltrated the SE. Because the pellet cross-section was uniformly exposed to oxygen, regions of the SE showing higher oxygen concentrations indicate the presence of Li. In this case, Li penetrated the pellet uniformly, contrasting with the wedge-like cracking typically observed in most SSB failures.[174,177]

Subsequent EDS maps, presented in *Figure 4.3-c* and *4.3-d*, highlight the presence of a Ag front, identified by the region between the pink dashes, through the superimposition of SEM and EDS images. Several line scans track the Ag concentration across the SE cross-section, with the highest Ag counts observed at the Ag band. The Ag concentration is notably higher in the Li-infiltrated region compared to in the unaffected SE beyond the Ag front. These findings suggest a mechanism that allows Ag to agglomerate along with the advancing dendrite front.

FIB milling of the Ag front was used to obtain a cross-sectional view of the Ag band. *Figure 4.3-e* reveals the dendrite-like structures within the Ag band, and *Figure 4.3-f* confirms the high concentration of Ag at the dendrites. This observation further confirms the coupling between Li dendrite propagation and Ag aggregation.

FIB/SEM tomography was conducted to investigate the microstructural evolution of the SE. Consistent with the observations in *Figure 4.3-e*, the cross-sectional images in *Figures 4.4-a* and *4.4-b* reveal highly branched dendrites distributed throughout the Ag front. To obtain deeper insight into the 3D structure, thin slices of 20 nm were sequentially cut across the cross-section using FIB, reaching a total depth of 2 µm.[181] After each cut, backscattered-electron imaging was used to capture the 2D morphological evolution of the cross-section. Image processing was subsequently performed on the selected regions, as shown in *Figure 4.4-b*, which involved segmentation to isolate the dendrite structures within the 2D image stack. This process enabled the 3D reconstruction presented in *Figure 4.4-d*, highlighting the in-depth evolution of the dendrites. The dendritic structures exhibit a significant degree of connectivity, with tomography revealing that the Ag band possesses a highly three-dimensional microstructure. This finding suggests that Ag must move alongside Li to enable such structural flexibility, offering valuable insight into the evolution of Li filaments and their interaction with Ag nanoparticles.

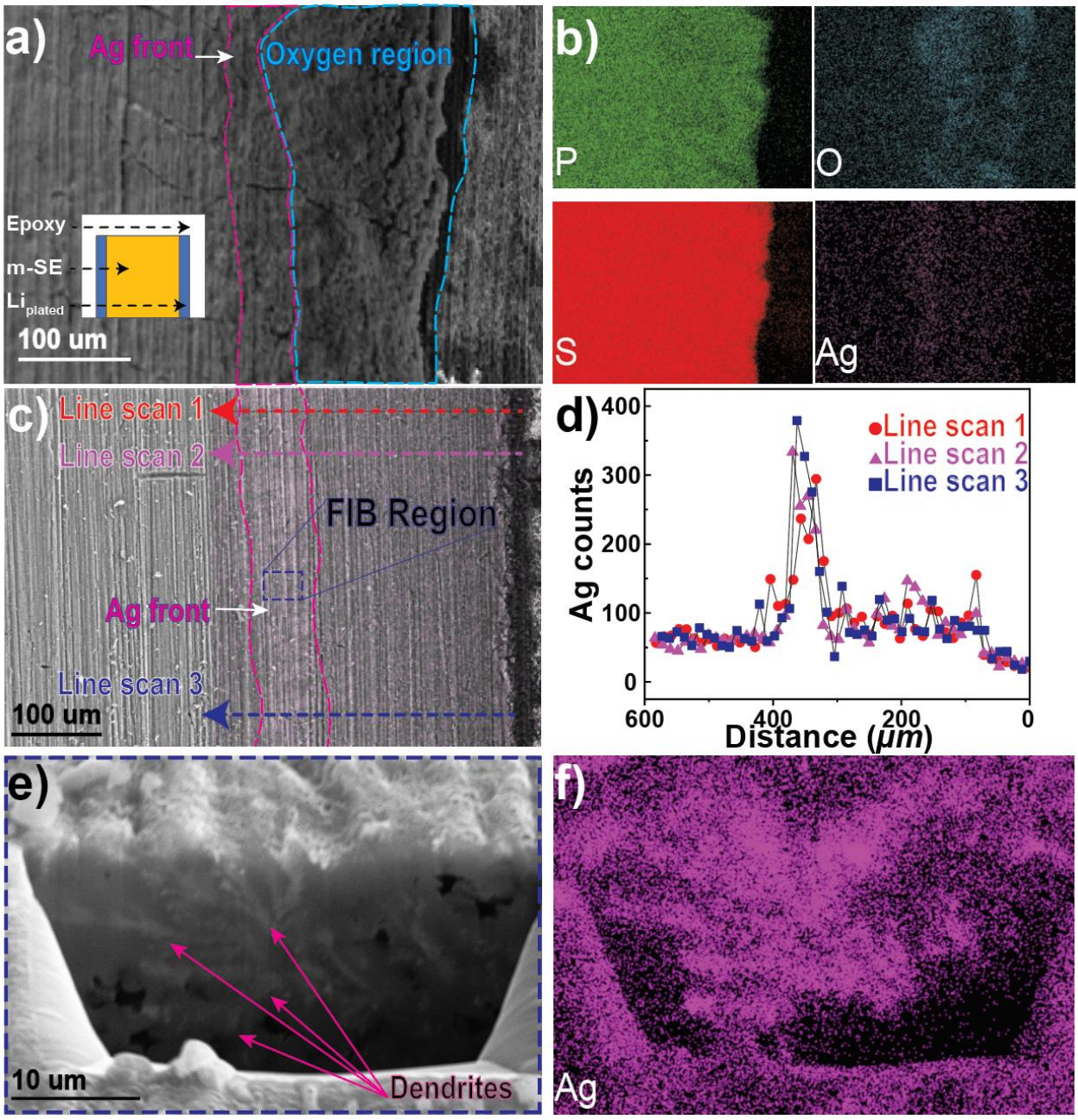

Figure 4. 3. Cross-sectional SEM/EDS characterization of post-charged LPS pellet with Ag nanoparticles. 3a–b) Cross-sectional SEM/EDS images of charged pellet after oxygen exposure. 3c) Cross-sectional SEM/EDS elemental mapping of Ag in polished pellet. 3d) Ag counts with respect to distance from the Li-plating side. 3e–f) FIB/SEM/EDS images of highlighted Ag band area.

Electrochemical performance of solid-state cells

The electrochemical performance of solid-state cells with mixed SE (m-SE) was systematically evaluated under various configurations and testing conditions. The tested configurations included both symmetric cells SUS | Li | SE | Li |SUS and Li | Li_3N+LiF | SE | Li_3N+LiF | Li. The EC

charging protocols implemented included 1) long-term charging at a fixed current density of 0.2 mA/cm², 2) unidirectional charging with increasing current densities over fixed time intervals, and 3) long-term cycling with increasing current densities. The Li_3N+LiF buffer layer was added to mitigate the effects of chemical reactions and electronic conductivity.[32]

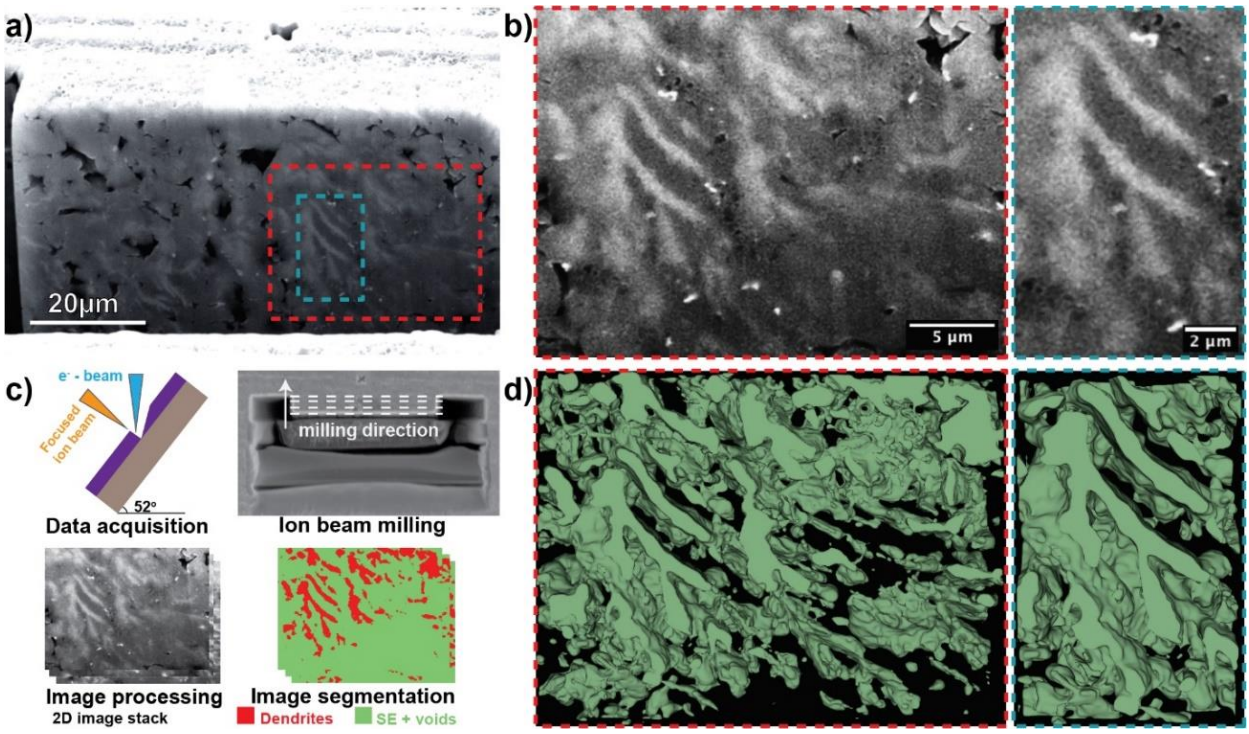

Figure 4. 4. 3D reconstruction from FIB/SEM tomography. 4a) FIB region selected for tomography highlighting the dendrites. 4b) Magnified backscattered-electron SEM image of cross-section, showing the regions targeted for 3D reconstruction. 4c) Workflow for FIB–SEM tomography.[181] 4d) Dendrite 3D reconstruction of selected regions.

Figure 4.5a compares three symmetric cells with similar architectures and testing conditions but different SEs: LPS pressed at 300 MPa, mixed SE (LPS + 2% Ag) pressed at 300 MPa, and mixed SE (LPS + 2%) pressed at 1 GPa. The SEs pressed at 300 MPa were within the pore-percolating regime, where the pores are interconnected, whereas the SEs pressed at 1 GPa were in the non-percolating regime. The cells in the percolating regime exhibited different behaviors: the bare LPS cell short-circuited at 0.4 mA/cm², whereas the mixed SE cell remained stable without short-circuiting, even at 12.4 mA/cm², although some voltage noise was observed at higher current densities. In contrast, the mixed SE in the non-percolating regime short-circuited at 1.6 mA/cm², which is consistent with the behavior of LPSCl in the non-percolating regime. The differing failure behaviors of the cells prepared with mixed SEs suggest distinct failure mechanisms. In the percolating regime, the interconnected pores facilitate Li infiltration, whereas in the non-percolating regime, the isolated pores restrict this infiltration, thereby limiting the interaction between Li and Ag nanoparticles.

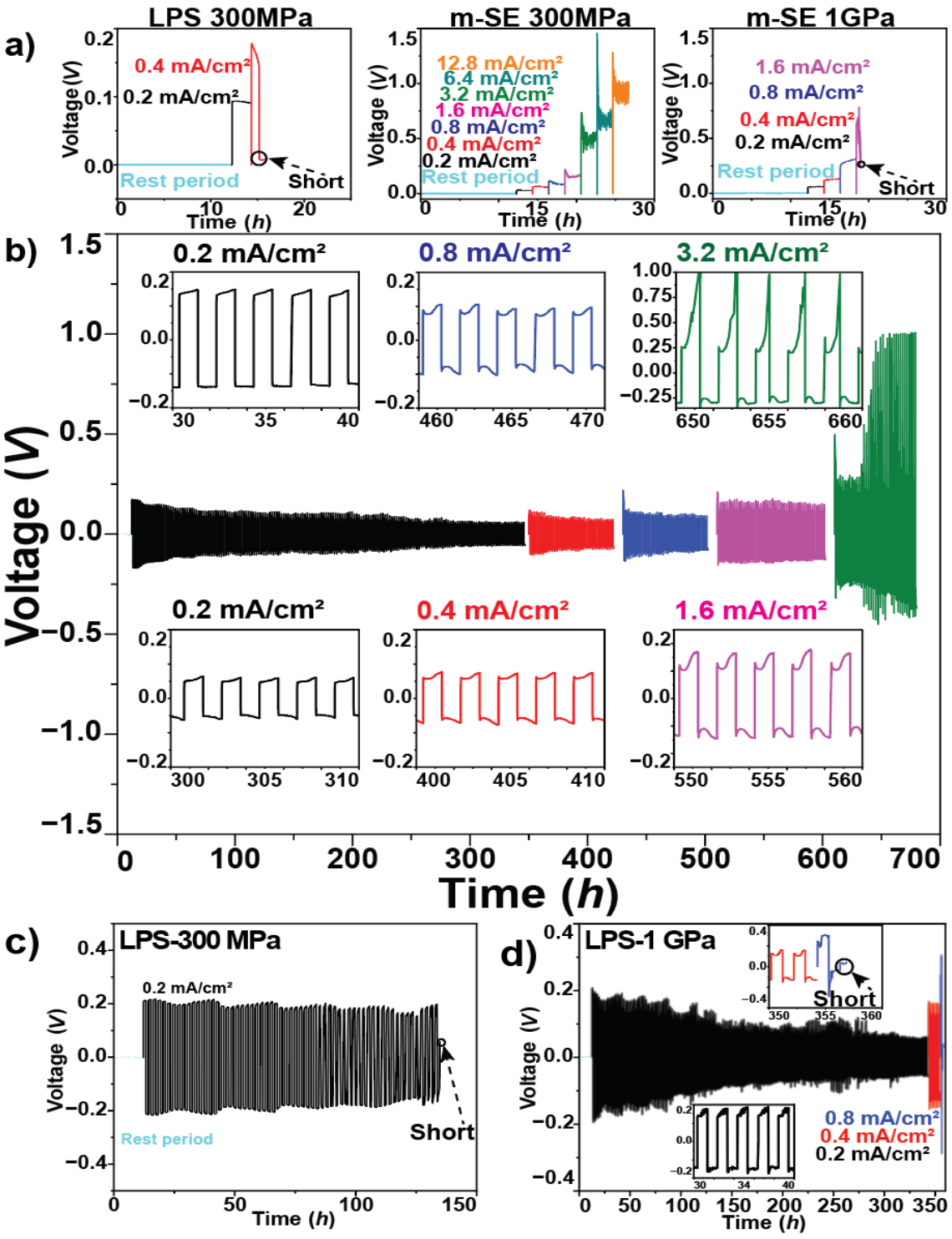

Figure 4. 5. Effect of Ag nanoparticles on electrochemical performance. 5a) Voltage profile comparison of cells with different SEs (300MPa–LPS, 300MPa–LPS+2%Ag, 1GPa–LPS+2%Ag) at increasing current density. 5b) Long-term cycling at increasing current density of (Li|Li_3N+LiF|LPS–10%Ag|Li_3N+LiF|Li). The SE was pressed at 300 MPa. 5c–d) Shorted cells (Li|Li_3N+LiF|LPS|Li_3N+LiF|Li) under long-term cycling testing conditions. SE pressed at 300 MPa and 1 GPa corresponds to the pore-percolating and non-percolating regimes, respectively.

Figure 4.5-b presents the long-term cycling voltage profile of a symmetric cell (Li | Li_3N + LiF | LPS-10% Ag | Li_3N + LiF | Li). The cell was first cycled at 0.2 mA/cm² for 160 cycles to assess the stability. After reaching a stable plating potential, the cell was cycled at increasing current densities for 6 cycles. Stable cycling was maintained up to 3.2 mA/cm², with signs of irreversibility but no short-circuiting. The inset subplots provide a detailed view of the voltage profile at different time intervals, highlighting the stability of the charge/discharge process. In contrast, *Figures 4.5-c* and *4.5-d* depict identical experimental procedures for cells using bare LPS in both percolating (LPS pressed at 300 MPa) and non-percolating (LPS pressed at 1 GPa) regimes. The cell in the percolating regime short-circuited at 0.2 mA/cm² after 67 cycles, whereas the cell in the non-percolating regime short-circuited at 0.8 mA/cm².

4.5 Discussion

Previously, we have demonstrated that at low current densities (i.e., 0.2 mA/cm²), the dominant failure mechanism in SEs involves the growth of Li filaments within the porous networks present in SE pellets densified below 95% (M_1). These Li filaments, if allowed to propagate, can ultimately lead to short-circuiting and rapid capacity degradation in solid-state cells[75]. In contrast, Li depletion is observed in SE pellets densified above 95% due to the absence of pore networks, which prevents Li infiltration. At higher current densities (i.e., > 0.2 mA/cm²), the prevailing failure mechanism shifts to stress intensification, leading to fractures in the SE (M_2), irrespective of the SE pellet microstructure.[178] This stress-induced failure severely compromises the structural integrity of the SE, contributing to overall battery failure.

In this study, we demonstrate that the incorporation of Ag nanoparticles in the SE effectively suppresses both M_1 and M_2 in the pore-percolating regime. The presence of Ag nanoparticles disrupts Li-filament growth by redistributing Li currents, preventing localized current concentration and subsequent dendrite propagation. As highlighted in *Figure 4.1-d*, Ag nanoparticles inhibit M_1, leading to Li-source depletion in solid-state cells within the percolating regime at low current densities. Additionally, as shown in *Figure 4.5-a*, Ag nanoparticles mitigate M_2 by reducing stress concentrations that typically lead to SE fracture at higher current densities. Previous studies have explored various strategies for mitigating dendrite growth and stress-induced fractures; however, the incorporation of Ag nanoparticles provides a novel and effective approach.

Behavior in the pore-percolating regime: Advanced characterization techniques, including FIB–SEM and EDS, alongside oxygen cross-section exposure, provided crucial insight into the behavior of Li infiltration within the SE in the pore-percolating regime. By exposing the cross-section of the charged pellet to oxygen, regions with higher oxygen concentrations were identified, which correspond to areas infiltrated by Li. This technique provides a clear visual contrast, allowing for more precise mapping of the Li distribution within the SE. These methods revealed a homogeneous Li layer deep within the SE, extending from the Li plating side. This discovery strongly suggests that Li is infiltrating the SE through interconnected porous networks, forming a continuous Li layer within the material. The uniform nature of this Li distribution implies that Ag

nanoparticles play a key role in promoting more controlled Li infiltration throughout the SE. In contrast to scenarios where dendrite growth is concentrated in certain regions[50], the presence of Ag nanoparticles ensures a more even spread of Li, likely by redistributing the Li current within the SE and reducing localized dendrite formation, thereby explaining the suppression of M_1 and M_2 in the pore-percolating regime.

Furthermore, EDS elemental mapping of the infiltrated Li revealed a significant presence of Ag, with the highest concentration located at the leading edge of the Li infiltration, forming what is known as the **Ag front**. This front is prominently illustrated in *Figure 4.2* and *Figure 4.3*, where the Ag concentration is demonstrated to be notably higher between the Li plating side and the Ag front compared to regions beyond it. This finding suggests that Ag nanoparticles migrate with the advancing Li-dendrite front. Additionally, FIB analysis revealed that the structure within the Ag front exhibits a classic dendrite morphology[182–185]—observed for the first time in SSBs—characterized by a high concentration of Ag. These dendrites are seen branching and spreading in multiple directions, particularly along the Li stripping direction, further reinforcing the role of Ag in modifying dendrite growth. This behavior suggests that Ag nanoparticles not only redirect the current but also impact the structural evolution of Li filaments within the SE.

Behavior in the non-percolating regime: Although Ag nanoparticles play a critical role in mitigating dendrite propagation in the pore-percolating regime, their effectiveness diminishes significantly in the non-percolating regime. In this regime, SEs are densified above 95%, resulting in the absence of interconnected pore networks. This structural difference fundamentally alters the behavior of Li infiltration and shifts the primary failure mechanism to M_2. Without the porous pathways available in the pore-percolating regime, Li infiltration is limited, and cracks begin to form at the SE–Li interface under high current densities. As demonstrated in previous studies, materials such as LPSCl exhibit wedge-like cracking under current densities above 3 mA/cm², with crack initiation occurring at surface defects. This form of fracture significantly weakens the SE, leading to premature cell failure[70,174,177].

Ag nanoparticles, which previously redistributed Li currents and suppressed dendrite growth in the pore-percolating regime, are ineffective in preventing such cracks. The structural integrity of the SE is compromised by stress intensification, and the Ag particles are unable to alter the progression of these fractures. In contrast to their role in the pore-percolating regime, where they promote a more uniform Li distribution, Ag nanoparticles have no impact on the stress concentration at the SE–Li interface in the non-percolating regime.

Although this point could be viewed as a limitation, it is not considered as one because densification is required to suppress the pore-percolating regime. Extensive studies have also shown that densification improves performance in LPS[52], LPSCl[186], and LLZO[53,55]; however, these materials often face the same challenge of suppressed dendrite growth while remaining vulnerable to fracture due to stress intensification. Our results hint at the prospect of achieving higher performance at lower density, which would offer more manufacturing options for their commercialization.

Mechanistic Insights into Ag Nanoparticles' Role: Understanding the role of Ag nanoparticles in dendrite suppression is critical to understanding our findings. A study on the role of Ag in Ag–C buffer layers previously demonstrated that Ag particles significantly affect current homogenization at the current collector, redirecting Li currents even near defect tips positioned 25-µm away[187]. In the context of SEs, the homogeneous distribution of Ag nanoparticles leads to lithiation upon contact with Li filaments, expanding toward existing defects. This behavior is further supported by our electro-mechanical model (details in the Method section), which quantifies the Li current distribution within the mixed SE, as shown in *Figure 4.6-e*. The model simulates a 2-µm Li filament growing in a pore with a Ag particle positioned midway along its length to examine the current distribution along the filament. *Figure 4.6-f* shows the current density at various positions along the Li filament, comparing the cases where a Ag particle is in contact with the filament and where no Ag particle is present. In the case where no Ag particle is present, the current density is highest at the tip of the Li filament, which explains the continuous growth of a dendrite once it materializes. Based on this result, it is expected that the Li filament in the more connected porous network would grow the fastest and cause short-circuit, consistent with our observations.

In the presence of Ag nanoparticles (blue curve in *Figure 4.6-f*), the current density is highest at the Ag location, even when a Li filament tip is positioned further from the Ag particle. The Li^+ current is redirected to the Ag particle, leading to its lithiation and expansion. Previous studies have examined the evolution of Li–Ag alloying in the Ag/C buffer layer,[36,188] demonstrating that as the Li fraction increases (and volume expansion occurs), the Li plating potential decreases, reducing the driving force for Li deposition at the Ag particle.[187] This phenomenon supports the idea that when individual Li filaments encounter Ag particles, there is a local deceleration in growth due to alloying. This effect is sufficient to promote the activation of other Li filaments, which continue to grow until they, too, contact Ag particles.

The presence of Ag nanoparticles within the SE matrix alters the growth of Li filaments from a localized advancing tip (*Figure 4.6-b*) to a more homogeneously advancing front (*Figure 4.6-d*). This shift promotes the extrusion of Li–Ag within the porous network, facilitating the transport of Ag to the forefront of the infiltrating Li. This mechanism demonstrates how Ag nanoparticles redistribute Li current and homogenize Li deposition, effectively mitigating the growth of localized dendritic structures. Additionally, the agglomeration of Ag nanoparticles alongside the advancing Li dendrite front suggests that their presence promotes more uniform Li-filament growth, which helps explain the suppression of M_1. Furthermore, the interaction between the advancing Li dendrites and the uniformly distributed Ag nanoparticles leads to the delocalization of dendrite growth, slowing Li infiltration and reducing the risk of SE fracture at high current densities, thereby mitigating M_2.

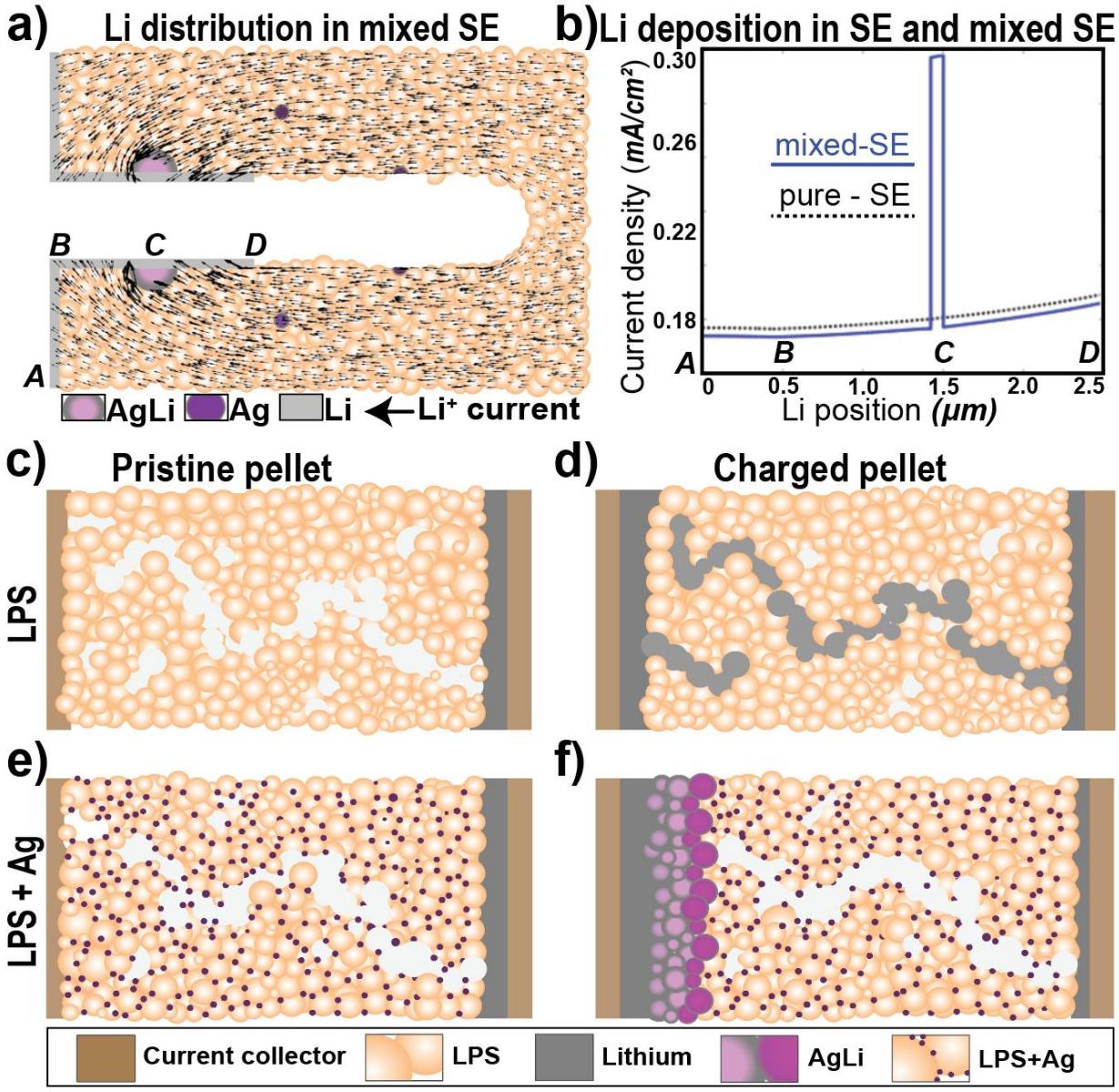

Figure 4. 6. Mechanistic comparative analysis of role of Ag nanoparticles in the solid electrolyte. 6a) Li distribution in mixed SE. 6b) Current density distribution in bare SE and mixed SE. 6c) Uncharged pristine pellet. 6d) Failure of charged pellet due to percolating pore networks. 6e) Uncharged pristine pellet with Ag particles dispersed in LPS. 6f) Survival of charged pellet due to Ag–Li interaction.

With these insights into how Ag nanoparticles influence Li dendrite growth and current distribution, it becomes clear that the same principles could have important applications in other areas of battery design, such as anode scaffolding. For instance, the application of Ag nanoparticles could be explored in anode scaffolding, a critical area where the reversibility of plated Li remains unresolved. Although anode scaffolds can maintain zero strain during Li plating, Li stripping is often limited by the interplay between diffusion and stripping kinetics, restricting current rates. Several scaffold designs have been proposed to address issues such as dendrite formation,

mechanical stability, electrical conductivity, and interfacial stability between the scaffold and SE; however, challenges with high-rate electrochemical cycling persist.[189,190]

In summary, this work offers compelling evidence that Ag nanoparticles are highly effective in suppressing Li-dendrite growth and stress-induced fracture in SEs. These findings not only provide a deeper understanding of the mechanisms at play but also open the door to new battery designs that could overcome longstanding challenges in high-energy-density batteries. Moving forward, optimization of the nanoparticle size, distribution, and concentration, alongside long-term cycling studies, will be critical to translating these results into commercially viable technologies.

4.6 Methods and supplementary results

Preparation of SUS | Li | SE/mSE | Li | SUS cells: Glassy LPS material was synthesized by ball milling 75% Li_2S (99.9% metal basis, Alfa Aesar) and 25% P_2S_5 (99.9% metal basis, Alfa Aesar) for 4 h. LPS was mixed with Ag (99.5% metal basis, Sigma Aldrich <100nm) nanoparticles using a vertical shaker for 10 min at 25 cycles per second. The cell was prepared in the following sequence. Lithium electrodes were first cut from Li-metal foils (99.9% metal basis, Alfa Aesar) and attached to the SE. The cells were then assembled using an in-house-designed cell-making toolkit (illustrated in *Figure SI-4.1*). A constant stack pressure of 5 MPa was applied to the cell to maintain the conformal Li–SE interfacial contact.

Electrochemical cycling and electrochemical impedance spectroscopy: Each cell was tested following two sequential stages: 1) Initial rest stage: the cells were rested for 12 h after assembly under the stack pressure. EIS measurement was conducted every 4 h to monitor the temporal evolution of both the bulk and interfacial resistances. 2) Electrochemical (EC) cycle stage. The charge, cycling, and EIS measurements were performed using a potentiostat (VMP-300, BioLogic). The EC and EIS measurements were conducted at room temperature in a temperature-controlled chamber to ensure a constant cycling temperature. The EC measurements were performed with an electrode diameter d=6.35 mm. The EIS measurements were conducted at a frequency ranging from 10^{-3} to 7×10^{6} Hz.

Focused ion beam and scanning electron microscopy/Energy-dispersive X-ray spectroscopy: FIB–SEM/EDS characterization was performed on a FEI Helios G4 dual-beam FIB system equipped with a Ga+ ion beam and a Scios 2 Dual Beam SEM/FIB equipped with a Ga+ ion beam. Pellets were cut in the normal direction using FIB and were characterized using SEM under a tilt angle of 52°. The samples were transferred from a glovebox to the FIB-SEM using the ZoNexus air-free transfer module for SEM/FIB.

3D reconstruction method: The charged cell was tilted to a 52° angle, positioning the polished cross-sectional surface perpendicular to the ion beam. Trenches were milled around the area of interest using the ion beam, exposing the cross-section to a top-mounted electron beam at the same 52° angle. A backscattered-electron image was then captured to provide 2D morphological information on the Ag front within the SE. Subsequently, thin slices of 20 nm were milled away

from the cross-section using the ion beam, and another backscattered-electron image was obtained. This process was repeated several hundred times, after which the image stack was aligned, cropped, and combined into a 2D image stack (*Figure 4.4-c*). For a more detailed view, a video of the 3D stack images of the FIB cross-section can be found in the SI attachment. The 2D image stack, along with the corresponding two-phase segmentation image where dendrites are represented in red and other structures in green, is presented in *Figure 4.4-c*. These classifiers were trained in the Trainable Weka Segmentation plug-in in the ImageJ software to complete the segmentation process for the entire 2D image stack. The 3D visualization and reconstruction of the segmentation was performed with the 3D slicer software.

Modeling of Li diffusion in SE, deposition in pores, and alloy with Ag particles: The transport of Li^+ in the SE can be described by the ohmic relations:

$$\nabla^2 \phi_{SE} = 0, \qquad \mathbf{i} = -\sigma_{Li^+} \nabla \phi_{SE} \tag{1}$$

The current density involved in the lithiation is controlled by the surface overpotential (η) through the commonly used Butler–Volmer equation incorporating the mechanical effect as derived by Ganser at al[171]:

$$i_{ct} = i_{exc} e^{\frac{(1-\alpha_a)\overline{V}_{Li}\Delta P_{Li}}{RT}} \left(e^{\frac{\alpha_a F}{RT}\eta} - e^{-\frac{\alpha_c F}{RT}\eta} \right) \tag{2}$$

$$i_{ct} = -i_n = -\mathbf{i} \cdot \mathbf{n}_{\mathrm{SE}} \tag{3}$$

Here, i_{ct} is the current density due to charge transfer across the interface, i_n is the local current density normal to the interface and i_{exc} is the reference exchange current density of the Li/Li^+ reaction. α_a and α_c are the anodic and cathodic charge-transfer coefficients for the reaction, respectively; η is the surface overpotential in the absence of mechanical effect: $\eta = \phi_{Anode} - V_0 - \frac{\overline{V}_{Li}\Delta P_{AgLi}}{F}$, where ϕ_{Anode} is the electrode potential, which equals zero for Li metal anode; however, in the situation when Ag particles are activated, this anode potential evolutes following the open circuit potential of Ag-Li alloy, as discussed in our earlier work[187] and replotted in the following. V_0 is the open circuit potential without compressive stress; $\overline{V}_{Li}\Delta P_{AgLi}$ is the mechanical energy induced by the local compressive stress.

An in-house-developed code based on the finite element method and the MOOSE framework[78] was implemented to numerically solve all the coupled electro-chemo-mechanical PDEs. The default values of the parameters (such as the electronic/ionic conductivities for Li^+ transport in the SE and electrons in the Li metal) used in this work were obtained from experimental measurements of LPS-type SE and are listed in the last column of Table 4.1.

Table 4. 1. Key parameters used in this work.

NAME	SYMBOL	UNIT	VALUE	REF
Exchange current density at electrode/SE interface	i_{exc}^{k}	mA/cm^2	1.3	[79]
Exchange current density at void/SE interface	i_{exc}^{V}	mA/cm^2	0.01	[80]
Ionic conductivity in the SE	σ_{M^+}	mS/cm	0.1	[81]

Experimental setup for electrochemistry: The cells are assembled in a small PEEK tube as shown in the *Figure SI-4.1*.The SE is first pressed in the small PEEK tube (depicted while) at 300MPa for the pore-percolating regime, and 1GPa for the non-percolating regime. Li metal is then attached to both sides of the SE, followed by SUS foils in the case of symmetric cells. In the case of half cells, one side of the pellet is not attached to Li and will only be in direct contact with SUS. Finally, in the case of symmetric cells where we use a Li3N and LiF buffer layer, The SE is first pressed at 100MPa, then the Li3N+LiF powder is added to both sides. The pellet is pressed to 300MPa followed by attaching Li and SUS on both sides of the pressed SE+BL.

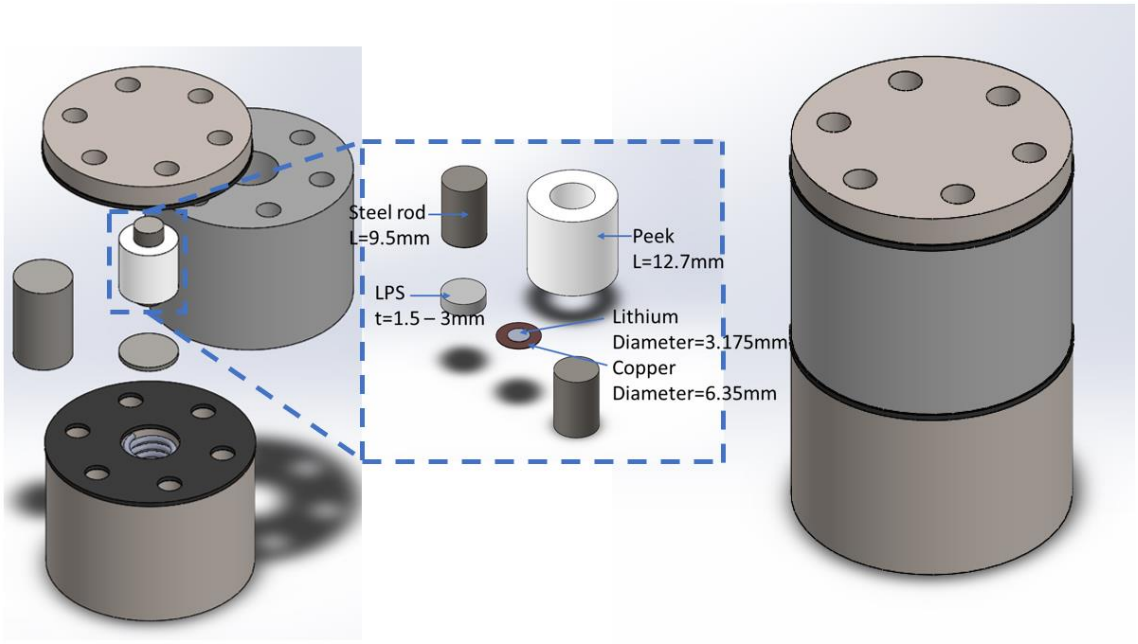

Figure SI-4. 1. The experimental setup for EC charging and cycling experiments.

Electrochemical exploration of different Ag contents: *Figure SI-4.2* showcases several symmetric cells that are charged at 0.2mA/cm^2 to either failure or Li source depletion. The cells are made by pressing the different SEs to 300MPa and attaching Li metal and SUS on both sides. The cell is then assembled in our EC experimental setup. This experiment highlights failure suppression with as little as 0.5%Ag.

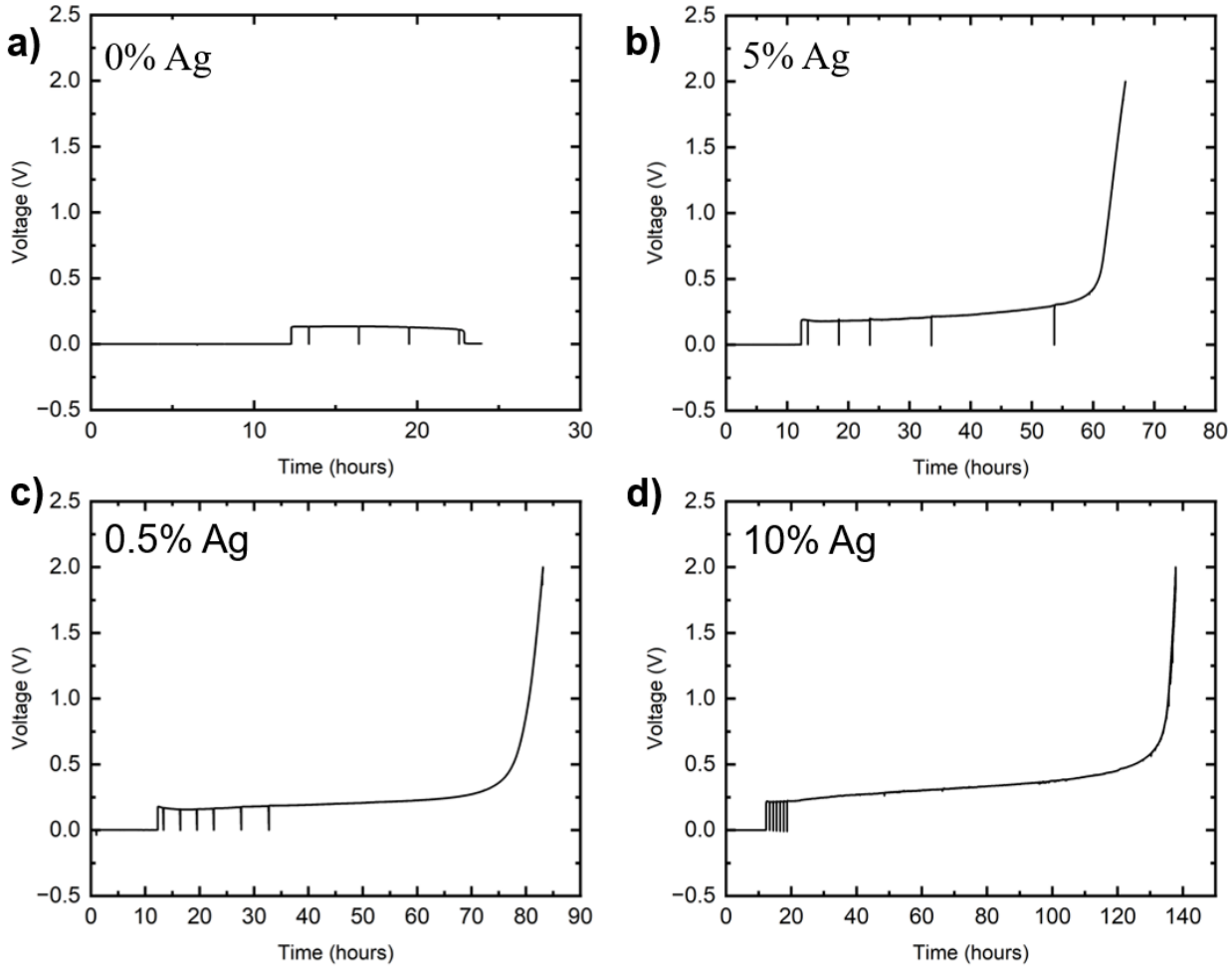

Figure SI-4. 2. EC charging at 0.2mA/cm^2 for different LPS-Ag contents.

State of charge measurement: Four half-cells were prepared with LPS-2%Ag as the solid electrolyte. The cells were charged under constant current density of 0.2mA/cm^2 at the same time and stopped at different states of charge, respectively 5hours, 10 hours, 20 hours and finally 40hours; as shown in *Figure SI-4.3*. The stopped cells were disassembled and sealed in epoxy for polishing.

The first 3 cells (5, 10, and 20 hours) were polished in a Top-down fashion by starting on the Li-plating side; shown in *Figure SI4.4*, *SI-4.5* and *SI-4.6*. Several optical images are taken to show the evolution of the cell macroscopic morphology as layers are polished away. The 40hours cell is used for cross-sectional imaging; optical microscopy is shown in *Figure SI-4.7*.

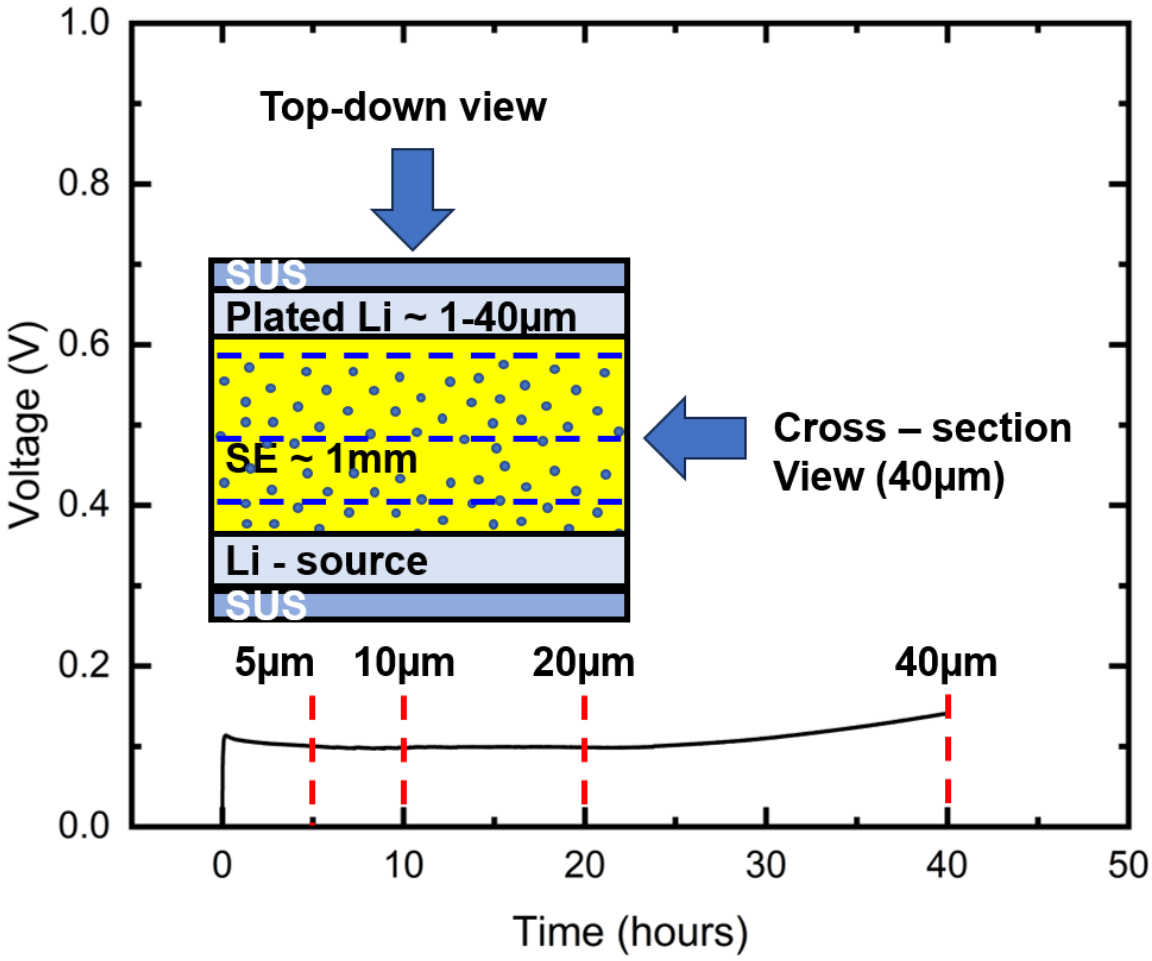

Figure SI-4. 3. The voltage profile of 4 different cells stopped at different states of charge.

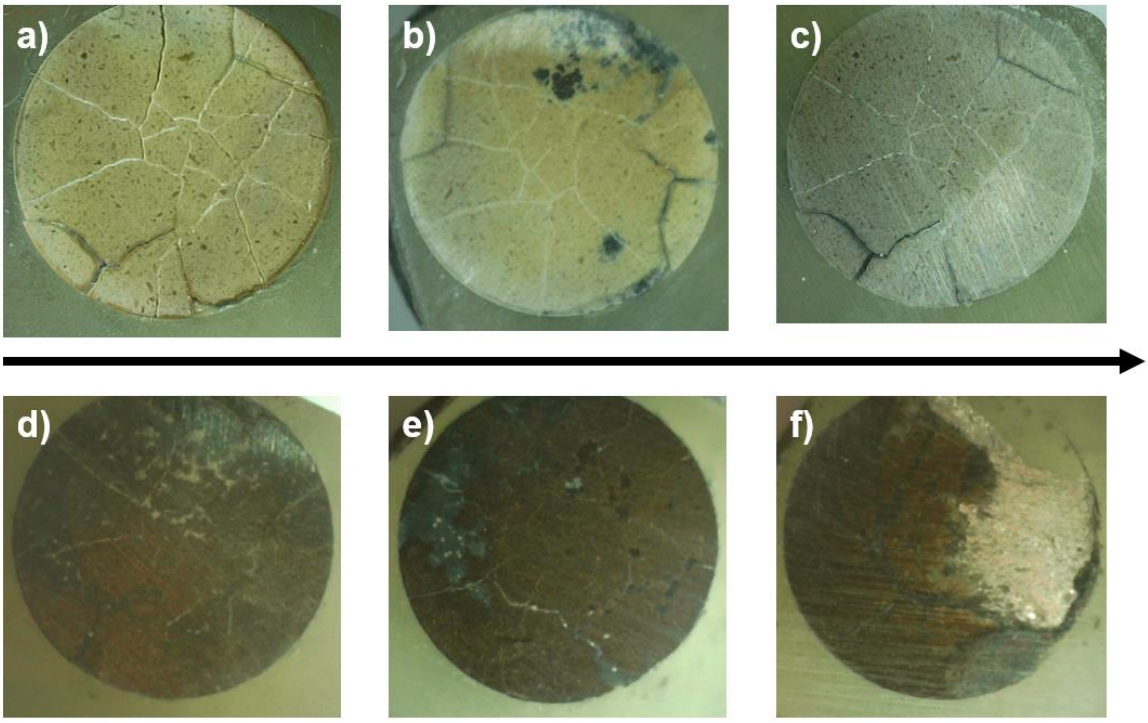

Figure SI-4. 4. Progressive OM images charged cell for 5 hours at different polishing steps.

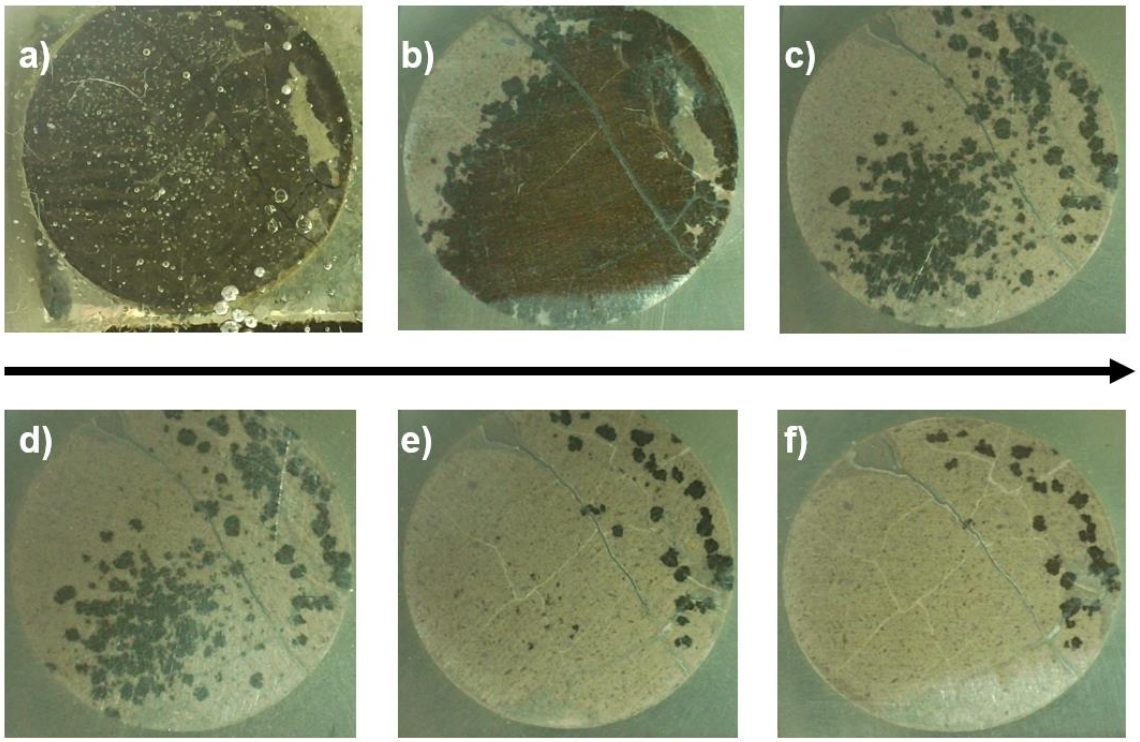

Figure SI-4. 5. Progressive OM images charged cell for 10 hours at different polishing steps.

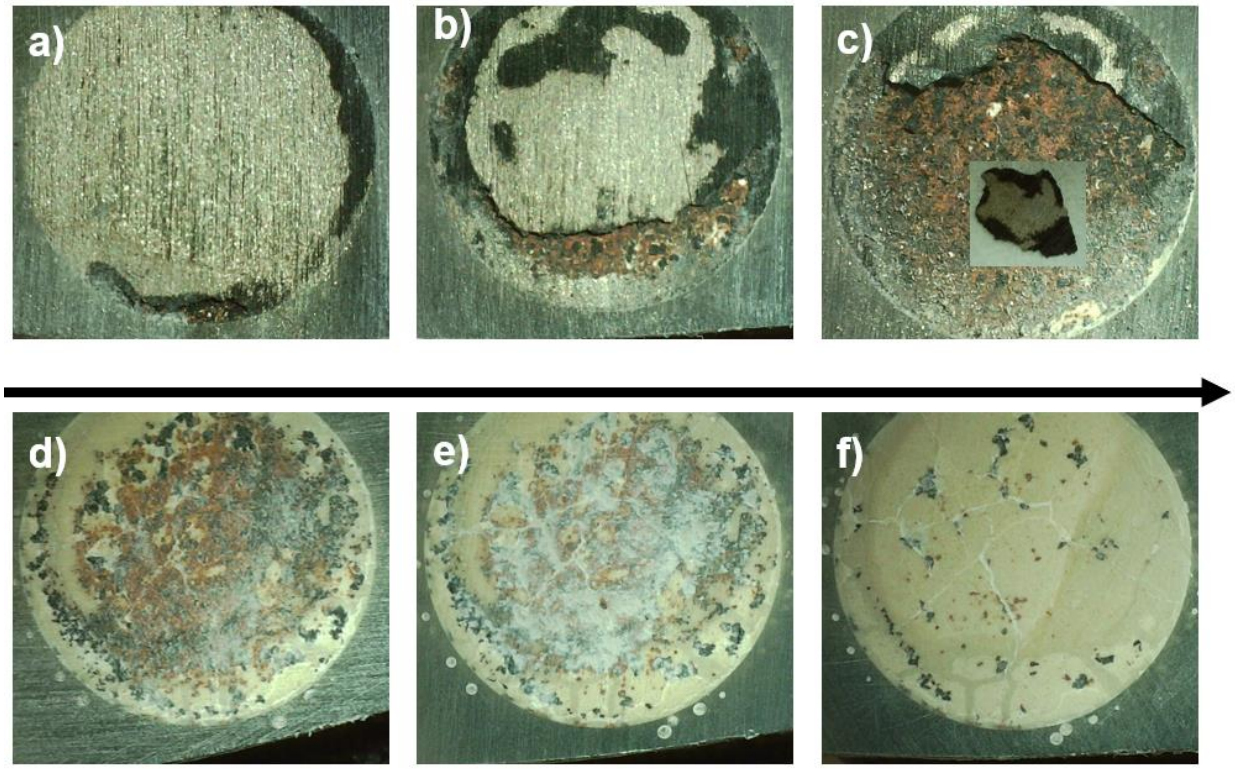

Figure SI-4. 6. Progressive OM images charged cell for 20 hours at different polishing steps.

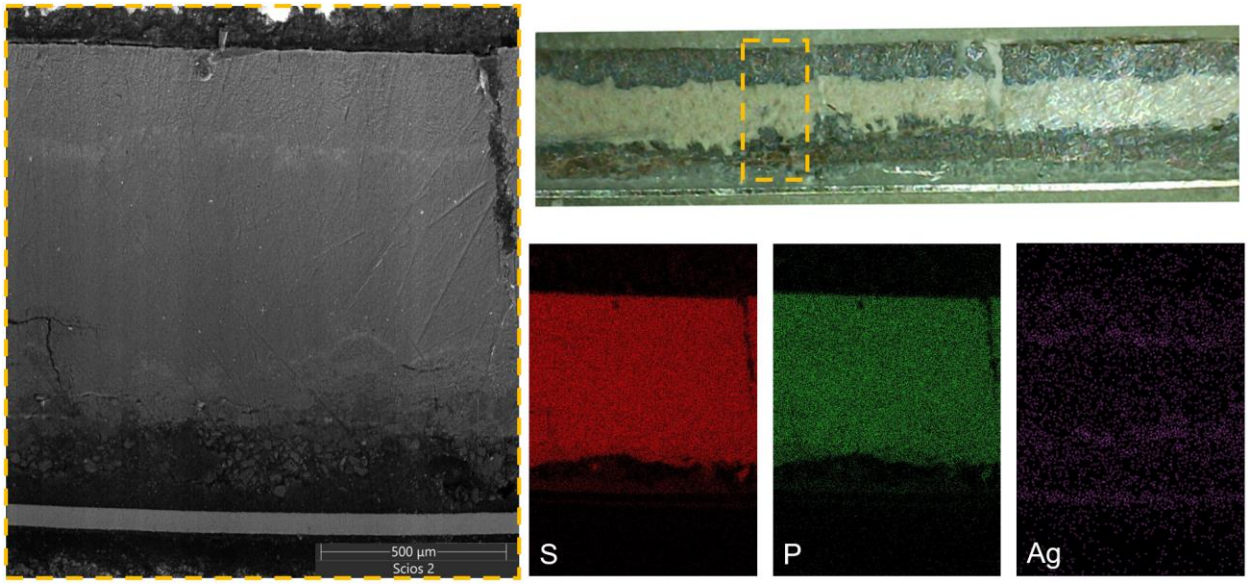

Figure SI-4. 7. Cross-section OM and SEM/EDS image of polished cell charged for 40hours.

Unidirectional constant current density 0.2mA/cm^2 on LPSCl and Ag mixed-LPSCl electrolyte: Half-cells with LPSCl and LPSCl-2%Ag were prepared and subjected to the unidirectional constant current density measurement. The Ag content tested was 2%. It is shown in *Figure SI-4.8* that all cells show similar behavior, both cells exhibited Li depletion behavior. That means that LPSCl displays non-percolating regime behavior. Li penetration does not occur on LPSCl pressed at 300MPa.

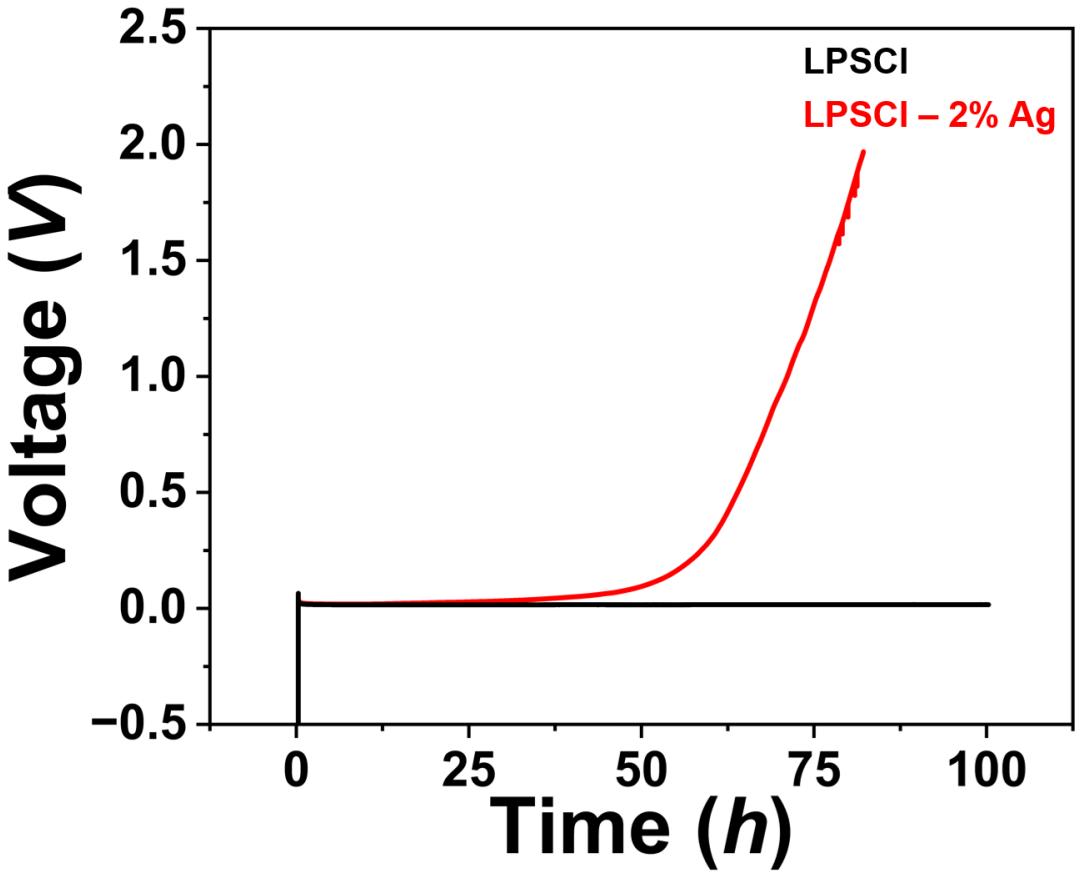

Figure SI-4. 8. Voltage profiles for LPSCl and LPSCl + 2% Ag Half-cell charged at 0.2 mA/cm^2.

Unidirectional increased current density stress test on LPSCl electrolyte: Symmetric cells with LPSCl and various Ag mixed LPSCl were prepared and subjected to the unidirectional increased current density measurement. The Ag content tested were 2%, 5%, and 10%. It is shown in *Figure SI-4.8* that all cells show similar behavior, they all short-circuit at 1.6mA/cm^2 except for the cell with LPSCl-5%Ag as the solid electrolyte which short-circuited at 0.8mA/cm^2.

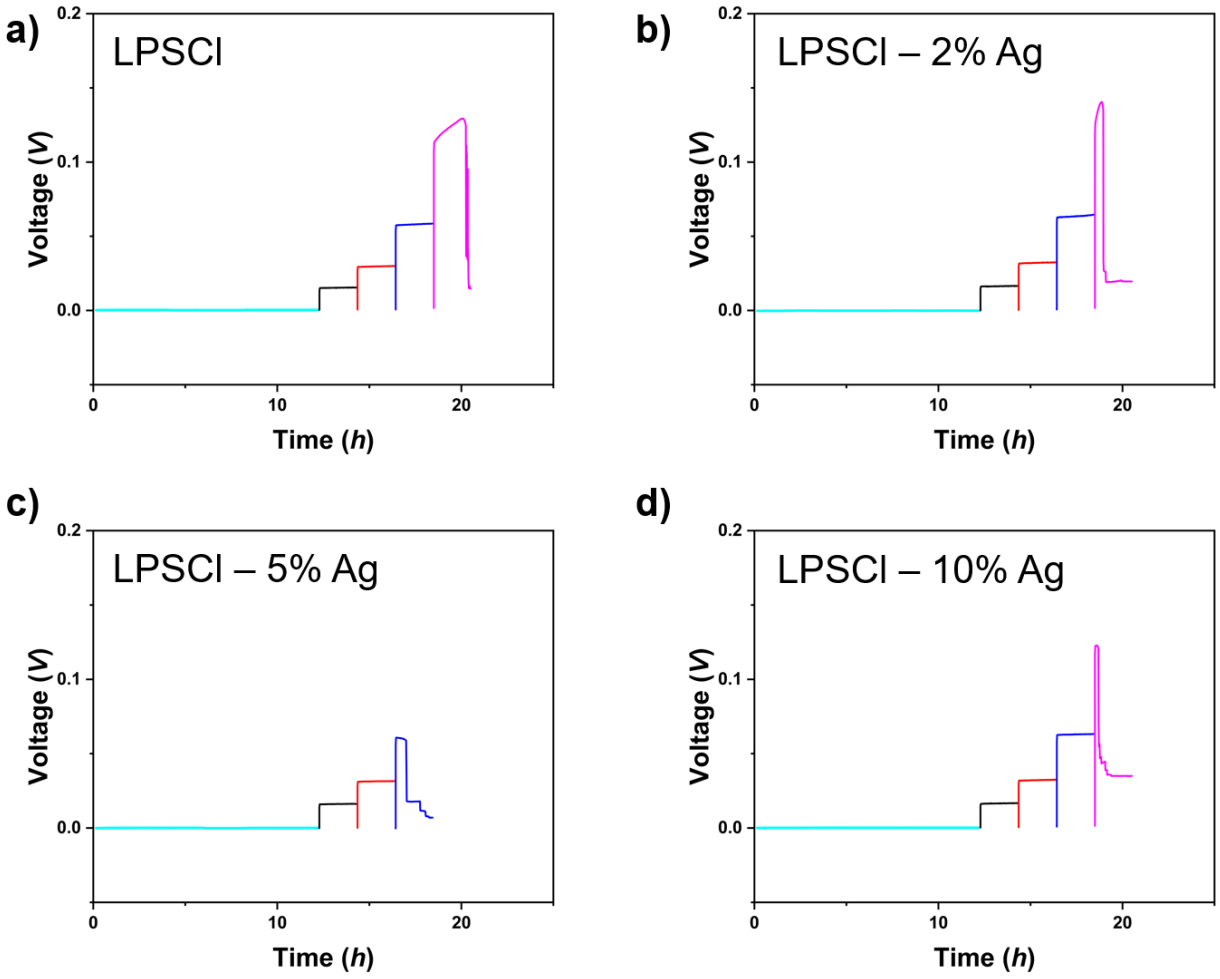

Figure SI-4. 9. Comparison of cells with different Ag contents in the SE at increasing current density.

4.7 Acknowledgements

This work was supported by the Samsung Advanced Institute of Technology and the Office of Energy Efficiency and Renewable Energy of the U.S. Department of Energy under Contract No. 1384-1778. The SEM analysis was performed at the Molecular Foundry, Lawrence Berkeley National Laboratory, supported by the Office of Science, Office of Basic Energy Sciences, of the U.S. Department of Energy under Contract No. DE-AC02-05CH11231. This research used 7 BM of the National Synchrotron Light Source II; a U.S. Department of Energy (DOE) Office of Science User Facility operated for the DOE Office of Science by Brookhaven National Laboratory under Contract No. DE-SC0012704. This research used the Lawrencium computational cluster resource provided by the IT Division at Lawrence Berkeley National Laboratory (supported by the Director, Office of Science, Office of Basic Energy Sciences, of the U.S. Department of Energy under Contract No. DE-AC02-05CH11231) and the Savio computational cluster resource provided by the Berkeley Research Computing program at the University of California, Berkeley (supported by the UC Berkeley Chancellor, Vice Chancellor for Research, and Chief Information Officer). The modeling work provided by QHT is supported by the US Army Research Office with award number W911NF2310302. S.T.O is supported by the Schmidt Science Fellows, in partnership with the Rhodes Trust. The authors also gratefully acknowledge BNC personnel starting with director Paul Lum, Dr. Naima Azgui and Andrew Gubser for the help provided in using SEM resources.

Chapter 5: Summary and outlook

This thesis has presented a detailed exploration of lithium dendrite suppression in solid-state batteries (SSBs) with lithium metal anodes, a critical challenge for next-generation energy storage systems. Through a combination of experimental studies and computational modeling, we have gained significant insights into the mechanisms of dendrite growth in solid electrolytes (SEs) and have proposed strategies to mitigate this issue, enhancing the performance, safety, and longevity of SSBs.

In **Chapter 2**, we examined the effect of solid-electrolyte pellet density on the performance and failure of solid-state batteries. Our findings revealed that when the SE reaches 99.5% density, a transition occurs in the pore microstructure from a percolating network to a non-percolating structure. This shift is critical as it directly influences the battery's behavior under applied current density. Below this density, batteries were prone to short-circuiting, while above this threshold, the cells exhibited significant improvements in cycling longevity. This work highlights the importance of optimizing solid-electrolyte density in order to prevent failure and ensure the reliable operation of SSBs under high current densities.

In **Chapter 3**, we focused on the role of Ag/C composite buffer layers (BLs) in anode-free lithium metal solid-state batteries (LMSSBs). Using first-principles atomistic and continuum modeling, we investigated how these buffer layers improve battery performance. Our study revealed that Ag maintains a homogeneous solid-solution structure during lithiation, even at high lithium concentrations, which contributes to uniform lithium deposition at the current collector (CC)/BL interface. We also identified several factors that promote Ag migration toward the CC and reduce interfacial resistance, enhancing cycling stability and mitigating dendrite formation. The insights gained from this work provide valuable guidelines for optimizing buffer layer design, particularly in anode-free architectures, to improve the performance of LMSSBs.

In **Chapter 4**, we explored the potential of silver (Ag) nanoparticles to suppress lithium dendrite growth within solid electrolytes. Our experiments demonstrated that Ag nanoparticles mitigate two key failure mechanisms: dendrite propagation at low current densities and stress-induced SE fractures at higher current densities. Ex-situ characterization, including FIB-SEM and EDS analysis, revealed that Ag nanoparticles migrate alongside advancing Li dendrites, promoting homogeneous growth and reducing localized stress concentrations. This migration results in a more uniform distribution of lithium, which could potentially enable higher charging rates in SSBs. These findings suggest that the incorporation of Ag nanoparticles is a promising approach to enhancing the performance and safety of solid-state batteries by addressing both dendrite growth and mechanical stability.

While this dissertation has made significant contributions to the understanding and mitigation of lithium dendrite formation in solid-state batteries, several areas remain open for further exploration. First, the optimization of solid-electrolyte density, as discussed in Chapter 2, presents

an important direction for future work. Achieving consistent and scalable production of high-density SEs will be critical for the commercialization of SSBs. Advances in manufacturing techniques, such as improved sintering processes or additive manufacturing, could help achieve the necessary density while maintaining the mechanical and electrochemical properties required for battery stability. As discussed in Chapter 3, mechanistic understanding of Ag/C buffer layer is crucial to enable anode-free architectures. However, further research is needed to explore the long-term cycling behavior of these layers, particularly under real-world conditions.

The work presented in Chapter 4 on the role of Ag nanoparticles in dendrite suppression opens up exciting possibilities for nanoparticle engineering in SSBs. Future studies should focus on the scalability of incorporating nanoparticles into solid electrolytes and explore how varying nanoparticle size, distribution, and material composition might further improve performance. Additionally, the interaction between nanoparticles and other materials in the battery, such as the cathode and SE, warrants further investigation to understand potential synergies or drawbacks.

In conclusion, this thesis has laid a strong foundation for the advancement of dendrite suppression strategies in solid-state batteries. While challenges remain, the findings presented here provide a roadmap for future research and development efforts aimed at commercializing safer, higher-performing solid-state energy storage systems. Continued exploration of material design, manufacturing processes, and interface engineering will be essential in realizing the full potential of SSBs and facilitating their adoption in electric vehicles, grid storage, and other applications critical to a sustainable energy future.

References

[1] P. D. United Nations, Department of Economic and Social Affairs, **2024**, 1.

[2] Internet Live Stats, *Real Time Statistics Project*, **2024**.

[3] British Petroleum, *Stat. Rev. World Energy* **2023**, 1.

[4] B.P., *BP Energy Outlook*, **2024**.

[5] Y. Tian, G. Zeng, A. Rutt, T. Shi, H. Kim, J. Wang, J. Koettgen, Y. Sun, B. Ouyang, T. Chen, Z. Lun, Z. Rong, K. Persson, G. Ceder, *Chem. Rev.* **2021**, *121*, 1623.

[6] Energy Agency International, IEA, **2024**, 1.

[7] M. J. Wang, E. Kazyak, N. P. Dasgupta, J. Sakamoto, *Joule* **2021**, *5*, 1371.

[8] USABC, *15*, 7.

[9] USABC, *United States Adv. Batter. Consort. LLC* **2016**.

[10] USABC, **2025**, 1.

[11] F. Fe, S. Strength, T. Stability, T. Strength, S. Temperature, H. V. Resistance, 1.

[12] USABC Goals for Advanced Batteries for 12V Start Stop Vehicle Applications, 360.

[13] USABC goals for advanced electrolytes, *Lithium-Ion Batter. Chem.* **2019**, 301.

[14] U. Goals, L. F. Advanced, E. Cy, **2023**, 2023.

[15] USABC, **2014**, 450.

[16] P. Targets, K. Parameters, P. Details, O. Environment, P. Temperature, C. Temperature, 1.

[17] J. Janek, W. G. Zeier, *Nat. Energy* **2016**, *1*, 1.

[18] J. B. Goodenough, K. S. Park, *J. Am. Chem. Soc.* **2013**, *135*, 1167.

[19] T. Famprikis, P. Canepa, J. A. Dawson, M. S. Islam, C. Masquelier, *Fundamentals of inorganic solid-state electrolytes for batteries*, Vol. 18, Nature Publishing Group, **2019**, pp. 1278–1291.

[20] M. Nagasaki, K. Nishikawa, K. Kanamura, *J. Electrochem. Soc.* **2019**, *166*, A2618.

[21] P. Albertus, S. Babinec, S. Litzelman, A. Newman, *Nat. Energy* **2018**, *3*, 16.

[22] W. Huang, P. Xu, X. Huang, C. Zhao, X. Bie, H. Zhang, A. Chen, E. Kuzmina, E. Karaseva, V. Kolosnitsyn, X. Zhai, T. Jiang, L. Fan, D. Wang, Q. Zhang, *MetalMat* **2023**.

[23] R. Garcia-Mendez, J. G. Smith, J. C. Neuefeind, D. J. Siegel, J. Sakamoto, *Adv. Energy Mater.* **2020**, *10*, 1.

[24] Y. Wang, H. Hao, K. G. Naik, B. S. Vishnugopi, C. D. Fincher, Q. Yan, V. Raj, H. Celio, G. Yang, H. Fang, Y. M. Chiang, F. A. Perras, P. Jena, J. Watt, P. P. Mukherjee, D.

Mitlin, *Adv. Energy Mater.* **2024**, *14*, 1.

[25] C. Yu, Y. Li, M. Willans, Y. Zhao, K. R. Adair, F. Zhao, W. Li, S. Deng, J. Liang, M. N. Banis, R. Li, H. Huang, L. Zhang, R. Yang, S. Lu, Y. Huang, X. Sun, *Nano Energy* **2020**, *69*, 104396.

[26] L. Zhou, A. Assoud, Q. Zhang, X. Wu, L. F. Nazar, *J. Am. Chem. Soc.* **2019**, *141*, 19002.

[27] Y. Wang, W. D. Richards, S. P. Ong, L. J. Miara, J. C. Kim, Y. Mo, G. Ceder, *Nat. Mater.* **2015**, *14*, 1026.

[28] Q. Tu, T. Shi, S. Chakravarthy, G. Ceder, *Matter* **2021**, *4*, 3248.

[29] C. Monroe, J. Newman, *J. Electrochem. Soc.* **2004**, *151*, A880.

[30] C. Monroe, J. Newman, *J. Electrochem. Soc.* **2005**, *152*, A396.

[31] L. Barroso-Luque, Q. Tu, G. Ceder, *J. Electrochem. Soc.* **2020**, *167*, 020534.

[32] X. Ji, S. Hou, P. Wang, X. He, N. Piao, J. Chen, X. Fan, C. Wang, *Adv. Mater.* **2020**, *32*, 1.

[33] Y. G. Lee, S. Fujiki, C. Jung, N. Suzuki, N. Yashiro, R. Omoda, D. S. Ko, T. Shiratsuchi, T. Sugimoto, S. Ryu, J. H. Ku, T. Watanabe, Y. Park, Y. Aihara, D. Im, I. T. Han, *Nat. Energy* **2020**, *5*, 299.

[34] N. Suzuki, N. Yashiro, S. Fujiki, R. Omoda, T. Shiratsuchi, T. Watanabe, Y. Aihara, *Adv. Energy Sustain. Res.* **2021**, *2*.

[35] J. S. Kim, G. Yoon, S. Kim, S. Sugata, N. Yashiro, S. Suzuki, M. J. Lee, R. Kim, M. Badding, Z. Song, J. M. Chang, D. Im, *Nat. Commun.* **2023**, *14*.

[36] D. Spencer-Jolly, V. Agarwal, C. Doerrer, B. Hu, S. Zhang, D. L. R. Melvin, H. Gao, X. Gao, P. Adamson, O. V. Magdysyuk, P. S. Grant, R. A. House, P. G. Bruce, *Joule* **2023**, *7*, 503.

[37] C. Haslam, J. Sakamoto, *J. Electrochem. Soc.* **2023**, *170*, 040524.

[38] A. Müller, L. Paravicini, J. Morzy, M. Krause, J. Casella, N. Osenciat, M. H. Futscher, Y. E. Romanyuk, *ACS Appl. Mater. Interfaces* **2024**, *16*, 695.

[39] C. Cui, H. Yang, C. Zeng, S. Gui, J. Liang, P. Xiao, S. Wang, G. Huang, M. Hu, T. Zhai, H. Li, *Sci. Adv.* **2022**, *8*, 1.

[40] S. E. Sandoval, J. A. Lewis, B. S. Vishnugopi, D. L. Nelson, M. M. Schneider, F. J. Q. Cortes, C. M. Matthews, J. Watt, M. Tian, P. Shevchenko, P. P. Mukherjee, M. T. McDowell, *Joule* **2023**, *7*, 2054.

[41] S. Risal, C. Wu, F. Wang, S. Risal, F. C. Robles Hernandez, W. Zhu, Y. Yao, Z. Fan, *Carbon N. Y.* **2023**, *213*, 118225.

[42] C. Wu, B. Emley, L. Zhao, Y. Liang, Q. Ai, Z. Chen, F. C. Robles Hernández, F. Wang, S. Risal, H. Guo, J. Lou, Y. Yao, Z. Fan, *Nano Lett.* **2023**, *23*, 4415.

[43] D. W. Liao, T. H. Cho, S. Sarna, M. K. Jangid, H. Kawakami, T. Kotaka, K. Aotani, N. P. Dasgupta, *J. Mater. Chem. A* **2024**, *12*, 5990.

[44] T. Famprikis, P. Canepa, J. A. Dawson, M. S. Islam, C. Masquelier, *Nat. Mater.* **2019**, 1.

[45] Y. Xiao, K. J. Jun, Y. Wang, L. J. Miara, Q. Tu, G. Ceder, *Adv. Energy Mater.* **2021**, *11*.

[46] N. J. Taylor, S. Stangeland-Molo, C. G. Haslam, A. Sharafi, T. Thompson, M. Wang, R. Garcia-Mendez, J. Sakamoto, *J. Power Sources* **2018**, *396*, 314.

[47] F. Han, J. Yue, X. Zhu, C. Wang, *Adv. Energy Mater.* **2018**, *8*, 1.

[48] J. Lee, T. Lee, K. Char, K. J. Kim, J. W. Choi, *Acc. Chem. Res.* **2021**, *54*, 3390.

[49] S. Randau, D. A. Weber, O. Kötz, R. Koerver, P. Braun, A. Weber, E. Ivers-Tiffée, T. Adermann, J. Kulisch, W. G. Zeier, F. H. Richter, J. Janek, *Nat. Energy* **2020**, *5*, 259.

[50] F. Shen, M. B. Dixit, X. Xiao, K. B. Hatzell, *ACS Energy Lett.* **2018**, *3*, 1056.

[51] R. Garcia-Mendez, F. Mizuno, R. Zhang, T. S. Arthur, J. Sakamoto, *Electrochim. Acta* **2017**, *237*, 144.

[52] M. Nagao, A. Hayashi, M. Tatsumisago, T. Kanetsuku, T. Tsuda, S. Kuwabata, *Phys. Chem. Chem. Phys.* **2013**, *15*, 18600.

[53] Y. Ren, Y. Shen, Y. Lin, C. W. Nan, *Electrochem. commun.* **2015**, *57*, 27.

[54] T. Swamy, R. Park, B. W. Sheldon, D. Rettenwander, L. Porz, S. Berendts, R. Uecker, W. C. Carter, Y.-M. Chiang, *J. Electrochem. Soc.* **2018**, *165*, A3648.

[55] L. C. Zhang, J. F. Yang, C. L. Li, Y. X. Gao, X. P. Wang, Q. F. Fang, *J. Power Sources* **2020**, *449*.

[56] R. Sudo, Y. Nakata, K. Ishiguro, M. Matsui, A. Hirano, Y. Takeda, O. Yamamoto, N. Imanishi, *Solid State Ionics* **2014**, *262*, 151.

[57] A. Sharafi, E. Kazyak, A. L. Davis, S. Yu, T. Thompson, D. J. Siegel, N. P. Dasgupta, J. Sakamoto, *Chem. Mater.* **2017**, *29*, 7961.

[58] L. C. De Jonghe, L. Feldman, A. Beuchele, *J. Mater. Sci.* **1981**, *16*, 780.

[59] C. L. Tsai, V. Roddatis, C. V. Chandran, Q. Ma, S. Uhlenbruck, M. Bram, P. Heitjans, O. Guillon, *ACS Appl. Mater. Interfaces* **2016**, *8*, 10617.

[60] L. Porz, T. Swamy, B. W. Sheldon, D. Rettenwander, T. Frömling, H. L. Thaman, S. Berendts, R. Uecker, W. C. Carter, Y.-M. Chiang, *Adv. Energy Mater.* **2017**, *7*, n/a.

[61] X. Ji, S. Hou, P. Wang, X. He, N. Piao, J. Chen, X. Fan, C. Wang, *Adv. Mater.* **2020**, *2002741*, 1.

[62] S. Wenzel, D. A. Weber, T. Leichtweiss, M. R. Busche, J. Sann, J. Janek, *Solid State Ionics* **2016**, *286*, 24.

[63] A. D. Shugard, D. B. Robinson, **2012**.

[64] Y.-S. Wu, K. Pruess, peter Persoff, *Transp. Porous Media* **1998**, *32*, 117.

[65] Q. Tu, L. Barroso-Luque, T. Shi, G. Ceder, *Cell Reports Phys. Sci.* **2020**, *1*, 100106.

[66] W. S. LePage, Y. Chen, E. Kazyak, K.-H. Chen, A. J. Sanchez, A. Poli, E. M. Arruda, M. D. Thouless, N. P. Dasgupta, *J. Electrochem. Soc.* **2019**, *166*, A89.

[67] Y. Chen, Z. Wang, X. Li, X. Yao, C. Wang, Y. Li, W. Xue, D. Yu, S. Y. Kim, F. Yang, A. Kushima, G. Zhang, H. Huang, N. Wu, Y. W. Mai, J. B. Goodenough, J. Li, *Nature* **2020**, *578*, 251.

[68] E. J. Cheng, A. Sharafi, J. Sakamoto, *Electrochim. Acta* **2017**, *223*, 85.

[69] F. Han, A. S. Westover, J. Yue, X. Fan, F. Wang, M. Chi, D. N. Leonard, N. J. Dudney, H. Wang, C. Wang, *Nat. Energy* **2019**, *4*, 187.

[70] Z. Ning, D. S. Jolly, G. Li, R. De Meyere, S. D. Pu, Y. Chen, J. Kasemchainan, J. Ihli, C. Gong, B. Liu, D. L. R. Melvin, A. Bonnin, O. Magdysyuk, P. Adamson, G. O. Hartley, C. W. Monroe, T. J. Marrow, P. G. Bruce, *Nat. Mater.* **2021**, *20*, 1121.

[71] C. Lee, S. Y. Han, J. A. Lewis, P. P. Shetty, D. Yeh, Y. Liu, E. Klein, H. W. Lee, M. T. McDowell, *ACS Energy Lett.* **2021**, *6*, 3261.

[72] C. J. Permann, D. R. Gaston, D. Andrš, R. W. Carlsen, F. Kong, A. D. Lindsay, J. M. Miller, J. W. Peterson, A. E. Slaughter, R. H. Stogner, R. C. Martineau, *SoftwareX* **2020**, *11*, 100430.

[73] M. Golozar, A. Paolella, H. Demers, S. Savoie, G. Girard, N. Delaporte, R. Gauvin, A. Guerfi, H. Lorrmann, K. Zaghib, *Sci. Rep.* **2020**, *10*, 1.

[74] J. M. Doux, Y. Yang, D. H. S. Tan, H. Nguyen, E. A. Wu, X. Wang, A. Banerjee, Y. S. Meng, *J. Mater. Chem. A* **2020**, *8*, 5049.

[75] J. M. Doux, H. Nguyen, D. H. S. Tan, A. Banerjee, X. Wang, E. A. Wu, C. Jo, H. Yang, Y. S. Meng, *Adv. Energy Mater.* **2020**, *10*, 1.

[76] C. Hänsel, D. Kundu, *Adv. Mater. Interfaces* **2021**, *8*, 1.

[77] T. Shi, Q. Tu, Y. Tian, Y. Xiao, L. J. Miara, O. Kononova, G. Ceder, *Adv. Energy Mater.* **2020**, *10*.

[78] M. CHIKU, W. TSUJIWAKI, E. HIGUCHI, H. INOUE, *Electrochemistry* **2012**, *80*, 740.

[79] H. K. Tian, Z. Liu, Y. Ji, L. Q. Chen, Y. Qi, *Chem. Mater.* **2019**, *31*, 7351.

[80] J. C. Bachman, S. Muy, A. Grimaud, H. H. Chang, N. Pour, S. F. Lux, O. Paschos, F. Maglia, S. Lupart, P. Lamp, L. Giordano, Y. Shao-Horn, *Chem. Rev.* **2015**, *116*, 140.

[81] J. C. Bachman, S. Muy, A. Grimaud, H. H. Chang, N. Pour, S. F. Lux, O. Paschos, F. Maglia, S. Lupart, P. Lamp, L. Giordano, Y. Shao-Horn, *Inorganic Solid-State Electrolytes for Lithium Batteries: Mechanisms and Properties Governing Ion Conduction*, Vol. 116, **2016**, pp. 140–162.

[82] A. Masias, N. Felten, R. Garcia-Mendez, J. Wolfenstine, J. Sakamoto, *J. Mater. Sci.* **2019**,

54, 2585.

[83] A. Masias, N. Felten, R. Garcia-Mendez, J. Wolfenstine, J. Sakamoto, *J. Mater. Sci.* **2019**, *54*, 2585.

[84] Q. Zhang, D. Cao, Y. Ma, A. Natan, P. Aurora, H. Zhu, *Sulfide-Based Solid-State Electrolytes: Synthesis, Stability, and Potential for All-Solid-State Batteries*, Vol. 31, **2019**, pp. 1–42.

[85] K. Yoon, S. Lee, K. Oh, K. Kang, *Challenges and Strategies towards Practically Feasible Solid-State Lithium Metal Batteries*, Vol. 34, **2022**, pp. 1–19.

[86] Y. Xiao, Y. Wang, S. H. Bo, J. C. Kim, L. J. Miara, G. Ceder, *Understanding interface stability in solid-state batteries*, Vol. 5, Springer US, **2020**, pp. 105–126.

[87] W. Luo, Y. Gong, Y. Zhu, Y. Li, Y. Yao, Y. Zhang, K. K. Fu, G. Pastel, C. F. Lin, Y. Mo, E. D. Wachsman, L. Hu, *Adv. Mater.* **2017**, *29*, 1.

[88] S. Kim, C. Jung, H. Kim, K. E. Thomas-Alyea, G. Yoon, B. Kim, M. E. Badding, Z. Song, J. M. Chang, J. Kim, D. Im, K. Kang, *Adv. Energy Mater.* **2020**, *10*, 1.

[89] Y. Lu, C. Z. Zhao, H. Yuan, X. B. Cheng, J. Q. Huang, Q. Zhang, *Critical Current Density in Solid-State Lithium Metal Batteries: Mechanism, Influences, and Strategies*, Vol. 31, **2021**, pp. 1–33.

[90] H. Wang, H. Gao, X. Chen, J. Zhu, W. Li, Z. Gong, Y. Li, M. S. Wang, Y. Yang, *Adv. Energy Mater.* **2021**, *11*, 1.

[91] P. Barai, A. T. Ngo, B. Narayanan, K. Higa, L. A. Curtiss, V. Srinivasan, *J. Electrochem. Soc.* **2020**, *167*, 100537.

[92] X. Liu, R. Garcia-Mendez, A. R. Lupini, Y. Cheng, Z. D. Hood, F. Han, A. Sharafi, J. C. Idrobo, N. J. Dudney, C. Wang, C. Ma, J. Sakamoto, M. Chi, *Nat. Mater.* **2021**, *20*, 1485.

[93] J. Lau, R. H. DeBlock, D. M. Butts, D. S. Ashby, C. S. Choi, B. S. Dunn, *Sulfide Solid Electrolytes for Lithium Battery Applications*, Vol. 8, **2018**, pp. 1–24.

[94] Y. W. Byeon, H. Kim, *Review on Interface and Interphase Issues in Sulfide Solid-State Electrolytes for All-Solid-State Li-Metal Batteries*, Vol. 2, **2021**, pp. 452–471.

[95] E. Kazyak, R. Garcia-Mendez, W. S. LePage, A. Sharafi, A. L. Davis, A. J. Sanchez, K. H. Chen, C. Haslam, J. Sakamoto, N. P. Dasgupta, *Matter* **2020**, *2*, 1025.

[96] M. Otoyama, M. Suyama, C. Hotehama, H. Kowada, Y. Takeda, K. Ito, A. Sakuda, M. Tatsumisago, A. Hayashi, **2021**.

[97] J. Kasemchainan, S. Zekoll, D. Spencer Jolly, Z. Ning, G. O. Hartley, J. Marrow, P. G. Bruce, *Nat. Mater.* **2019**, *18*, 1105.

[98] M. J. Wang, R. Choudhury, J. Sakamoto, *Joule* **2019**, *3*, 2165.

[99] M. Wang, J. B. Wolfenstine, J. Sakamoto, *Electrochim. Acta* **2019**, *296*, 842.

[100] S. H. Park, D. Jun, J. E. Jung, S. G. Lee, G. H. Lee, Y. J. Lee, *J. Mater. Chem. A* **2022**,

21995.

[101] S. Kim, G. Yoon, S. K. Jung, S. T. Park, J. S. Kim, K. Yoon, S. Lee, K. Kang, *ACS Energy Lett.* **2023**, *8*, 9.

[102] S. Pastorello, *Gazz. Chim. Ital.* **1930**, *60*, 493.

[103] S. Pastorello, *Gazz. chim. ital.* **1931**, *61*, 47.

[104] E. E. Hoffman, D. H. Jansen, *LITHIUM SYMPOSIUM--ANALYTICAL PROCEDURES AND HIGH-TEMPERATURE CORROSION. Reading List*, Oak Ridge National Lab.(ORNL), Oak Ridge, TN (United States), **1958**.

[105] V. H. Perlitz, D. Struktur, **1933**, 155.

[106] L. Arnberg, S. Westman, *Acta Chem. Scand.* **1972**, *26*, 513.

[107] T. Noritake, M. Aoki, S. ichi Towata, T. Takeuchi, U. Mizutani, *Acta Crystallogr. Sect. B Struct. Sci.* **2007**, *63*, 726.

[108] A. D. Pelton, *Bull. Alloy Phase Diagrams* **1986**, *7*, 223.

[109] M. H. Braga, A. Debski, S. Terlicka, W. Gqsior, A. Goral, **2020**, *817*.

[110] A. Zunger, S. Wei, L. G. Ferreira, J. E. Bernard, **1990**, *65*, 353.

[111] A. Seko, Y. Koyama, I. Tanaka, *Phys. Rev. B - Condens. Matter Mater. Phys.* **2009**, *80*, 1.

[112] A. J. Bradley, B. Thewlis, **1926**, *50*.

[113] U. Mizutani, R. Asahi, H. Sato, T. Noritake, T. Takeuchi, *J. Phys. Condens. Matter* **2008**, *20*.

[114] A. Jain, S. P. Ong, G. Hautier, W. Chen, W. D. Richards, S. Dacek, S. Cholia, D. Gunter, D. Skinner, G. Ceder, K. A. Persson, *Commentary: The materials project: A materials genome approach to accelerating materials innovation*, Vol. 1, **2013**.

[115] G. Bergerhoff, I. Brown, F. Allen, *Crystallographic databases. Int Union Crystallogr*, Chester, **1987**.

[116] A. J. Bradley, C. H. Gregory, *London, Edinburgh, Dublin Philos. Mag. J. Sci.* **1931**, *12*, 143.

[117] S. Westman, **1965**, *19*, 1411.

[118] P. Mario, A. Rollier, E. Arreghini, *Zeitschrift für Krist. - Cryst. Mater.* **1939**, *101*, 470.

[119] W. Obrowski, *Chang. to MTLLA* **1963**, *17*.

[120] A. Johansson, H. Ljung, S. Westman, T. Norin, *Acta Chem. Scand.* **1968**, *22*, 2743.

[121] L. D. Gulay, J. C. Schuster, *J. Alloys Compd.* **2003**, *360*, 137.

[122] J. M. Sanchez, F. Ducastelle, D. Gratias, *Phys. A Stat. Mech. its Appl.* **1984**, *128*, 334.

[123] G. Ceder, *Comput. Mater. Sci.* **1993**, *1*, 144.

[124] A. van de Walle, G. Ceder, *J. Phase Equilibria* **2002**, *23*, 348.

[125] Q. Tu, T. Shi, G. Ceder, In *Electrochemical Society Meeting Abstracts prime2020*, The Electrochemical Society, Inc., **2020**, p. 972.

[126] M. Ganser, F. E. Hildebrand, M. Klinsmann, M. Hanauer, M. Kamlah, R. M. McMeeking, *J. Electrochem. Soc.* **2019**, *166*, H167.

[127] B. Orvananos, H. Yu, A. Abdellahi, R. Malik, C. P. Grey, G. Ceder, K. Thornton, *J. Electrochem. Soc.* **2015**, *162*, A965.

[128] S. Narayan, L. Anand, *Extrem. Mech. Lett.* **2018**, *24*, 21.

[129] J. N. Reddy, *New York* **1993**, *27*, 14.

[130] R. Malik, F. Zhou, G. Ceder, *Nat. Mater.* **2011**, *10*, 587.

[131] D. Spencer-Jolly, V. Agarwal, C. Doerrer, B. Hu, S. Zhang, D. L. R. Melvin, H. Gao, X. Gao, P. Adamson, O. V Magdysyuk, P. S. Grant, R. A. House, P. G. Bruce, *Joule* **2023**, *7*, 503.

[132] K. Persson, V. A. Sethuraman, L. J. Hardwick, Y. Hinuma, Y. S. Meng, A. Van Der Ven, V. Srinivasan, R. Kostecki, G. Ceder, *J. Phys. Chem. Lett.* **2010**, *1*, 1176.

[133] H. Tachikawa, *J. Phys. Chem. C* **2007**, *111*, 13087.

[134] J. H. Park, H. Yoon, Y. Cho, C. Y. Yoo, *Materials (Basel).* **2021**, *14*.

[135] M. Morgan, *Thin Solid Films* **1971**, *7*, 313.

[136] M. Wang, J. Sakamoto, *J. Power Sources* **2018**, *377*, 7.

[137] K. Yan, Z. Lu, H. W. Lee, F. Xiong, P. C. Hsu, Y. Li, J. Zhao, S. Chu, Y. Cui, *Nat. Energy* **2016**, *1*.

[138] R. Akolkar, *J. Power Sources* **2013**, *232*, 23.

[139] A. D. Pelton, *J. Phase Equilibria* **1991**, *12*, 42.

[140] N. Saunders, A. P. Miodownik, *CALPHAD (calculation of phase diagrams): a comprehensive guide*, Elsevier, **1998**.

[141] Y. Liang, Z. Du, C. Guo, C. Li, *J. Alloys Compd.* **2008**, *455*, 236.

[142] J. Sangster, A. D. Pelton, *J. Phase Equilibria* **1991**, *12*, 447.

[143] A. D. Pelton, *Bull. Alloy Phase Diagrams* **1986**, *7*, 228.

[144] J. Sangster, A. D. Pelton, *J. Phase Equilibria* **1991**, *12*, 678.

[145] J. Sangster, A. D. Pelton, *J. Phase Equilibria* **1991**, *12*, 33.

[146] J. Sangster, C. W. Bale, *J. Phase Equilibria Diffus.* **1998**, *19*, 70.

[147] G. R. Goward, N. J. Taylor, D. C. S. Souza, L. F. Nazar, *J. Alloys Compd.* **2001**, *329*, 82.

[148] J. Sangster, A. D. Pelton, *J. Phase Equilibria* **1997**, *18*, 289.

[149] A. J. McAlister, *Bull. Alloy Phase Diagrams* **1982**, *3*, 177.

[150] H. Okamoto, *J. phase equilibria* **1993**, *14*, 770.

[151] A. D. Pelton, *Bull. Alloy Phase Diagrams* **1986**, *7*, 142.

[152] J. Sangster, *J. Phase Equilibria Diffus.* **2018**, *39*, 74.

[153] H. W. Leavenworth, R. E. Cleary, *The solubility of Ni, Cr, Fe, Ti and Mo in liquid lithium*, Vol. 9, **1961**, pp. 519–520.

[154] J. Sangster, A. D. Pelton, *J. Phase Equilibria* **1993**, *14*, 514.

[155] H. Okamoto, *Bull. Alloy Phase Diagrams* **1990**, *11*, 306.

[156] M. Zeilinger, D. Benson, U. Häussermann, T. F. Fässler, *Chem. Mater.* **2013**, *25*, 1960.

[157] J. Songster, A. D. Pelton, *J. Phase Equilibria* **1991**, *12*, 37.

[158] A. A. Nayeb-Hashemi, J. B. Clark, A. D. Pelton, *Bull. Alloy Phase Diagrams* **1984**, *5*, 365.

[159] M. H. Braga, L. F. Malheiros, M. Hämäläinen, *Thermochim. Acta* **2000**, *344*, 47.

[160] R. A. Vargas-Hernández, *Phys. Rev. B* **1996**, *54*, 11 169.

[161] D. Joubert, *Phys. Rev. B - Condens. Matter Mater. Phys.* **1999**, *59*, 1758.

[162] J. P. Perdew, K. Burke, *Phys. Rev. B - Condens. Matter Mater. Phys.* **1996**, *54*, 16533.

[163] K. Mathew, J. H. Montoya, A. Faghaninia, S. Dwarakanath, M. Aykol, H. Tang, I. heng Chu, T. Smidt, B. Bocklund, M. Horton, J. Dagdelen, B. Wood, Z. K. Liu, J. Neaton, S. P. Ong, K. Persson, A. Jain, *Comput. Mater. Sci.* **2017**, *139*, 140.

[164] A. Jain, S. P. Ong, W. Chen, B. Medasani, X. Qu, M. Kocher, M. Brafman, G. Petretto, G. Rignanese, G. Hautier, D. Gunter, K. A. Persson, *Concurr. Comput. Pract. Exp.* **2015**, *27*, 5037.

[165] L. Barroso-Luque, P. Zhong, J. H. Yang, F. Xie, T. Chen, B. Ouyang, G. Ceder, *Phys. Rev. B* **2022**, *106*.

[166] L. J. Nelson, G. L. W. Hart, F. Zhou, V. Ozoliņš, *Phys. Rev. B - Condens. Matter Mater. Phys.* **2013**, *87*, 1.

[167] L. Barroso-Luque, J. H. Yang, F. Xie, T. Chen, R. L. Kam, Z. Jadidi, P. Zhong, G. Ceder, *J. Open Source Softw.* **2022**, *7*, 4504.

[168] L. Barroso-Luque, F. Xie, *J. Open Source Softw.* **2023**, *8*, 5867.

[169] A. Togo, I. Tanaka, *Scr. Mater.* **2015**, *108*, 1.

[170] A. Togo, *First-principles Phonon Calculations with Phonopy and Phono3py*, Vol. 92, **2023**, pp. 1–21.

[171] M. Ganser, F. E. Hildebrand, M. Klinsmann, M. Hanauer, M. Kamlah, R. M. McMeeking, *J. Electrochem. Soc.* **2019**, *166*, H167.

[172] X. Zhang, W. Shyy, A. Marie Sastry, *J. Electrochem. Soc.* **2007**, *154*, A910.

[173] K. Kerman, A. Luntz, V. Viswanathan, Y.-M. Chiang, Z. Chen, *J. Electrochem. Soc.* **2017**, *164*, A1731.

[174] Z. Ning, G. Li, D. L. R. Melvin, Y. Chen, J. Bu, D. Spencer-Jolly, J. Liu, B. Hu, X. Gao, J. Perera, C. Gong, S. D. Pu, S. Zhang, B. Liu, G. O. Hartley, A. J. Bodey, R. I. Todd, P. S. Grant, D. E. J. Armstrong, T. J. Marrow, C. W. Monroe, P. G. Bruce, *Nature* **2023**, *618*, 287.

[175] G. McConohy, X. Xu, T. Cui, E. Barks, S. Wang, E. Kaeli, C. Melamed, X. W. Gu, W. C. Chueh, *Nat. Energy* **2023**, *8*, 241.

[176] L. Ye, X. Li, *Nature* **2021**, *593*, 218.

[177] B. Hu, S. Zhang, Z. Ning, D. Spencer-Jolly, D. L. R. Melvin, X. Gao, J. Perera, S. D. Pu, G. J. Rees, L. Wang, L. Yang, H. Gao, S. Marathe, G. Burca, T. J. Marrow, P. G. Bruce, *Joule* **2024**, 1.

[178] M. S. Diallo, T. Shi, Y. Zhang, X. Peng, I. Shozib, Y. Wang, L. J. Miara, M. C. Scott, Q. H. Tu, G. Ceder, *Nat. Commun.* **2024**, *15*.

[179] M. Sun, T. Liu, Y. Yuan, M. Ling, N. Xu, Y. Liu, L. Yan, H. Li, C. Liu, Y. Lu, Y. Shi, Y. He, Y. Guo, X. Tao, C. Liang, J. Lu, *ACS Energy Lett.* **2021**, *6*, 451.

[180] W. Zhai, B. Yuan, Y. Fan, Y. Zhang, X. Zhang, Y. Ma, W. Liu, Y. Yu, *J. Am. Chem. Soc.* **2022**, *144*, 4124.

[181] T. Shi, Y. Zhang, G. Ceder, **2020**, 17399.

[182] T. Tatsuma, M. Taguchi, N. Oyama, *Electrochim. Acta* **2001**, *46*, 1201.

[183] J. Song, K. Xu, N. Liu, D. Reed, X. Li, *Mater. Today* **2021**, *45*, 191.

[184] X. Xu, S. Wang, H. Wang, C. Hu, Y. Jin, J. Liu, H. Yan, *J. Energy Chem.* **2018**, *27*, 513.

[185] L. Ma, J. Cui, S. Yao, X. Liu, Y. Luo, X. Shen, J. K. Kim, *Energy Storage Mater.* **2020**, *27*, 522.

[186] C. Yu, F. Zhao, J. Luo, L. Zhang, X. Sun, *Nano Energy* **2021**, *83*, 105858.

[187] F. Xie, M. S. Diallo, H. Kim, Q. H. Tu, G. Ceder, *Adv. Energy Mater.* **2024**, *14*, 1.

[188] J. Thomas, S. S. Behara, A. Van der Ven, *Chem. Mater.* **2024**, *69*, 1869.

[189] R. Wang, Q. Dong, C. Wang, M. Hong, J. Gao, H. Xie, M. Guo, W. Ping, X. Wang, S. He, J. Luo, L. Hu, *Adv. Mater.* **2021**, *33*, 1.

[190] E. Yi, H. Shen, S. Heywood, J. Alvarado, D. Y. Parkinson, G. Chen, S. W. Sofie, M. M. Doeff, *ACS Appl. Energy Mater.* **2020**, *3*, 170.